MODERNIZING INFRASOUND SYSTEMS: CHARACTERIZATION AND ANALYTICS APPROACHES FOR NEXT-GENERATION SENSORS

A DISSERTATION SUBMITTED TO THE GRADUATE DIVISION OF THE UNIVERSITY OF HAWAI'I AT MĀNOA IN PARTIAL FULFILLMENT OF THE REQUIREMENTS FOR THE DEGREE OF

DOCTOR OF PHILOSOPHY

IN

GEOLOGY AND GEOPHYSICS

MAY, 2019

By

Karina A. Asmar Toro

Dissertation Committee:

Milton A. Garcés, Chairperson
Robert Wright
Robert Dunn
James Foster
John Learned

Keywords: infrasound, smartphone, *Redvox* app, sensors, responses, data science

ACKNOWLEDGEMENTS

I would like to thank my advisor, Milton Garces, for giving me the opportunity to work with his team and for always being available to provide me with great scientific advice and guidance. I am very grateful to committee members, Profs. Robert Dunn, James Foster, John Learned, and Rob Wright, for their incredible patience and for always being willing to provide me with excellent and constructive feedback. Many thanks to our collaborators at Idaho and Oak Ridge National Laboratories, all of whom were great friends and mentors: David Chichester, Scott Watson, Tommy Holschuh, Edna Cárdenas, Jared Johnson, Richard Hale, Riley Hunley, Mónica Maceira, and Russ Henderson. I am deeply grateful to my co-workers for their immense support, not only always willing to lend a hand in this research but for always being fun to work with: Brian, Anthony, Nicole, Julie, Kayleigh, Tyler, Van, and Andrew. Many thanks to Darren for his excellent consulting services and for teaching me so much about sensor calibrations. This process would not have been completed without the help of many staff members in HIGP and the Earth Sciences Department, all of whom were my lifeline with the university as a remote student: Lily, Susan, Vi, Rena, Karynne, Bill, Grace, and Kyle, among many others. I am very grateful to the funding agencies which supported this research, Department of Energy (DOE), National Nuclear Security Administration (NNSA), Consortium for Verification Technology (CVT), and Multi-Informatics for Nuclear Operations Scenarios (MINOS). And finally, to my friends, my family, and David, all of whom were here from beginning to end, who were my constant support, and whom I owe everything I have achieved to.

ABSTRACT

The next generation of acoustic sensors is emerging to supplement legacy sensors traditionally used in regional and global networks. The most notable features of these modern devices are their significant reduction in size, weight, power, and cost, as well as the integration of high-resolution analogue-to-digital converters to provide digital data. The integration of these digital sensing devices as supplements to networks that are currently in use for nuclear and geophysical hazard monitoring is highly dependent on the modernization of characterization and data analytics methods. This dissertation presents approaches and results for such purposes in hope to contribute to the modernization of conventional technologies.

The MB3 digital microbarometer and the iPrecisionMic smartphone microphone are first characterized and evaluated against analog legacy systems in non-isolated conditions. Parametric responses in the digital domain are developed for both sensors. By overlapping these responses, digital sensor performance across the infrasound range can be benchmarked. A method is then developed for the estimation of smartphone built-in microphone amplitude responses in non-isolated conditions with conventional consumer products. The *Redvox Infrasound* app for iOS and Android is used to measure acoustic pressure waves with the smartphone devices. The method is applied to the calibration of the Samsung Galaxy S8 smartphone Model SM-G950U1, and an amplitude response model is estimated for the built-in microphone of the device across 0.5 – 4000 Hz.

A data science approach for real-time sensor monitoring and acoustic analysis in multi-sensing mobile networks is presented. The ability to generate visual products (e.g., text, tables, graphs, images, maps) in real-time and through batch analysis is described, and the potential use of these products for acoustic feature extraction, signal detection, and data-driven decision making is discussed. The results of this dissertation research show experimental and computational capabilities that can contribute to the modernization of infrasound systems.

TABLE OF CONTENTS

Acknowledgements **2**
Abstract **3**
List of Tables **6**
List of Figures **7**
1 Introduction **9**
1.1 Infrasound background 9
1.2 Infrasound sensors 11
1.2.1 Description 11
1.2.2 Sensor responses 13
1.2.3 New generations of infrasound sensors 14
1.3 Digital signal processing 16
1.3.1 Sampling and quantization 16
1.3.2 Time-frequency analysis 17
1.3.3 Removing sensor responses from digital time series data 18
1.4 Data science approach in mobile global networks 19
1.5 Dissertation overview 21
2 Digital acoustic sensor performance across the infrasound range in non-isolated conditions **22**
2.1 Introduction 23
2.2 Methods 24
2.2.1 Digital sensitivity measurement test 25
2.2.2 Sensor frequency response test 26
2.2.3 Sensor self-noise test 27
2.3 Characterization of the MB3 digital microbarometer response across 0.01 – 4 Hz 27
2.3.1 Digital sensitivity measurement 27
2.3.2 Sensor frequency response 28
2.3.3 Sensor self-noise 32
2.4 Evaluation of the analog Brüel & Kjaer Microphone Type 4193 microphone response above 0.25 Hz 34
2.4.1 Digital sensitivity measurement 34
2.4.2 Sensor frequency response 35
2.5 Evaluation of the iPrecision smartphone microphone response across 1- 20 Hz 39
2.5.1 Digital sensitivity measurement 39
2.5.2 Sensor frequency response 40
2.6 Conclusions 43

3 A method for estimating the amplitude response of smartphone built-in microphone sensors below 4 kHz 45
3.1 Introduction 46
3.2 Methods 48
3.3 Amplitude response of the iPrecision smartphone microphone 49
3.4 Amplitude response of the Samsung Galaxy S8 smartphone built-in microphone 52
3.5 Self-noise measurements 57
3.6 Summary 58
4 Real-time monitoring and analytics in multi-sensing mobile sensor networks 60
4.1 Introduction 61
4.2 Real-time device monitoring 62
4.3 Real-time acoustic data analysis 63
4.3.1 Data cleaning, transformation, and processing 63
4.3.2 Time synchronization 63
4.3.3 Time-frequency analysis 65
4.3.4 Real-time visual products 66
4.3.5 Batch analysis and feature extraction 68
4.4 Acoustic tonal detection 70
4.4.1 Detection algorithm 70
4.4.2 Performance statistics of the algorithm with a controlled data set 72
4.4.3 Approach for real-time monitoring of industrial equipment 75
4.5 Summary and Future Work 77
5 Conclusions and Future Work 78
5.1 Summary 78
5.2 Future work and recommendations 78
5.3 Contributions and implications 79
Appendix A 80
References 81

LIST OF TABLES

Table 2.1. Sine fit results with RMS error for MB3d digital sensitivity measurements 28

Table 2.2. Pole-Zero response model for the MB3d sensor..... 28

Table 2.3. Sine fit results with RMS error for B&K digital sensitivity measurements 35

Table 2.4. B&K Pole-Zero response model 35

Table 2.5. Sine fit results with RMS error at 16 Hz for iMic digital sensitivity measurement 39

Table 2.6. iMic (SN CQ10003) pole-zero response model 40

Table 3.1 Sensor description 49

Table 3.2. Pole-zero model for iMic sensor 50

Table 3.3. Digital gain levels for Samsung Galaxy S8 smartphone microphone across 0.5 – 2000 Hz octave bands..... 55

Table 4.1. Tri-message parameters and cross-correlation results for time synchronization of nodes A, B, C, and D, with common reference node. 65

Table 4.2. Mean sound pressure levels and signal-to-noise ratios for diesel generator startup/shutdown..... 69

Table 4.3. Combinations of user-specified parameters used for testing signal detection algorithm. 74

Table 4.4. Sensitivity values not equal to 1 per combination of user-specified parameters 74

Table 4.5. Positive Predictive Values not equal to 1 per combination of user-specified parameters..... 75

Table 4.6. Mean sound pressure levels and signal-to-noise ratios for cooling tower shutdown 77

LIST OF FIGURES

Figure 1.1. Certified station locations of the IMS Infrasound Network as of November, 2017 10

Figure 1.2. Example of Linear Variable Differential Transformer (LVDT). 12

Figure 1.3. MB3d transducer and digitizing blocks 14

Figure 1.4 *Redvox* global device collection 16

Figure 1.5. *Redvox* data science life cycle 20

Figure 2.1. Frequency response of the MB3d sensor across 29

Figure 2.2. Noise power spectral density levels for MB3d and MB2000 across 0.01 – 4 Hz. 30

Figure 2.3. Noise coherence results for MB3d and MB2000 across 0.01 – 4 Hz. 30

Figure 2.4. Noise response results for MB3d relative to MB2000 within the 0.01 – 4 Hz. 31

Figure 2.5. Self-noise power spectral density levels across the 0.01 – 10 Hz pass band for the MB2000 and MB3d 32

Figure 2.6. Self-noise coherence results between the MB3d and MB2000 across the 0.01 – 10 Hz pass band 33

Figure 2.7. Frequency response of the B&K sensor 36

Figure 2.8. Noise power spectral density levels for B&K and MB3d across 0.18 – 7.1 Hz. 37

Figure 2.9. Noise coherence results for B&K and MB3d across 0.18 – 7.1 Hz 37

Figure 2.10. Noise response results for B&K relative to MB3d across 0.18 – 7.1 Hz 38

Figure 2.11. Frequency response of the iMic sensor across 1 – 20 Hz 40

Figure 2.12. Noise power spectral density levels for iMic and B&K across 0.97 – 22.4 Hz. 41

Figure 2.13. Noise coherence results for iMic and B&K across 0.97 – 22.4 Hz 42

Figure 2.14. Noise response results for iMic relative to B&K across 0.97 – 22.4 Hz. 42

Figure 3.1. Measured amplitude response for the iMic sensor across 1 – 2000 Hz 51

Figure 3.2. Uncertainty of measured digital gain levels for iMic sensor 51

Figure 3.3 Sensor configuration (iMic, MB3d and S8) 53

Figure 3.4. Amplitude response for Samsung Galaxy S8 smartphone microphone 54

Figure 3.5. Uncertainty levels of Samsung Galaxy S8 smartphone digital sensitivities 56

Figure 3.6. Amplitude response averaged at 1/3-octave bands for Samsung Galaxy S8 smartphone microphone 55

Figure 3.7. Self-noise sound pressure levels (SPL) for iMic and Samsung Galaxy S8 smartphone microphone 57

Figure 3.8. Self-noise power spectral density (PSD) levels for iMic and Samsung Galaxy S8 smartphone microphone sensors averaged over 1/3-octave bands and compared to Infrasound Station Noise Models 58

Figure 4.1. Visual products for real-time monitoring of smartphone devices deployed on the Big Island of Hawaii. 62

Figure 4.2. Waveforms for four co-located synchronizing nodes A, B, C, and D, before and after time synchronization. 64

Figure 4.3. Real-time visual product for acoustic data from a Samsung Galaxy S8 using multiresolution analysis 67

Figure 4.4. Real-time visual product for acoustic data from a Samsung Galaxy S8 using Fourier analysis 68

Figure 4.5. Sound pressure level (SPL) increase at frequencies of interest during diesel generator startup 69

Figure 4.6. Convolution function related to the mean-subtracted spectral power function at 90 Hz of diesel generator startup/shutdown 71

Figure 4.7. Map visualization of distributed smartphone sensors and controllable sound source 72

Figure 4.8. Sound pressure levels (SPL) in decibels at 125 Hz for one device from each group of distributed smartphone sensors 73

Figure 4.9. Spectral analysis results for an acoustic record corresponding to a cooling tower shutdown measured with a Samsung Galaxy S8 76

CHAPTER 1. INTRODUCTION

1.1 Infrasound Background

Infrasound refers to atmospheric sound waves propagating with frequencies lower than 20 Hz. A wave is characterized as an oscillatory disturbance in a compressible medium that propagates away from a source without transporting mass (Pierce, 1981). In the case of sound waves, the disturbance corresponds to a pressure fluctuation. These types of waves propagate in the same direction as the particle motion (i.e., they are *longitudinal*) and are subject to the effects of a restoring force proportional to the displacement (i.e., they are *elastic*). Near the lower threshold of infrasound, the wavelengths become too long and gravity starts acting as the restoring force; once this happens, sound waves are referred to as *acoustic-gravity waves* (Evers and Haak, 2010). Sound waves disturb the medium in which they travel (i.e., the atmosphere) through compressions and rarefactions; these disturbances can be measured with microbarometers and microphones.

The classical absorption of sound in the atmosphere is caused by three different mechanisms: 1) viscous losses, which refer to frictional loss due to the compressions and expansions ensuing the sound wave propagation; 2) heat conduction losses resultant from heat transfer between higher temperature condensations and lower temperature rarefactions; and 3) molecular exchanges, which result when the kinetic energy of the propagating particles is converted to a different type of energy, such as internal rotational or vibrational energy (Kinsler et. al., 1982; Evers and Haak, 2010). Each of these processes is characterized by its relaxation time, which refers to the time it takes for the system to return to its original state. In general, the amplitude of the sound wave decreases exponentially upon propagation with absorption coefficient α. The low frequency approximation of α is proportional to the frequency squared, and is useful for all except extremely high ultrasonic frequencies or exceptionally viscous fluids (Kinsler et. al., 1982). Due to the low frequencies that characterize the infrasound range, attenuation of these waves in the atmosphere is minimal. Thus, infrasound can travel over vast distances without losing significant amounts of its original energy. Due to low attenuation over long distances and relatively fast propagation, infrasound is of particular interest for remote sensing purposes (Garces and Le Pichon, 2009).

Infrasound sources are prevalent in nature and man-made systems. Examples of natural events that are known to produce infrasound include: aurora (Wilson, 1967), lightning (Assink *et. al.*, 2008), surf (Garcés *et. al.*, 2006), microbaroms (Waxler and Gilbert, 2006), meteors (ReVelle, 1975), earthquakes (Mikumo, 1968), avalanches (Scott *et. al.*, 2007), and volcanoes (Fee *et. al.*, 2010). Anthropogenic events that have been characterized through their infrasonic emissions include: high-speed aircraft (Liszka and Waldemark, 1995), rockets (Balachandran and Donn, 1971), and man-made explosions (Ceranna *et. al.*, 2009). In recent years, acoustic signatures originating from operations inside nuclear facilities have also been reported (Watson *et al.*, 2018; Asmar *et al.,* 2018a), and further examples are presented in Chapter 4 of this dissertation.

Since its discovery in 1883, from the Krakatoa volcanic eruption, infrasound has evolved into a significant remote sensing and nuclear monitoring tool. Following an intermission during the late 20th century, the infrasound field experienced a renaissance with the negotiation of the Comprehensive Nuclear-Test-Ban Treaty (CTBT) from 1994 to 1996. Alongside seismic, hydroacoustic, and radionuclide detection, infrasound is one of the four monitoring technologies for nuclear nonproliferation. The International Monitoring System (IMS), which is the verification system of the CTBT, currently consists of 337 monitoring facilities encompassing these four verification technologies to monitor the planet for signs of nuclear explosions in the atmosphere, ground, and oceans. As of June 2017, the IMS Infrasound network consists of 49 certified stations. When fully operational, the IMS infrasound network will consist of 60 array stations deployed strategically across 35 countries (global station distribution is shown in Figure 1.1), ensuring reliable detection of a 1 kiloton atmospheric nuclear explosion anywhere in the globe by at least two stations (Marty, 2019; Hupe *et al.*, 2018). The signing of the CTBT has fueled the advance of infrasound monitoring technology during the last two decades (Christie and Campus, 2010) for nuclear nonproliferation purposes. This dissertation research explores the new generations of infrasound sensors, proposes novel methods for their characterizations, and presents a data science approach for real-time sensor monitoring and analysis in multi-sensing mobile sensor networks.

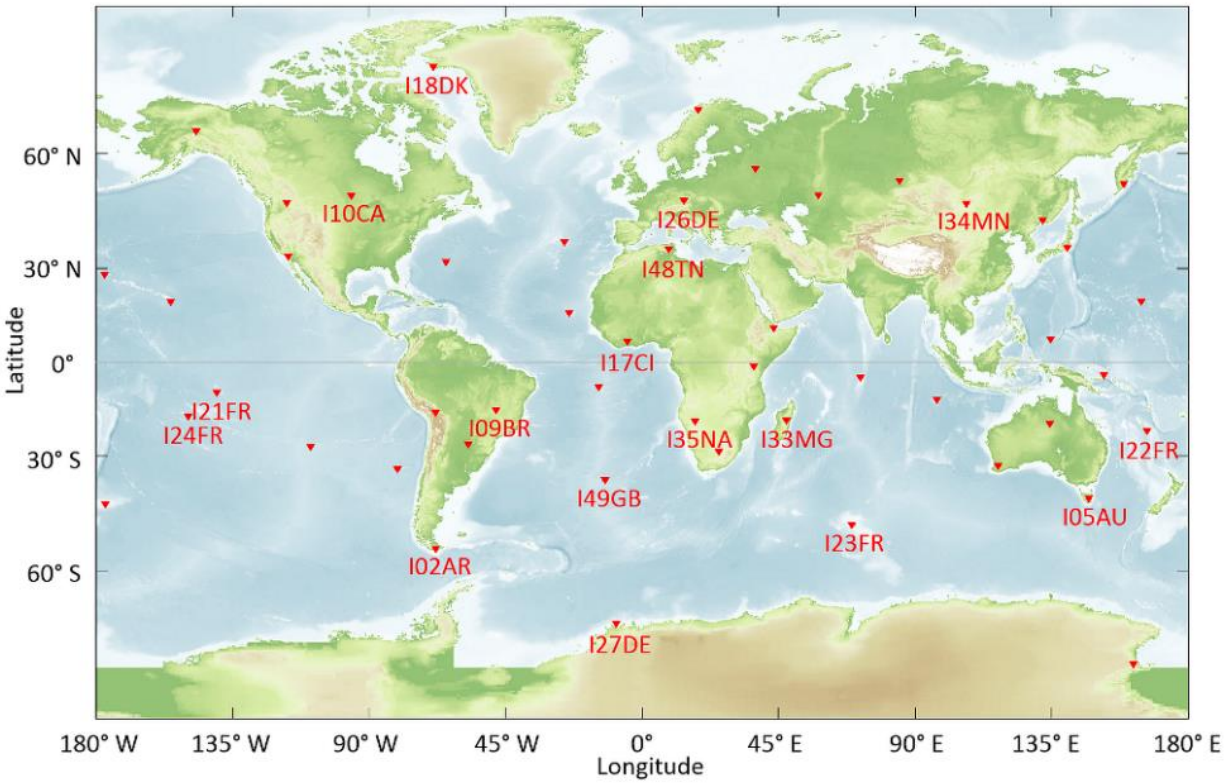

Figure 1.1. Certified station locations of the IMS Infrasound Network in compliance with the CTBT as of November, 2017 (Hupe *et al.,* 2018). Each red triangle represents a certified station array with the naming convention of the CTBT.

1.2 Infrasound Sensors

1.2.1 Description

Infrasound and acoustic sensors measure perturbations in the background atmospheric pressure and convert them to an electrical signal. The main components of such devices are the mechanical assembly sensitive to pressure and the associated *transducer*; the latter converts input pressure variations into an output electrical signal (Ponceau and Bosca, 2010). The *sensitivity* of the transducer determines the proportionality of the electrical output to the physical input, and is usually measured in V/Pa. Infrasound sensors (also called “microbarometers”) are designed with an enhanced response across the infrasound range, while acoustic sensors (also called “microphones”) optimize responses across the audio range. Absolute pressure sensors traditionally consist of a motion or stress transducer, which measures the deflection of an aneroid capsule impacted by atmospheric changes, and converts this displacement or stress into a dynamic electrical signal. These sensors, while practical for direct pressure measurements, are limited in dynamic range and subject to seismic sensitivity. Differential pressure sensors measure the pressure difference between the inside and outside of a closed cavity with a small leak. This small leak allows for measurements of short period pressure changes, while long period changes allow for the equalization of the inside and outside of the cavity through the flow in the leak (Ponceau and Bosca, 2010). The signal produced is proportional to the pressure difference between the measurement cavity and the reference (or backing) cavity. These sensors are sensitive to temperature differences between both cavities, and thermal insulation is usually recommended.

Absolute pressure sensors used by the IMS typically use a Linear Variable Differential Transformer (LVDT) or Magnet and Coil Velocity Transducer as the conversion mechanism. LVDT displacement transducers operate with three solenoid coils placed around a tube. An alternative current is driven through the primary coil, causing a voltage to be induced in the two secondary coils. These secondary coils are wired in reverse so that the output voltage is the difference between the two. A ferrite core is attached to an object that moves with incoming pressure disturbances, and slides along the axis of the tube, changing mutual inductances between the coils and causing changes in voltages. An example of an LVDT transducer is shown in Figure 1.2. The magnitude of the output voltage is proportional to the displacement of the object attached to the core and its phase indicates the direction of displacement (Ponceau and Bosca, 2010). The MB2000 and MB20005 (CEA/DAM, 2009) microbarometers, developed by the Commissariat à L’Énergie Atomique (CEA), are examples of absolute pressure sensors with LVDT transducers. A Magnet and Coil Velocity Transducer operates by generating an electromotive force (i.e., emf) voltage produced when a magnet moves proportionally to incoming pressure disturbances inside a

coil. This transducer is robust and has very low self-noise. The CEA developed MB3 (Seismowave, 2015) microbarometer is an example of an absolute pressure sensor with magnet-and-coil velocity transducer.

The most common differential pressure sensors used by IMS and acoustic manufacturers consist of a metal housing inside which resides a capacitor; this capacitor is formed by a fixed back plate and a diaphragm (i.e. the front plate). A constant electrical charge is supplied to the capacitor for polarization of the inner electric field. When the diaphragm is displaced by incoming pressure fluctuations, the difference in distance between both capacitor plates generates a change in capacitance which produces an output analog voltage, proportional to the distance differential. The constant electrical charge for the polarization of the electrical field between the capacitor plates may be applied from external voltage (i.e., a preamplifier or battery) or from a permanently charged polymer (i.e., an electret). Such sensors are named externally polarized and prepolarized condenser microphones/microbarometers, respectively (Brüel and Kjaer, 1996). The Chaparral 50A infrasound sensor developed by the Geophysical Institute of the University of Alaska (Chaparral Physics, 2011) is an example of a capacitor transducer used for IMS purposes.

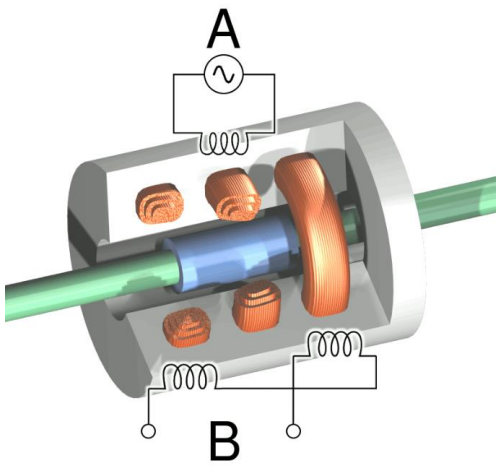

Figure 1.2. Example of Linear Variable Differential Transformer (LVDT). The ferritic core is represented in blue and the mobile element in green. The excitation voltage for the primary coil is shown in *A* and the output of the secondary coils is shown in *B* (Ponceau and Bosca, 2010).

Sensors based on microelectromechanical systems (MEMS) technology are also examples of differential acoustic sensors, and are extensively used in in industrial, military, scientific, and medical applications for acoustic measurements (Marcillo *et al.*, 2012; Ko, 2007). The Chaparral M60 infrasound sensor is an example of a high performance, miniaturized sensor designed for IMS specifications based on MEMS technology (Nief *et al.*, 2019). Sensors based on this technology enable mobile infrasound measurements and normally impractical deployments. At lower cost and high performance, they facilitate mass production and are commonly used in mobile consumer devices such as laptops and smartphones.

1.2.2 Sensor Responses

An acoustic sensor's response characterizes how the linear system (i.e. the sensor mechanisms) transforms an input pressure fluctuation into an output analog electrical signal (Merchant and Hart, 2011). The output of the linear system in the time domain is determined by the convolution of the input signal with the system's *impulse response*

$$y(t) = h(t) * x(t), \tag{1.1}$$

where $y(t)$ is the output signal, $x(t)$ is the input signal, and $h(t)$ is the system's impulse response. The Fourier Transform of the impulse response, referred to as the *frequency response*, determines the system's behavior in the frequency domain. A linear system's response to sinusoidal inputs is a sinusoidal output with the same input frequency, with amplitude and phase determined by the frequency response (Oppenheim and Schafer, 1989). The Fourier representation of Eq. (1.1) is given by

$$Y(e^{j\omega}) = H(e^{j\omega})X(e^{j\omega}), \tag{1.2}$$

where $Y(e^{j\omega})$ is the Fourier Transform of the output signal $y(t)$, $X(e^{j\omega})$ is the Fourier Transform of the input signal $x(t)$, and $H(e^{j\omega})$ the system's frequency response. The complex frequency response of the system can be represented in terms of magnitude and phase as

$$H(e^{j\omega}) = \left|H(e^{j\omega})\right| e^{j\measuredangle H(e^{j\omega})}. \tag{1.3}$$

$\left|H(e^{j\omega})\right|$ is referred to as the *magnitude response* or *gain* of the system, and $\measuredangle H(e^{j\omega})$ is referred to as the *phase response* or *phase shift* of the system. The magnitude and phase of the input and output of the system are related by

$$\left|Y(e^{j\omega})\right| = \left|H(e^{j\omega}\right| \cdot \left|X(e^{j\omega})\right| \tag{1.4a}$$

$$\measuredangle Y(e^{j\omega}) = \measuredangle H(e^{j\omega}) + \measuredangle X(e^{j\omega}), \tag{1.4b}$$

respectively (Oppenheim and Schafer, 1989). A linear system's frequency response can also be defined parametrically in terms of gain k, poles p_i and zeros z_i (Merchant and Hart, 2011) as

$$H(e^{j\omega}) = k\frac{\prod_{i=1}^{i=N_{zeros}}(j\omega - z_i)}{\prod_{i=1}^{i=N_{poles}}(j\omega - p_i)}. \tag{1.5}$$

The resulting value from evaluating Eq. (1.5) at a defined discrete radian frequency ω is a complex value of the form $a + jb$, with magnitude and phase

$$\left|H(e^{j\omega})\right| = \sqrt{a^2 + b^2} \quad \text{(1.6a)}$$

$$\measuredangle H(e^{j\omega}) = arctan\left(\frac{b}{a}\right), \quad \text{1.6b)}$$

respectively. The system's *transfer function* $H(s)$ can be obtained by setting $j\omega = s$ in Eq. (1.5). The frequency response corresponds to the transfer function evaluated on the imaginary axis of the s-domain; namely, the transfer function is the Laplace Transform of the system's impulse response (Smith, 1999).

1.2.3 New generations of infrasound sensors

In recent years, improvements upon legacy infrasound sensors have resulted in digital versions. These newer generations perform analog-to-digital conversion of the transducer electrical output inside the sensor itself, meaning the digitizer (acquisition unit) is embedded and not externally connected to the sensor with wiring (Nief *et al.*, 2019). Examples of these digital sensors include the MB3 digital microbarometer (MB3d), which includes a digitizing block attached to the analog transducer block, and the Hyperion model 5200 series. Both of these are examples of sensors designed to meet IMS specifications for global nuclear monitoring. A visual representation of the block components of the MB3d is shown in Figure 1.3. In this dissertation, the evaluation of the MB3d against legacy sensor systems in the digital domain is presented in Chapter 2.

Figure 1.3. MB3 digital microbarometer (MB3d); a digital infrasound sensor designed to meet IMS specifications. The sensor consists of a transducer block (bottom) with an aneroid capsule coupled with a magnet-and-coil transducer. A secondary coil wrapped around the main one ensures remote calibration capability. The second block of the sensor is the digitizing block (top), which samples the analog output of

the transducer block with a low consumption high performance analog-to-digital converter (ADC) and provides Global Positioning System (GPS) timestamps (Larsonner *et al.*, 2014).

Another example of contemporary digital acoustic sensors is smartphone built-in microphone sensors. With the important distinction that these sensors are designed for speech transmission instead of IMS standards, these ubiquitous sensors show increasing promise as reliable sensing systems within the acoustics community. Chapter 3 of this dissertation explores novel characterization methods for smartphone built-in microphone sensors. Smartphone-based acoustic sensors are of interest due in large part to their accessibility, low cost, and efficiency at time of deployment. Furthermore, smartphones have their own versions of the three main components needed for a traditional infrasound station to become fully operational: power, acquisition, and communications. A smartphone's power system is its rechargeable battery, and its communications system is the access to wireless networks or cell communications. As for acquisition, smartphones have embedded pressure sensors, such as microphones and barometers, and analog-to-digital converters.

In this dissertation, smartphones are presented as acoustic sensing systems for infrasound and low-frequency detection. The *Redvox Infrasound* app (Redvox, 2018) is used to measure acoustic data with the built-in pressure sensors of the smartphones. Figure 1.4 shows the global device collection of smartphones running on iOS and Android operating systems that have been used at some point for the purposes of acoustic measurements with the *Redvox* app. The figure shows smartphone usage in every continent in the globe. As the demand for consumer mobile devices continues to rise globally, smartphones show promise as supplementary systems for regional and global infrasound networks.

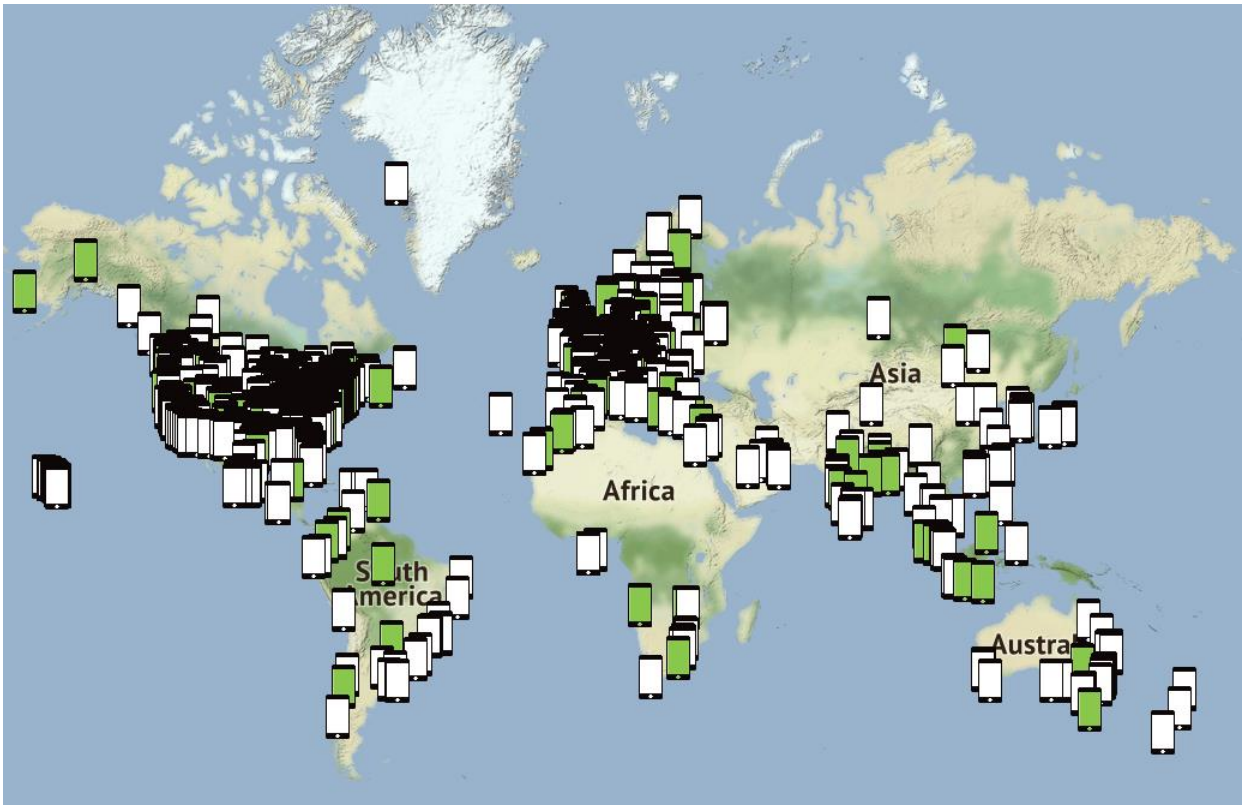

Figure 1.4 Global device collection of smartphone devices that have been used for the purposes of acoustic measurements with the *Redvox* app. Smartphone icons in white represent devices running on iOS software from June 2015 to December 2018 while those in green represent devices running on Android software from June 2017 to December 2018 (redvox.io).

1.3 Digital Signal Processing

1.3.1 Sampling and quantization

An acoustic sensor's output is a continuous-time signal represented as voltage as a function of time. This signal can be *digitized* for digital computers and interfaces to interact with the analog information obtained from the physical world. The amount of information contained in a *digital* or *discrete-time* signal is constrained by the *sampling frequency*, number of *bits* (binary value: 0 or 1) per sample, and *analog anti-aliasing filter* (Smith, 1999). The *sampling frequency* dictates how often a signal is sampled in samples/second; this *sampling* process converts the independent variable (i.e., time) of the analog signal from continuous to discrete. The number of *bits* determines the precision with which each sample of the dependent variable (i.e., voltage) of the analog signal will be *quantized*, namely, mapped to a discrete level represented by a sequence of bits. A device that performs digitization of an output analog signal from a sensor is referred to as a *digitizer*. The *least-significant-bit* (lsb) of a digitizing system is the smallest step that can be represented by the digital output word, and is often referred to as a *count*. Units

of lsb are a measure of the distance between adjacent quantization levels. The *bit-weight* of a digitizer constrains the proportion of the digital output to the analog input, and is commonly measured in V/lsb.

In order to gather all the necessary information needed to reconstruct the analog signal constrained in the digital data, the signal must be sampled at a rate of at least twice the maximum frequency component of the input signal:

$$f_s \geq 2f_{max} \ , \tag{1.7}$$

where f_s is the sampling frequency and f_{max} is the maximum frequency component. This is known as the *Nyquist-Shannon Sampling Theorem* (Nyquist, 1928; Shannon, 1949). Failure to abide by this theorem's constrictions results in signal *temporal aliasing*; this phenomenon occurs when the reconstructed signal from the digital sequence is distorted, or different from the original analog signal (Oppenheim and Schafer, 1989).

Aliasing can be avoided by pre-filtering the analog signal prior to digitization with an *anti-aliasing* filter. This filter limits the analog signal bandwidth as constrained by the Nyquist-Shannon Sampling Theorem; it is a low pass filter that removes frequency components above one-half of the sample rate. The anti-aliasing filter roll-off usually starts around one third of the sample rate (Swanson, 2008).

1.3.2 Time-frequency analysis

Spectral analysis of acoustic signals is performed in the frequency domain in order to capture instructive acoustic features such as frequency, amplitude and phase relationships of the sound waves. This type of analysis is essentially a variance technique, and is based on the representation of the time series as a sum of sines and cosines of different frequencies and amplitudes. The *spectrum* of the time series is known as the sum of the frequency components of the time series, where each component represents the contribution that the frequency makes to the total variability of the series (Percival and Walden, 1993).

A raw pressure record as a function of time is known as the time domain representation of a sound signal. The frequency composition of the time signal can be obtained by performing Fourier analysis on the time record and is represented as a pressure-related value such as amplitude or power as a function of frequency. The most practical version of Fourier analysis consists of applying the *Fast Fourier Transform* (FFT) to the record, which is an efficient way to compute the *Discrete Fourier Transform* (DFT) on the time series for discretely sampled records. Eq. (1.8) shows the DFT $G(k)$ for a discrete time series $g(n)$

$$G(k) = \left(\frac{1}{N}\right) \sum_{n=0}^{N-1} g(n) e^{-2\pi jkn/N} \ , 0 \ \leq k \leq N-1, \tag{1.8}$$

where k is the discrete frequency and n the discrete sample in time.

The resulting relationship of a dynamic variable as a function of frequency is the spectrum, and represents an average of the frequency content of the signal over the entire record time. When the frequency-domain properties of the signal vary with time, a *spectrogram* is computed. In this process, the *short time Fourier Transform* (STFT) is applied to the record. The STFT is obtained by truncating the signal into windows of a chosen width. The FFT is applied to each window section, resulting in an array containing the spectrum for each time-frequency position (Randall, 2008; Oppenheim, 1989).

The STFT is limited by the time-frequency uncertainty principle, which states that the product of the time and frequency resolutions is constant. Thus, an increased resolution in the frequency domain is obtained at the expense of temporal resolution, and vice versa (Gabor, 1946). The resulting Fourier spectrogram obtained by applying the STFT algorithm to a discrete time record has uniform resolution in both time and frequency (Randall, 2008). The resolution in each domain is inversely proportional to the other. The temporal resolution T_w of the spectrogram is therefore determined by the minimum frequency f_{min} as $\frac{1}{f_{min}}$. While incredibly useful for tonal detections where high spectral resolution is desired, the STFT has limitations for transient signal analysis at very low frequencies and in cases where a high temporal resolution is desired. *Multiresolution* analysis (Garces, 2013) approaches this problem by using fractional octave bands and logarithmic frequency resolution. In this algorithm, the time window size is determined per frequency band, enough to allow for an adequate number of periods within the window.

1.3.3 Removing sensor responses from digital time-series data

When a sensor's response is flat (within 3 dB) within the bandwidth of the time series, a calibration or sensitivity value can be obtained from the response and directly applied to the data in order to obtain the original physical units. This calibration value can be obtained by evaluating the response H at the designated frequency f_{cal}; the digital time series $y[n]$ is then divided by this value to transform digital units (i.e., counts) to a physical unit such as pressure, as shown Eq. (1.9):

$$x[n] = \frac{y[n]}{H(j2\pi f_{cal})}\,. \tag{1.9}$$

For non-flat responses, the sensor's response can be removed by deconvolution; if the system response is known, the input digital time series $x[n]$ can be found by finding a solution to the convolution equation Eq. (1.1).

When spectral analysis is performed on the digital time series, the response $H(e^{j\omega})$ must be removed in the frequency domain. The response corrected power spectral density P'_{xx} can be obtained as

$$P'_{xx}(\omega) = \frac{P_{xx}(\omega)}{H^*(e^{j\omega})\cdot H(e^{j\omega})}\,, \tag{1.10}$$

where $P_{xx}(\omega)$ denotes the raw power spectral density, ω the discrete frequency in radians, and $H^*(e^{j\omega})$ the complex conjugate of the frequency response (Merchant and Hart, 2011).

1.4 Data science approach in mobile global networks

The collection of acoustic data through crowdsourcing schemes with multi-sensing smartphones results in broadband mobile networks. This introduces a versatile global infrastructure that internally generates vast amounts of semi-structured network-level (e.g., user id, location, device OS and type, etc.) and app-level (e.g., sensor payload, sampling rate, etc.) data streaming at high velocities (Yazti and Krishnaswamy, 2014). The diverse embedded sensors and features of each smartphone in a network introduce veracity (e.g., timing, accuracy, response, etc.) and variety (e.g., data from different sensors, data in different formats, etc.) related issues into the incoming data as well. In order to extract meaningful knowledge and insights from the incoming streams of data from mobile networks in real-time, data collection, streaming, and analysis protocols need to be modernized. The combination of emerging technologies such as Big Data Analytics, Data Science, and Cloud Computing address these modern issues that have emerged with the integration of mobile multi-sensing systems in the scientific community.

Legacy sensing systems, such as the IMS, use on-site databases for data storage and processing. For the IMS, the data is received, stored, and processed in near-real-time at the International Data Centre (IDC). The infrasound station data frames are automatically checked for quality in batches of 30-minute intervals, after which event detection analysis and fusion with the other IMS technologies is performed (Mialle *et al.,* 2019).

In more modern systems, Cloud Computing services are used. This technology consists of using a network of remote servers hosted on the Internet (i.e., “the cloud”) for the storage, processing, analysis, and sharing of data. This method eliminates the cost of setting up on-site software and hardware required by traditional databases, while offering the needed speed and geographical flexibility for vast amounts of scalable computing resources (Amazon Web Services, 2018; Microsoft Auzure, 2018). Web services commonly provide application programming interfaces (APIs), which are the communication intermediaries between mobile apps and remote servers. These APIs allow for data requests in a semi-structured format, which in turn allows for metadata and payload extraction through software development kit (SDK) readers. Server and app communicate with data packets, which contain header and payload information. Data science methods aim to extract insightful knowledge from structured, semi-structured, and unstructured data sets (Grus, 2015). Namely, Data Science encompasses challenges ranging from data collection, to analysis, visualization, and data-driven decision-making capabilities.

Traditional data analytics methods are inadequate when faced with multi-sensing mobile sensor networks for several reasons. First, traditional data analytics deals with structured data in limited stream batches. App-based data from smartphones, however, is generally unstructured and streams at large volumes and high velocities. Second, data analysis is traditionally confined to a single database or department unit, and is limited in its capability to provide useful information in real-time from a global perspective (He *et al.,* 2016). When Cloud Computing technologies are being used, a dynamic and scalable data analysis system is needed to provide real-time information at a global scale. Third, traditional analytics methods are aimed for persistent stations streaming continuously, and are hardly

suited for mobile stations running with intermittent sensors. Data science techniques are necessary to assess the veracity of the data and filter the streams.

Chapter 4 of this dissertation describes a data science approach for extracting useful information from large amounts of semi-structured data. The data originate from mobile devices running the *Redvox* app, and are stored in distributed remote databases. A data science approach essentially consists of building scalable algorithm solutions for data management and analytics, and deploying these algorithms in a production system (Lo, F., 2018). The production system for *Redvox* app data is a collection of cloud-based services that enable data acquisition, storage, analysis, and product reporting (Christe *et al.*, 2018). Data products resulting from these approaches are technical assets, that can be leveraged at wide scale, and that utilize data as input and process that data to return algorithmically generated results. These results can then be used to steer data-driven decision-making capabilities.

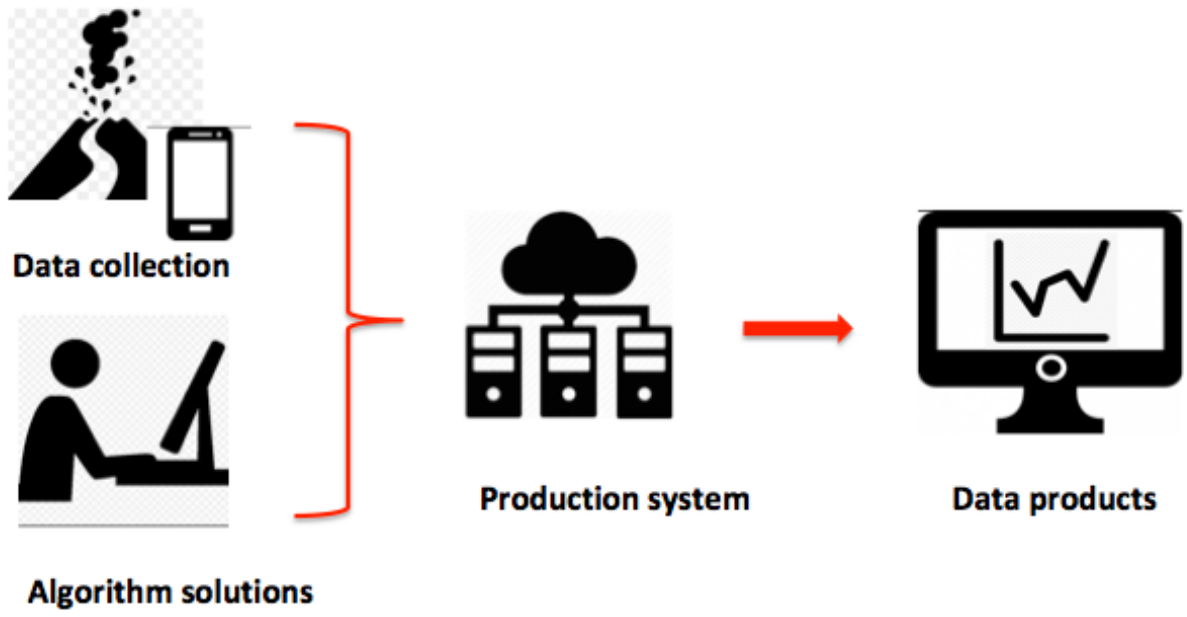

Figure 1.5. Illustration of data science life cycle in mobile sensor networks. The data originate from mobile devices running the *Redvox* app. The first stage of the cycle consists of collecting the data and building algorithmic solutions. In the **data collection** part, the embedded sensors of the mobile device gather information from its physical surroundings, and the information is stored by the app in API format. The data scientist builds **algorithm solutions** for the management and analytics of the semi-structured API-formatted data. The algorithms are deployed in the **production** system, which is a collection of cloud-based services that enable data acquisition, storage, analysis, and product reporting. The resulting **data products** are technical assets that can be used to steer data-driven decision-making capabilities. These products are accessible by users via an interactive web interface.

1.5 Dissertation Overview

This dissertation aims to contribute to the modernization of infrasound systems by presenting novel characterization and analytics approaches for the new generation of sensors. In Chapter 2, a method is presented for characterizing acoustic sensors in the digital domain against analog legacy systems. Chapter 3 presents a method for estimating amplitude responses of smartphone built-in microphone sensors in non-isolated conditions using conventional consumer products. Chapter 4 focuses on approaches for real-time monitoring and acoustic analysis in multi-sensing mobile sensor networks. Chapter 5 summarizes the main results and findings, future work, and implications of the presented research.

CHAPTER 2. DIGITAL ACOUSTIC SENSOR PERFORMANCE ACROSS THE INFRASOUND RANGE IN NON-ISOLATED CONDITIONS

Published as: Asmar, K., Garcés, M., Hart, D., and Williams, B. (2018) “Digital acoustic sensor performance across the infrasound range in non-isolated conditions” *J. Acoust. Soc. Am.* 144(5), 3036-3045

Abstract

The next generation of acoustic sensors is emerging to supplement legacy sensors traditionally used in regional and global networks. These devices operate under similar principles as traditional sensors, without the need of a separate external digitizer. The calibration of these sensors against their predecessors is crucial to the modernization of conventional technologies. This work describes the characterization of the next-generation MB3 digital microbarometer and the iPrecision smartphone microphone in a non-isolated calibration room across the infrasound (i.e. 0.01 – 20 Hz) range. The intent is to evaluate nominal instrument performance before deployment. A portable rotary subwoofer is used as a controllable infrasound source to generate single-tone sinusoidal and broadband noise pressure waves in a room configured for calibration purposes. For each device, comparison measurements are made, from which the digital sensitivity and the parametric response is developed. The results provide insight into the performance of the sensors in non-isolated environments. By overlapping the responses of the test sensors, digital sensor performance across the infrasound range can be benchmarked. These responses may serve as a double-reference scheme in future pressure measurements and digital calibrations of acoustic sensors.

2.1 Introduction

Acoustic sensors use different mechanisms to convert input pressure fluctuations into output analog or digital signals. In order to ensure that the end result of this conversion accurately represents the incoming pressure field, it is necessary to properly characterize and calibrate the sensors performing the measurements (Marcillo *et al.*, 2012). This work describes the evaluation and characterization of two next-generation digital sensors across the infrasound range. These devices are part of a modern generation of acoustic sensors known for the integration of analogue-to-digital converters to provide digital data. Their significant reduction in size, weight, power, and cost, is also advantageous to data collection and shipping logistics. The calibration of these sensors could potentially contribute to the modernization of conventional acoustic sensing technologies. Though numerous analog acoustic calibrations and chamber tests have been performed and are described in the literature, the calibration methods described in this study focus on the evaluation of the *digital* output of the test sensors relative to established analog reference sensors connected to external digitizers. We define the *digital sensitivity* of an acoustic sensor system (i.e., transducer plus digitizer) as the ratio of the input pressure to the system's digital output. We develop response models for the digital acoustic sensors in terms of *digital gain*, which we define as the ratio of the system's digital output to the input pressure (i.e., the inverse of the digital sensitivity). We use a portable rotary subwoofer (which will be described in Section 2.2) as a controllable infrasound source (Park *et al.*, 2009a) in calibration experiments performed in non-isolated conditions.

The first test sensor is the MB3 digital microbarometer (MB3d), an infrasound sensor developed by the Commissariat à l'Énergie Atomique (CEA) to meet the Comprehensive Nuclear-Test-Ban Treaty (CTBT) International Monitoring System (IMS) requirements. This sensor is a newer version of the MB2000 and MB2005 series (Seismowave, 2015). IMS sensors are designed to operate with an enhanced response within the 0.02 – 4 Hz pass band. A notable feature of the MB3d is the integration of an on-board, low-noise 24-bit analog-to-digital converter (ADC) for digital output. The digitizing block of the MB3d permits time synchronization with Universal Coordinated Time (UTC), which is performed by a time tagging board with pulse per second (PPS) capability. When connected to a Global Positioning System (GPS) antenna, the digitizing block provides digital data outputs with GPS timestamps, which are known to be accurate to the order of milliseconds. The Hyperion Model 5200 series is another example of an existing digital infrasound sensor manufactured for explosion monitoring. Aside from reduced size and weight, the MB3d is reengineered to use a Linear Variable Differential Transformer (LVDT) as opposed to a magnet and coil velocity transducer. This last feature is essential for lowering the self-noise of the sensor in the upper passband. The analog version of the MB3d (i.e., the MB3a) was evaluated by Merchant and McDowell (2014) and Larsonner *et al.* (2014). Although the MB3d and MB3a share the same transducer block and analog response, the digital output of the MB3d is constrained by its embedded digitizer. In this study, we characterize the MB3d digital response against its MB2000 analog predecessor (CEA/DAM, 2009) connected to a conventional 24-bit digitizer Reftek Model 130 (Refraction Technology Inc., 2011) commonly used in field experiments.

The second test sensor is the iPrecision smartphone microphone (iMic) (Audio Control, 2018); a factory calibrated iOS condenser microphone with an embedded preamplifier and 24-bit analog-to-digital converter. This device is designed to operate with a flat (within 3 dB) amplitude response from 3 to 20,000 Hz. When connected to an iPhone or an iPad, it is able to bypass the analog electronic stages with a digital audio link and override the internal microphone. In this work, we use the *RedVox Infrasound app* for iOS (Redvox, 2018) to record acoustic signals measured by the iMic. This *app* displays the acoustic pressure recorded with the internal or external microphone as it streams the sound files anonymously to a cloud server for analysis. In this work, we describe the response of the system consisting of the iMic sensor connected to an iPhone 6s. The reference for calibrating the iMic at higher frequencies is the Brüel & Kjaer (B&K) Low-frequency Pressure-field ½'' Microphone Type 4193 (Brüel and Kjaer, 1995), which will be described in Section 2.4. B&K microphones are commonly used as references in acoustic calibration processes (Larsonner *et al.*, 2014 and Ollivier *et al.*, 2012) due to their long-established stability and reliability.

This article describes the evaluation and characterization of these next-generation digital sensors against legacy analog sensors configured with external digitizers in a non-isolated calibration room across the 0.01 – 20 Hz passband. Section 2.2 describes the experimental and processing methods applied in the calibration tests and analyses. Section 2.3 describes the characterization of the MB3d sensor against its analog MB2000 predecessor across 0.01 – 4 Hz. We evaluate an analog Brüel & Kjaer Microphone Type 4193 against the MB3d in the common passband (0.25 – 4 Hz) in Section 2.4. This Brüel & Kjaer microphone is then chosen as a reference for calibrating the iMic sensor. Section 2.5 subsequently focuses on the calibration of the iMic flat amplitude response against the Brüel & Kjaer sensor across 1 – 20 Hz. We summarize our observations in Section 2.6 and comment on the applications of our results.

2.2 Methods

The performance evaluation of the acoustic sensors described in this work took place in a ~10.7 x 7.3 x 3.0 m^3 non-isolated calibration room. External factors such as wind, ambient, and cultural noise were therefore components in the acoustic measurements. All acoustic signals were generated with a Tektronix RM 3100 signal generator. A Thigpen Rotary Woofer Model 17 (TRW-17) (Eminent Technologies, 2018 and Park and Robertson, 2009) was used as the sound projector for frequencies lower than 20 Hz. The TRW-17 is essentially a rotating fan, driven by an electric motor, with blades that pitch dynamically in response to an applied signal. While the fan rotates at constant frequency, an input signal is fed into the system's audio amplifier, which drives a conventional electromagnetic coil assembly. The longitudinal motion of the coil is then converted to rotational motion of the blades (Park *et al.,* 2009). The result is a sound pressure wave propagating at a frequency determined by the input electrical signal. The TRW-17 described in this study is configured so that it radiates into the calibration room, while a room of dimensions ~ 8.8 x 6.6 x 3.0 m^3 forms the back volume. Sensors were placed at an approximate distance of 5 meters from the TRW-17 in the calibration room. Three types of tests were performed to

assess the response of the sensors. Analog and pressure chamber versions of these tests, described in Sections 2.2.1-2.2.3, are presented in Kromer *et al.* (2007).

Each acoustic sensor's frequency response is defined parametrically as a function of angular frequency ω in terms of amplitude or gain k, poles p_i and zeros z_i (Merchant and Hart, 2011) as

$$H(e^{j\omega}) = k\frac{\prod_{i=1}^{i=N_{zeros}}(j\omega - z_i)}{\prod_{i=1}^{i=N_{poles}}(j\omega - p_i)}. \quad (2.1)$$

A *pole-zero model* commonly consists of a gain value and the locations of poles and zeros for a specific sensor's frequency response. The poles are usually represented in radians as $-2\pi f_{hz}$, where f_{hz} is the pole frequency in Hz. In order to compute the response corrected auto and cross spectra, the units of the gain *k* must be scaled to obtain final spectra with Pa^2/Hz units. The *least significant bit* (lsb) of a digital system is the smallest step that can be represented by the digital output word of the Analog-to-Digital Converter (ADC), and is often referred to as a *count*. Lsb is defined as the full-scale voltage input limit of the ADC divided by the bit resolution of the ADC. For digital data outputs, the gain *k* must have units of lsb/Pa. When the analog gain in V/Pa is provided for a sensor's response, it is divided by the corresponding digitizer's ADC resolution in V/lsb to obtain units of lsb/Pa.

The response corrected auto and cross spectra between two time series *x* and *y* are computed as

$$P'_{xx}(f) = \frac{P_{xx}(f)}{H_x^*\left(e^{\frac{j\omega}{2\pi}}\right)H_x\left(e^{\frac{j\omega}{2\pi}}\right)} \quad (2.2)$$

and

$$P'_{xy}(f) = \frac{P_{xy}(f)}{H_x^*\left(e^{\frac{j\omega}{2\pi}}\right)H_y\left(e^{\frac{j\omega}{2\pi}}\right)}\ , \quad (2.3)$$

respectively. H^*denotes the complex conjugate of the frequency response H, f is the frequency in Hz, $P_{xx}(f)$ is the raw auto spectra of time series *x* (the same principle can be applied to time series *y*), and $P_{xy}(f)$ is the raw cross spectra between both time series.

2.2.1 Digital sensitivity measurement test

This test uses sinusoid pressure waves at multiple discrete frequency values to measure the digital sensitivity of an acoustic sensor relative to a reference sensor. Single octave center frequency tones are generated with the signal generator; input sinusoidal parameters are 1Vpp amplitude, 0 phase, and 0 offset. More than 100 cycles of each tone are recorded. An octave band pass filter is first applied to each tone data with corner frequencies at $G^{-1/2N}f_0$ and $G^{1/2N}f_0$, where $G = 10^{0.3}$, $N = 1$ and f_0 is the octave center (i.e., tone) frequency (Garcés, 2013). Digital data records are then sliced into segments of user-specified consecutive cycles. In this study, data segments were set to 20 cycles. A 3-parameter

sine-fit algorithm (Merchant and Hart, 2011) is performed on the data segments to compute the sinusoidal amplitude and RMS error. Selected results are those with the highest signal-to-noise ratios. The sine-fit amplitude results for the reference sensor are multiplied by the sensor's digital sensitivity at the frequency of interest to obtain pressure units. The test sensor digital sensitivity is then estimated by dividing the reference amplitude in pressure units by the digital test amplitude.

2.2.2. Sensor frequency response test

This test uses a broadband noise pressure signal to verify the amplitude and phase response of a test sensor across the frequencies of interest relative to a reference sensor. A noise signal is generated by the signal generator with inputs 5 Vpp amplitude, 0 phase, and 0 offset; the signal is then fed into the rotary subwoofer for sound projection. The data from all sensors is retrieved as binary digital outputs and the response corrected auto and cross power spectra are computed. Raw spectra are first computed in lsb^2/Hz, and then corrected by the digital complex responses in lsb/Pa to obtain spectral units of Pa^2/Hz. All raw spectra are computed using Welch's method (Welch, 1967). The digital time series are first divided into 75% overlapping segments of the same size; the length of the segments is determined by the sample rate and desired spectral resolution. Each data segment is mean-subtracted and tapered with a *Hann* window of equal duration. The power spectrum is then computed by taking the square of the Fourier transform of the tapered and mean-subtracted data segments. To correct the spectral density for the windowing operation, each result is multiplied by a scaling factor $\frac{1}{fs \cdot \sum_{i=1}^{N} w^2}$, where *fs* is the sample rate and *w* is the windowing function of length *N*. The final power spectrum estimate is obtained by averaging the power spectra over the number of sections. All computed spectra are one-sided, where the power is attributed to positive frequencies only. Last, 95% confidence intervals (Bendat and Piersol, 1986) of the power spectra are computed as $\frac{n\hat{G}_{xx}(f)}{\chi^2_{n;0.025}} \leq G_{xx}(f) \leq \frac{n\hat{G}_{xx}(f)}{\chi^2_{n;0.975}}$, where *n* is twice the number of spectral averages, $G_{xx}(f)$ is the spectral density at a given frequency *f* and $\hat{G}_{xx}(f)$ its estimate, and χ^2_ν the chi-square distribution with ν degrees of freedom.

The last step is to compute the response corrected relative amplitude $M(f)$, relative phase φ, and coherence C_{xy} on each pair of sensors as

$$M(f) = 10\log_{10}\left(\frac{P'_{xx}(f)}{P'_{yy}(f)}\right), \tag{2.4}$$

$$\varphi = \arctan\left(\frac{Im(P_{xy})}{Re(P_{xy})}\right), \tag{2.5}$$

and

$$C_{xy}(f) = \frac{|P_{xy}(f)|^2}{P_{xx}(f)P_{yy}(f)} \ . \tag{2.6}$$

The normalized random error (Bendat and Piersol, 1986) of the coherence results is computed as $\frac{\sqrt{2}[1-C^2_{xy}(f)]}{|C_{xy}(f)|\sqrt{n_d}}$, where n_d is the number of spectral averages.

Given that the relative phase and coherence are functions of the cross spectrum, proper time alignment between the sensors must exist for the results from Eq. (2.5) and (2.6) to be accurate. Lack of time alignment, however, does not affect the auto spectrum of the individual sensors, and a reliable value of relative magnitude can still be computed if the coherence is high.

Spectral averaging over 1/3-octave bands (Garcés, 2013) is performed on coherence and relative response data in order to smooth random variations in the narrowband spectrum. The 1/3-octave bands are computed with corner frequencies at $G^{-1/2N} f_0$ and $G^{1/2N} f_0$, where $G = 10^{0.3}$, $N = 3$ and f_0 is the octave center. A relative amplitude of 0 dB across the common passband of the test and reference sensors indicates identical spectral amplitudes. Similarly, a relative phase of 0 degrees indicates identical spectral phase between the sensors. If the pole-zero model of the reference and test sensors perfectly represent their respective responses, then the relative amplitude and phase should be perfectly flat at 0 dB and 0 degrees, respectively (Merchant and McDowell, 2014).

2.2.3. Sensor self-noise test

This test measures the self-noise of a sensor in a non-isolated environment. The sensor is left to record data overnight with all its ports sealed. Response corrected power spectral density levels are then computed as described in Section 2.2.2.

2.3 Characterization of the MB3 digital microbarometer response across 0.01 – 4 Hz

The performance evaluation of the test sensor MB3d was assessed using a MB2000 as a reference. The MB2000 has a nominal analog sensitivity of 100 mV/Pa at 1 Hz, and was connected to 24-bit digitizer RefTek Model 130-01 with nominal manufacturer ADC resolution 1.589 μV/lsb. The MB3d is reported to have a nominal analog sensitivity of 20 mV/Pa at 1 Hz and a nominal ADC resolution of 2.356 μV/lsb. When both test and reference sensors digitize their analog signals through 24-bit systems, the nominal digital sensitivity of the MB3d is 7.4 times greater than the nominal digital sensitivity of the MB2000/Reftek system. Sample rates were set to 100 Hz and digitizer gain values were set to unity.

2.3.1 Digital sensitivity measurement

We obtained digital sensitivity values in Pa/lsb at 1, 2, and 4 Hz octave center frequencies for the MB3d test sensor relative to the MB2000. For this test, both sensors were placed with their ports capped on a padded surface to reduce vibration and connected to a manifold, which had one port open. The nominal digital sensitivity in Pa/lsb for the MB2000 was obtained by dividing the Reftek ADC resolution by the sensor's analog sensitivity. From the sine-fit results, we obtained digital sensitivities for the MB3d relative to the MB2000.

Table 2.1. Sine fit results with RMS error for MB3d digital sensitivity measurements. The algorithm's signal-to-noise values were 28 dB, 29 dB, and 39 dB at 1, 2, and 4 Hz octave center frequencies, respectively.

Frequency [Hz]	MB2000 pressure amplitude [Pa]	MB3d digital amplitude [lsb]	MB3d digital sensitivity [Pa/lsb]
1	3.430 $\pm$ 0.100	(3.085 $\pm$ 0.100)e+04	(1.112 $\pm$ 0.050)e-04
2	7.388 $\pm$ 0.200	(6.611 $\pm$ 0.200)e+04	(1.117 $\pm$ 0.050)e-04
4	3.759 $\pm$ 0.030	(3.320 $\pm$ 0.030)e+04	(1.132 $\pm$ 0.010)e-04

The digital sensitivity of the MB3d at 1 Hz was observed to be (1.112 $\pm$ 0.050)e-04 Pa/lsb, which deviates from its nominal 1.178e-04 Pa/lsb value by 5.6% (0.48 dB). Merchant and McDowell (2014) found the analog sensitivities at 1 Hz of two MB3a sensors to deviate from the nominal value by 6.0% (0.51 dB) and 1.5% (0.13 dB), respectively, when tested in an isolation chamber. The observed values at 2 and 4 Hz shown in Table 2.1 differed from the measured value at 1 Hz by 0.52% (0.05 dB) and 1.85% (0.16 dB), respectively. Across the 1 – 4 Hz octave passbands, the observed digital sensitivities of the MB3d were flat (within 3 dB), with an average value of (1.120 $\pm$ 0.070)e-04 Pa/lsb (4.88 % or 0.41 dB from nominal).

2.3.2. Sensor frequency response

We developed a pole-zero response model, described in Table 2.2, for the MB3d test sensor based on the CEA reported bandwidth and the measured digital sensitivity at 1 Hz. We subsequently verified the MB3d frequency response (shown in Figure 2.1) relative to the MB2000 using the same sensor configuration as in Section 2.3.1. In order to compare the digital outputs of the test and reference sensors, we scaled the nominal analog response model gain values in V/Pa provided by CEA to obtain digital gain units in lsb/Pa.

Table 2.2. Pole-Zero response model for the MB3d sensor. The pole and zero locations were kept nominal. The digital gain value in lsb/Pa was corrected based on the measured digital sensitivity at 1 Hz shown in Table 2.1.

Gain [lsb/Pa]	Zeros [rad]	Poles [rad]
1.527e+06	$0 + 0j$	$-2\pi(0.01 + 0j)$ $-2\pi(27.0 + 0j)$

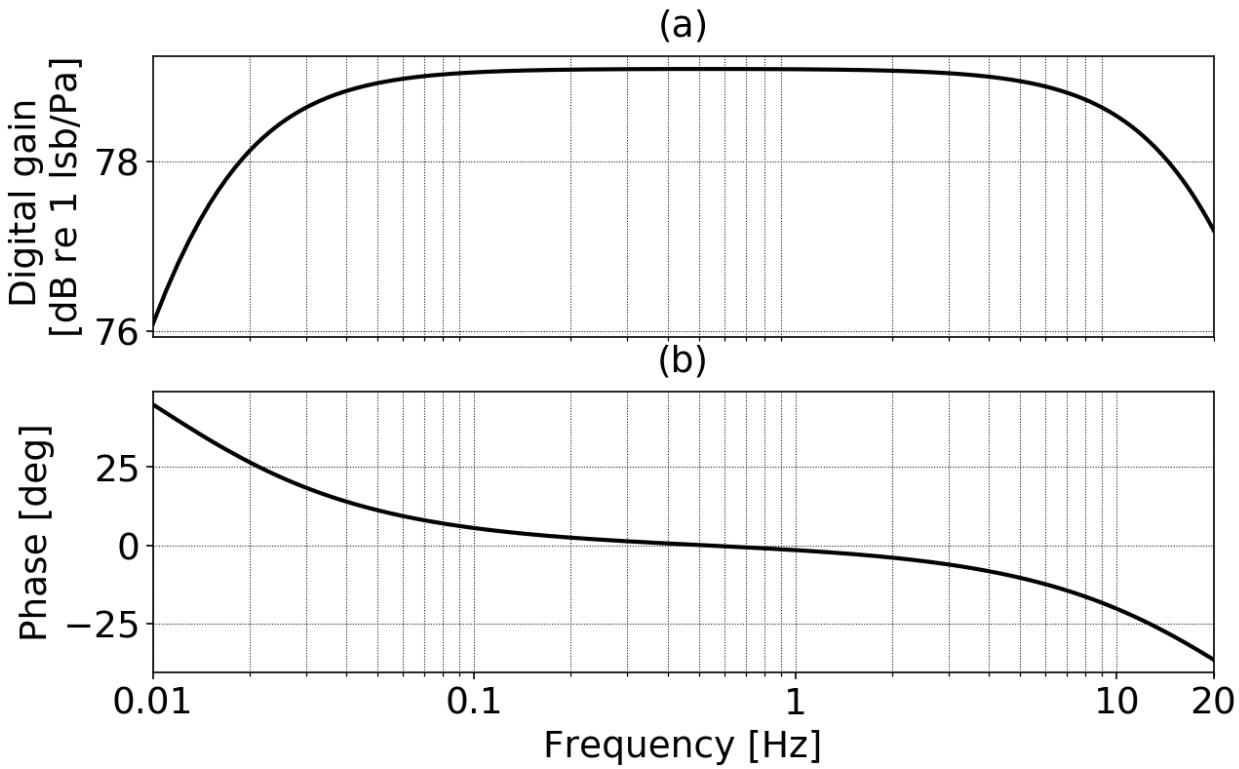

Figure 2.1. Frequency response of the MB3d sensor based on pole-zero model presented in Table 2.2. (a) Amplitude response in dB re 1 lsb/Pa. (b) Phase response in degrees.

For this test we generated a 30-minute acoustic noise signal and computed resulting Welch spectra with a Fast Fourier Transform window size of 16,384 samples (~164 seconds). This allowed for a spectral resolution of 0.01 Hz, with approximately 44 averages across the record. The sensor configuration was left as described in Section 2.3.1.

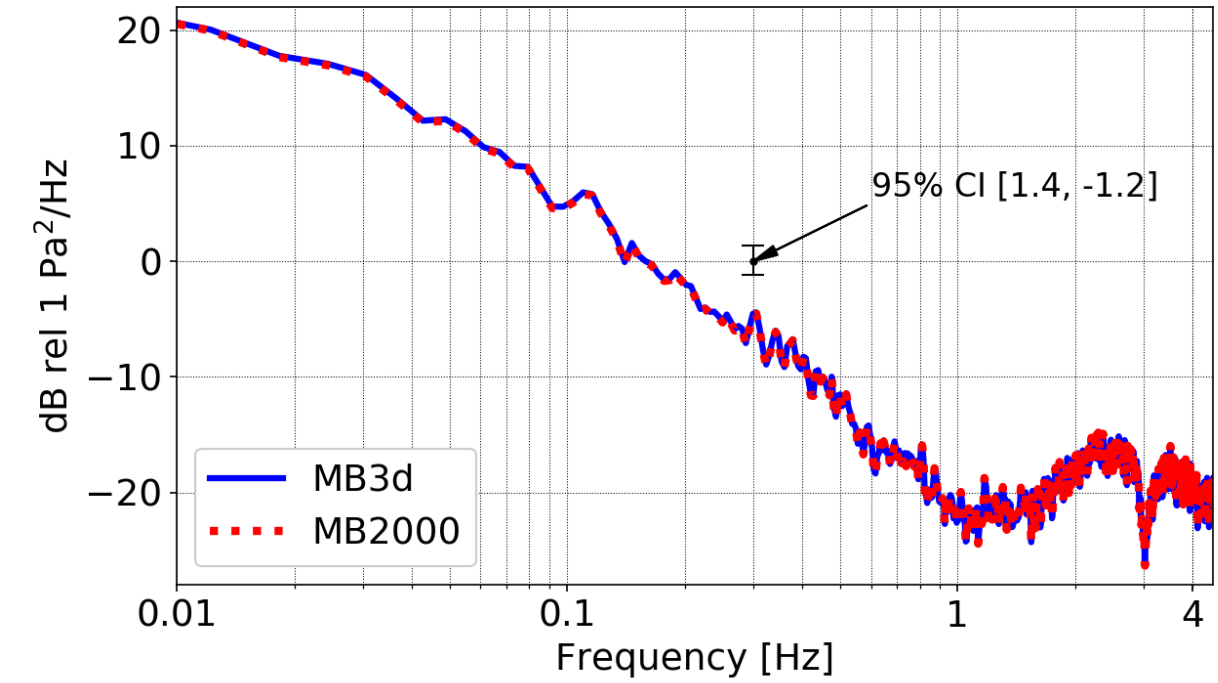

Figure 2.2. Noise power spectral density levels with 95% confidence interval (CI) [1.4, -1.2] dB re 1 Pa^2/Hz for MB3d and MB2000 across 0.01 – 4 Hz.

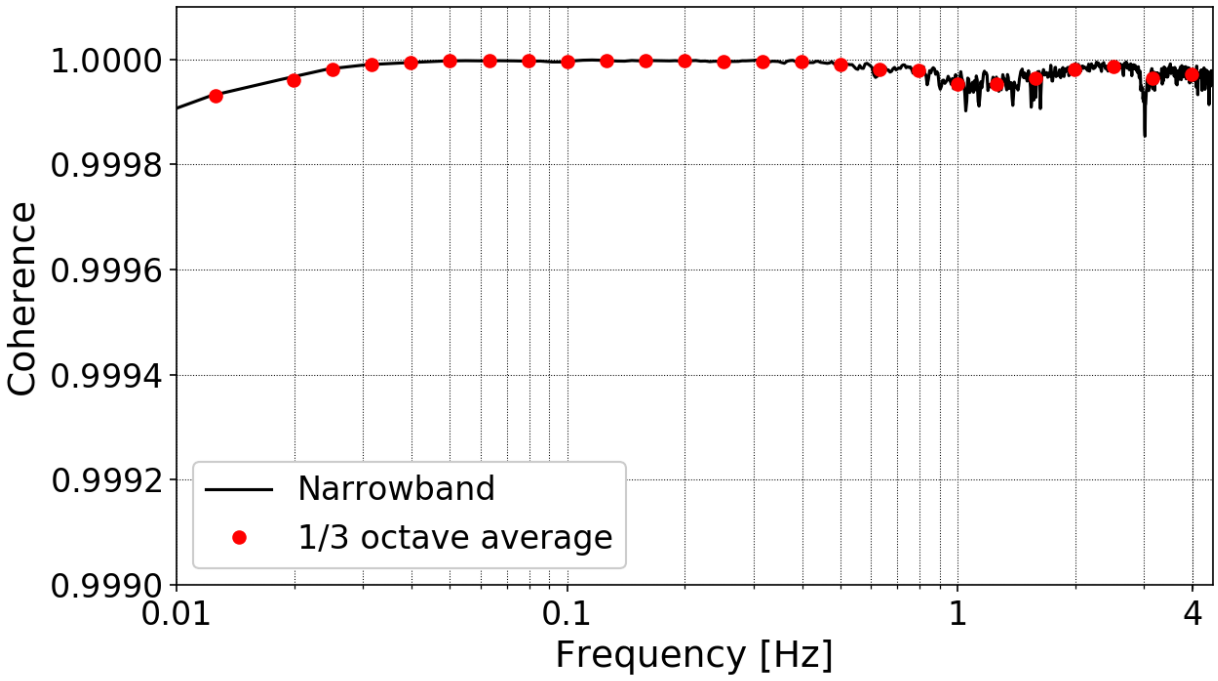

Figure 2.3. Noise coherence results for MB3d and MB2000 across 0.01 – 4 Hz. The solid line represents the coherence between the sensors. The filled circles represent 1/3-octave band averaging.

The noise power spectral density levels in Figure 2.2 and coherence analysis shown in Figure 2.3 indicate coherence above 0.99 between the MB3d test sensor and MB2000 reference sensor across 0.01 – 4 Hz, with normalized random error (5.4 $\pm$ 4.0)e-06. The high coherence among the sensors serves to validate the relative response results within the passband of interest.

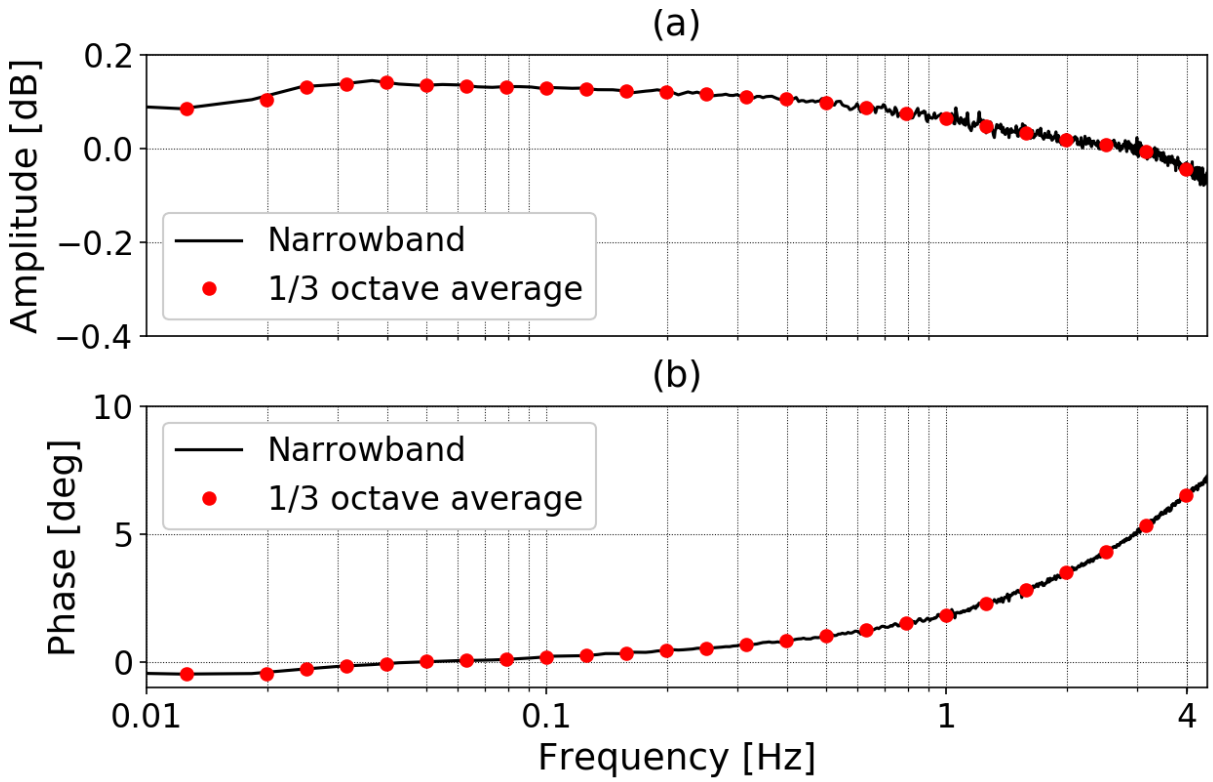

Figure 2.4. Noise response results for MB3d relative to MB2000 within the 0.01 – 4 Hz. (a) Relative amplitude between the sensors, computed as the ratio of their response corrected spectra. (b) Relative phase, computed as the angle of the response corrected cross-spectrum. Raw computations are represented by a solid line, while 1/3-octave band averaging is represented by the filled circles.

The relative amplitude 1/3-octave average results between the MB3 and MB2000 in Figure 2.4(a) are flat to within 0.14 dB (1.6 %) from 0.01 Hz up to the 4.0 Hz 1/3-octave band, with an observed 0.06 dB (0.75 %) bias at 1 Hz. Relative phase results, shown in Figure 2.4(b), show an average of 1.3 $\pm$ 1.8 degrees across the same pass band, with a value of 1.8 degrees at 1 Hz. The phase continues to rise above 1 Hz at a rate that suggests a time delay between the sensors of 5 milliseconds, which is likely due to different digitizing systems. Merchant and McDowell (2014) measured the relative response of two MB3a sensors against a MB2000 sensor in an isolated chamber when connected to a common digitizer

and found the relative magnitudes to be flat to within 0.3 dB (3.5%) and 1.15 dB (14.2%), respectively, across the 0.02 – 4 Hz IMS passband. The relative phase results found in the same study were seen to be flat to within 0.35 and 0.55 degrees, respectively.

The results show that the MB3d corrected digital response is consistent with its parametric response model in a non-isolated environment across 0.01 – 4 Hz. Relative response results satisfy the sensitivity and phase specifications for sensors used in the CTBTO (2001) network (± 0.45 dB and ± 5°, respectively, across the 0.02 – 4 Hz IMS pass band (Larsonner *et al.*, 2014).

2.3.3 Sensor self-noise

We measured and compared the self-noise of the sensors in a non-isolated environment. For this test, the sensors were disconnected from the manifold and left to record data overnight with their inlets sealed, using custom fittings for the MB3d.

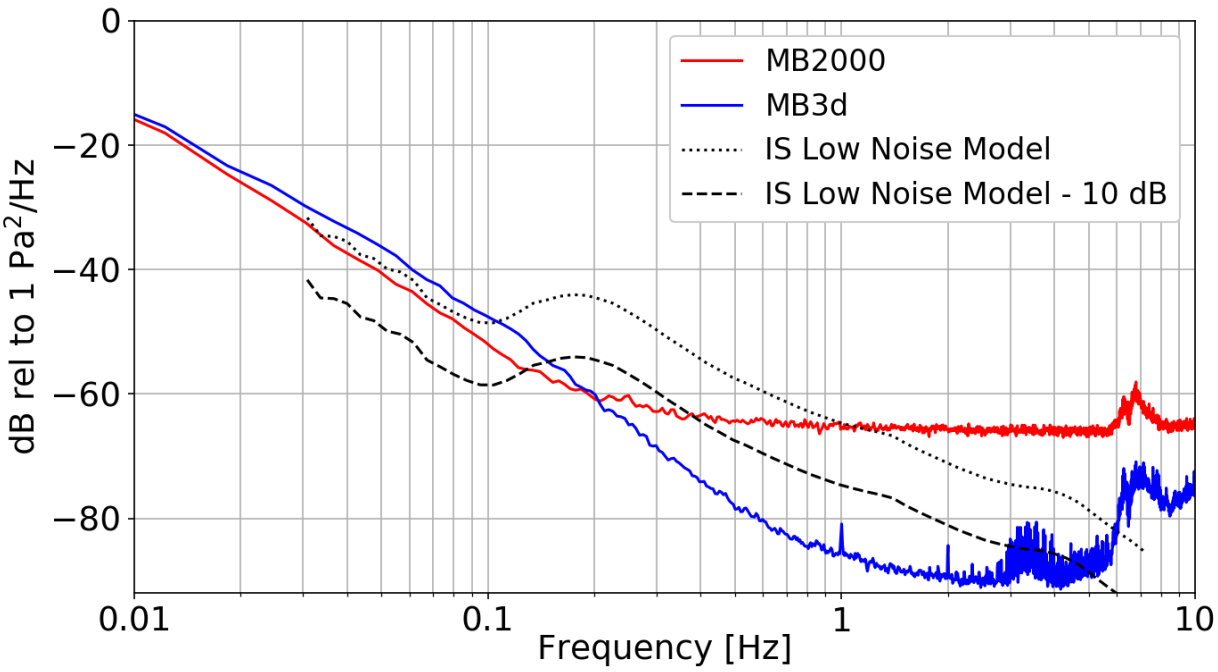

Figure 2.5. Response corrected self-noise power spectral density levels across the 0.01 – 10 Hz pass band for the MB2000 and MB3d, compared to the Infrasound Station (IS) Low Noise Model (LNM) established by Bowman *et al.* (2007). The CEA self-noise model for the MB3d sensor is more than 10 dB below the IS Low Noise Model. Data were acquired from 2 AM to 5 AM local time; this time period is known for low wind and cultural noise.

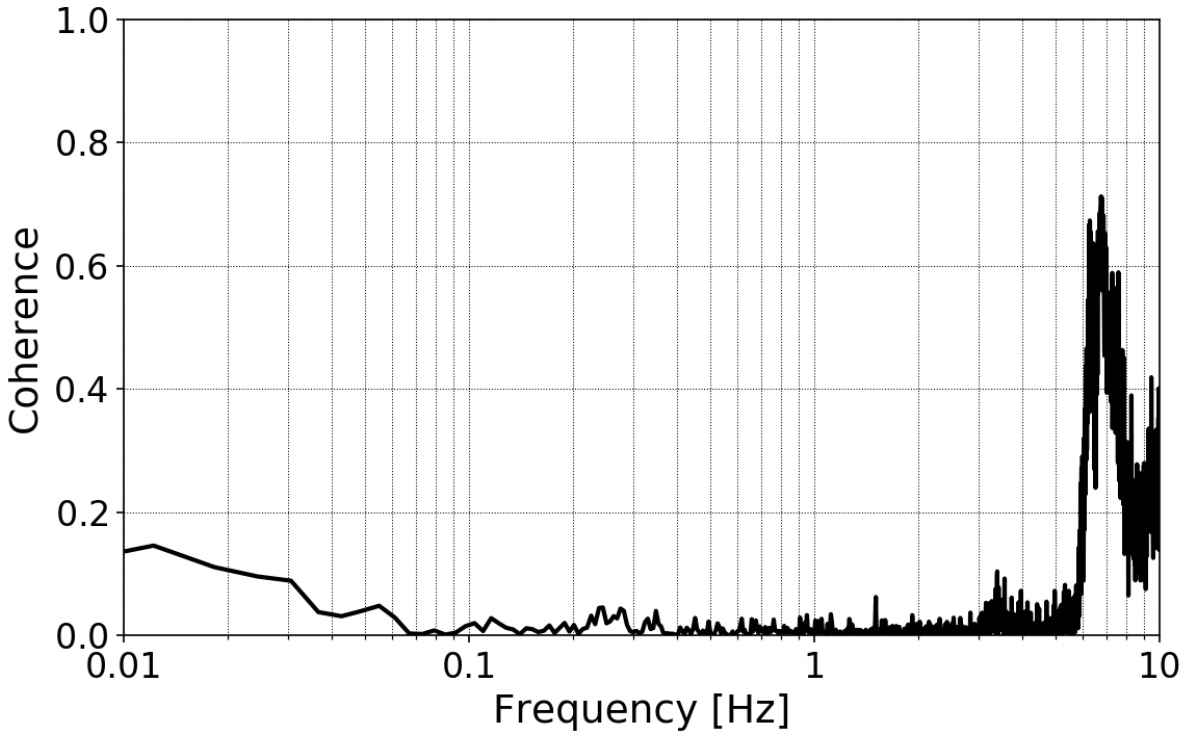

Figure 2.6. Self-noise coherence results between the MB3d and MB2000 across the 0.01 – 10 Hz pass band. Data were acquired from 2 AM to 5 AM local time; this time period is known for low wind and cultural noise.

Figure 2.5 shows isolated self-noise levels between the MB3d and MB2000 sensors. Coherence analysis results from Figure 2.6 show lack of coherence between the sensors across 0.1 – 6 Hz; this incoherence satisfies the requirement described by Kromer *et al.* (2007), in which there should be no coherent signal present among the sensors for proper self-noise measurements. Figure 2.5 shows the MB3d has a lower self-noise relative to the MB2000 above 0.2 Hz. The CEA self-noise model for the MB3d is more than 10 dB below the LNM in an isolation chamber; the results agree with the CEA self-noise model from 0.15 Hz to 4.0 Hz when averaged over 1/3-octave bands. The absence of microbarom infrasonic wave spectral curves across the 0.1 – 0.5 Hz passband (Christie and Campus, 2010) in Figure 2.5 suggests proper sealing of the inlets. The self-noise levels for the MB3d in Figure 2.5 are more than 10 dB above its CEA model across the 0.01 – 0.15 passband; coherence analysis in Figure 2.6 also shows a slight coherence increase below 0.07 Hz. We suspect this discrepancy from the CEA noise-model across the 0.01 – 0.15 Hz passband is due to low-frequency atmospheric background signals feeding into the sensors in a non-isolated environment; these signals are usually attenuated inside isolation chambers.

Two unique spikes at 1 and 2 Hz can be discerned in the MB3d self-noise levels shown in Figure 2.5. The sensor's embedded Global Positioning System (GPS) is known to sample at 1 pulse per second (PPS). The 1 Hz spike is likely due to GPS sampling, while the 2 Hz spike corresponds to the first overtone. Both spikes are below the sensor's noise model levels. The MB3d self-noise across the 1.0 Hz 1/3-octave pass band (i.e. -84.92 dB) exceeds the IMS requirement of at least 18 dB below LNM at 1 Hz. Increased self-noise levels are seen for the MB3d sensor above 4 Hz when averaged over 1/3-octave bands, with a sharp increase on both sensors at 6 Hz. Coherence analysis results in Figure 2.6 also show an abrupt increase in coherence between the sensors at 6 Hz. This suggests the presence of an external acoustic or seismic signal feeding into the sensors. Merchant and McDowell (2014) found the seismic sensitivity of the MB3a sensor to be visible in power spectra at frequencies above 4 Hz. The MB3a and MB3d sensors share the same magnet and coil velocity transducer, which is more sensitive to seismic vibrations when compared to the LVDT of the MB2000. We hypothesize the high self-noise levels of the MB3d above 4 Hz are due to seismic vibrations. The results show that the MB3d is consistent with its manufacturer noise model in a non-isolated environment from 0.15 to 4 Hz; low-frequency atmospheric background signals and seismic sensitivity are self-noise increasing agents in the field.

2.4. Evaluation of the analog Brüel & Kjaer Microphone Type 4193 microphone response above 0.25 Hz

We obtained a digital sensitivity value and measured the response of the Brüel & Kjaer (B&K) Microphone Type 4193 test sensor against the MB3d, which was considered in Section 2.3. The B&K sensor consists of an externally polarized analog microphone specially designed for infrasound, sonic boom, and pressure field measurements. The test sensor B&K Microphone Type 4193 was configured with infrasound adaptor UC-0211. We attached it to B&K Preamplifier Type ZC-0032, which was inserted to B&K Hand Held Analyzer Type 2250. Digitization of the B&K microphone data took place in the 24-bit digital interface embedded in the B&K Hand Held Analyzer Type 2250. We connected the MB3d and B&K sensors to a manifold and disconnected the B&K from power. All remaining ports on the MB3d were sealed, and one port was left open on the manifold. The MB3d sample rate was set to 20 Hz and unity digitizer gain. The B&K recorded at its lowest sample rate of 8,000 Hz. In order to correct for the time between the test and reference sensors, we performed time correlation analysis on 30-second window containing the noise signal described in Section 2.4.2. The MB3d data were upsampled to 8,000 Hz in this particular process to obtain better time alignment. We preprocessed B&K data in this section by shifting the waveform by the delay found in the time correction algorithm, then downsampling the record to 20 Hz (with a decimation factor of 400) to match the MB3d sample rate, and reversing the polarity to match MB3d sensor polarity.

2.4.1 Digital sensitivity measurement

We obtained the digital sensitivities in Pa/lsb at 1, 2, and 4 Hz for the B&K test sensor relative to the MB3d values shown in Table 2.1. We found in Section 2.3.3 that the seismic sensitivity of the MB3d

and MB2000 sensors increases above 4 Hz, which would make sinusoidal measurements with these sensors at 8 and 16 Hz unreliable.

Table 2.3. Sine fit results with RMS error for B&K digital sensitivity measurements. The algorithm's signal-to-noise values were 38 dB, 38 dB, and 40 dB at 1, 2, and 4 Hz octave center frequencies, respectively.

Frequency [Hz]	MB3d pressure amplitude [Pa]	B&K digital amplitude [lsb]	B&K digital sensitivity [Pa/lsb]
1	10.72 $\pm$ 0.10	(1.191 $\pm$ 0.010)e+04	(9.002 $\pm$ 0.100)e-04
2	7.029 $\pm$ 0.100	(7.801 $\pm$ 0.070)e+03	(9.010 $\pm$ 0.200)e-04
4	5.020 $\pm$ 0.040	(5.545 $\pm$ 0.040)e+03	(9.054 $\pm$ 0.100)e-04

The digital sensitivity of the B&K at 1 Hz was observed to be (9.002 $\pm$ 0.100)e-04 Pa/lsb, with deviations of 0.09% (0.01 dB) and 0.58% (0.05 dB) at 2 and 4 Hz, respectively (see Table 2.3). Across the 1 – 4 Hz octave passband, the observed digital sensitivities of the B&K were flat (within 3 dB). These results suggest that the B&K response is consistent with its manufacturer response model, which specifies a flat response from below 1 Hz up to 20,000 Hz.

2.4.2 Sensor frequency response

We developed a pole-zero response model for the B&K sensor, described in Table 2.4, and verified it against the reference MB3d sensor. The B&K 4193 test microphone calibration sheet specifies a flat response beyond 4,000 Hz, with a 3 dB low-end at 0.029 Hz. However, when connected to the preamplifier and hand held analyzer, the low corner frequency of the sensing system is between 0.1 and 1 Hz. We generated a response for the test sensor consistent with the measured digital sensitivity from Table 2.3 and the observed roll-off at the low corner frequency end. The response is shown in Figure 2.7. Sensor configuration was kept as described in Section 2.4.1.

Table 2.4. B&K Pole-Zero response model based on the digital sensitivity at 1 Hz presented in Table 2.3 and the observed low corner frequency roll-off at 0.25 Hz.

Gain [lsb/Pa]	Zeros [rad]	Poles [rad]
1.145e+03	0 + 0j	$-2\pi(0.25 + 0j)$

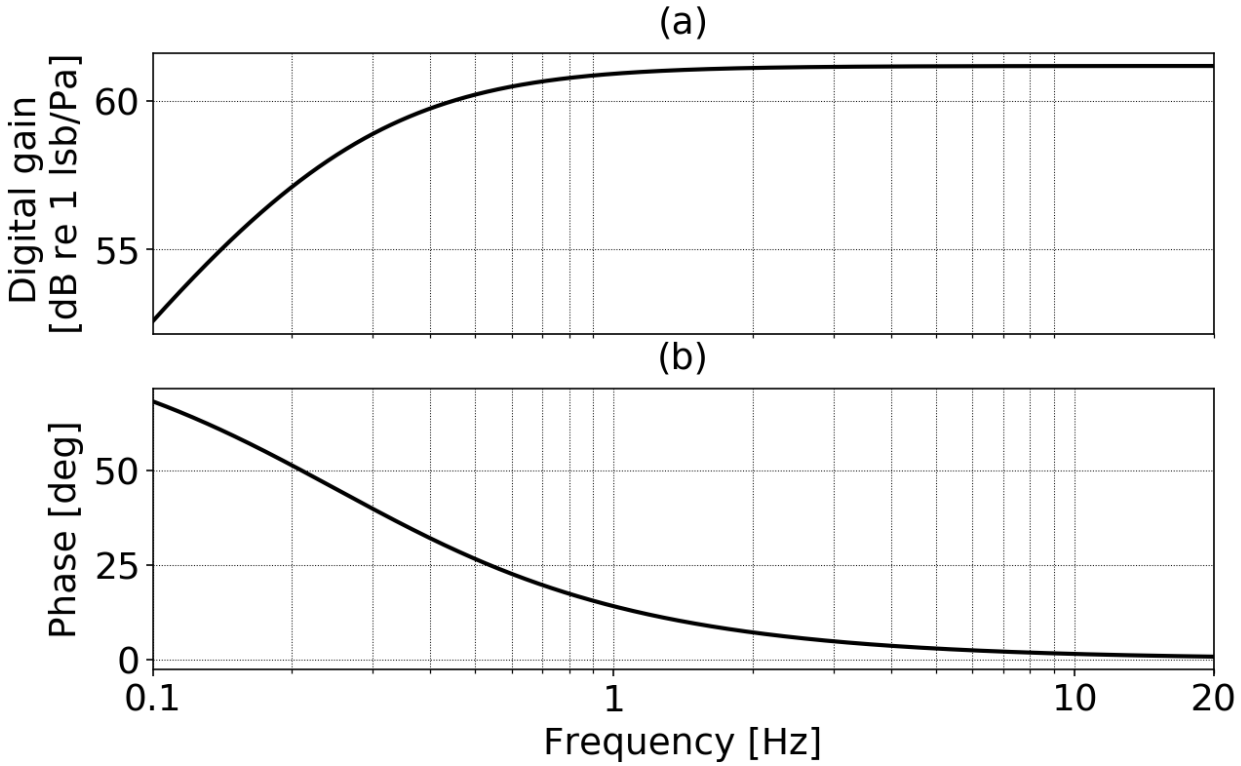

Figure 2.7. Frequency response of the B&K sensor based on pole-zero model presented in Table 2.4. (a) Amplitude response in dB re 1 lsb/Pa. (b) Phase response in degrees.

For this test, we generated a 10-minute noise acoustic signal and computed resulting Welch spectra with a Fast Fourier Transform window size of 4,096 samples (~205 seconds). This allowed for a spectral resolution of ~0.01 Hz, with approximately 12 averages across the record. The low spectral resolution permits a coherence analysis with higher accuracy across the frequency bands at the expense of increasing the 95% confidence interval.

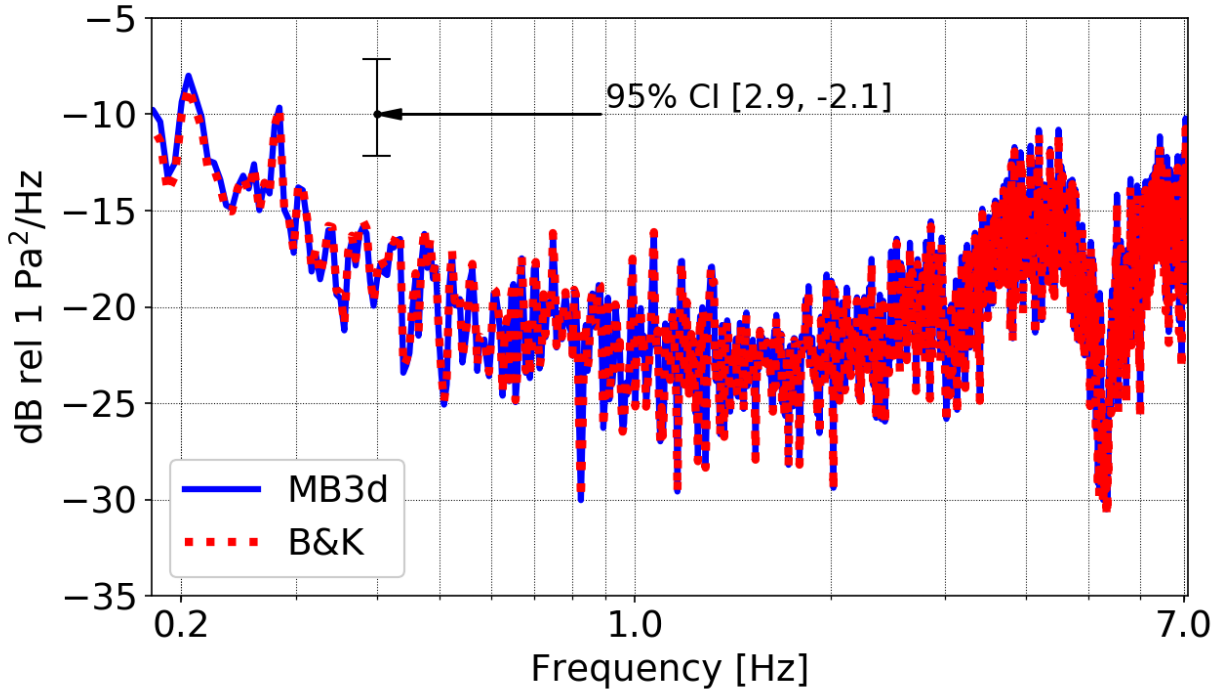

Figure 2.8. Noise power spectral density levels with 95% confidence interval (CI) [2.9, -2.1] dB re 1 Pa^2/Hz for B&K and MB3d across 0.18 – 7.1 Hz.

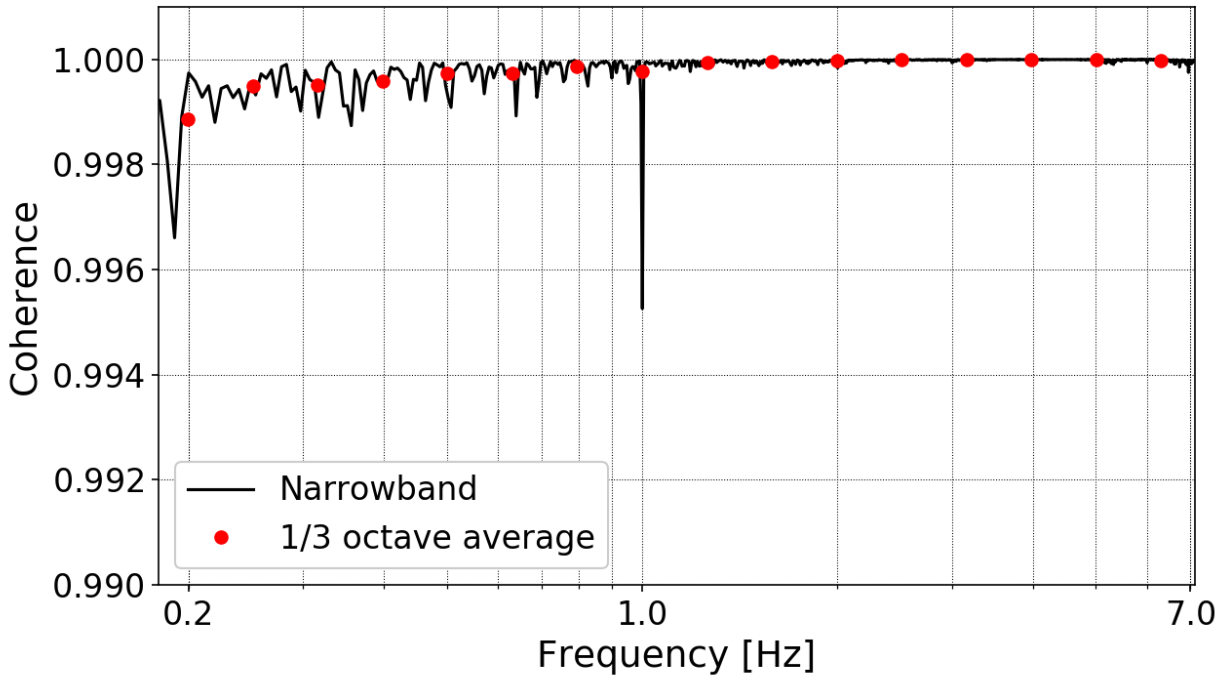

Figure 2.9. Noise coherence results for B&K and MB3d across 0.18 – 7.1 Hz. The solid line represents the coherence between the sensors. The filled circles represent 1/3-octave band averaging.

The noise power spectral density levels in Figure 2.8 and coherence results in Figure 2.9 indicate a coherence above 0.99 between the MB3d and B&K sensors from below 0.2 to beyond 7 Hz (above the upper limit of the MB3d evaluated passband and near where the anti-aliasing filter begins to operate). The normalized random error for the coherence across the passband is (2.4 $\pm$ 8.5)e-05. A downward spike in coherence is visible at 1 Hz. This is likely due to the GPS sampling of the MB3d sensor at 1 pulse-per-second (see Section 2.3.3). The high coherence among the sensors serves to validate the relative response results above the 0.2 Hz 1/3-octave band.

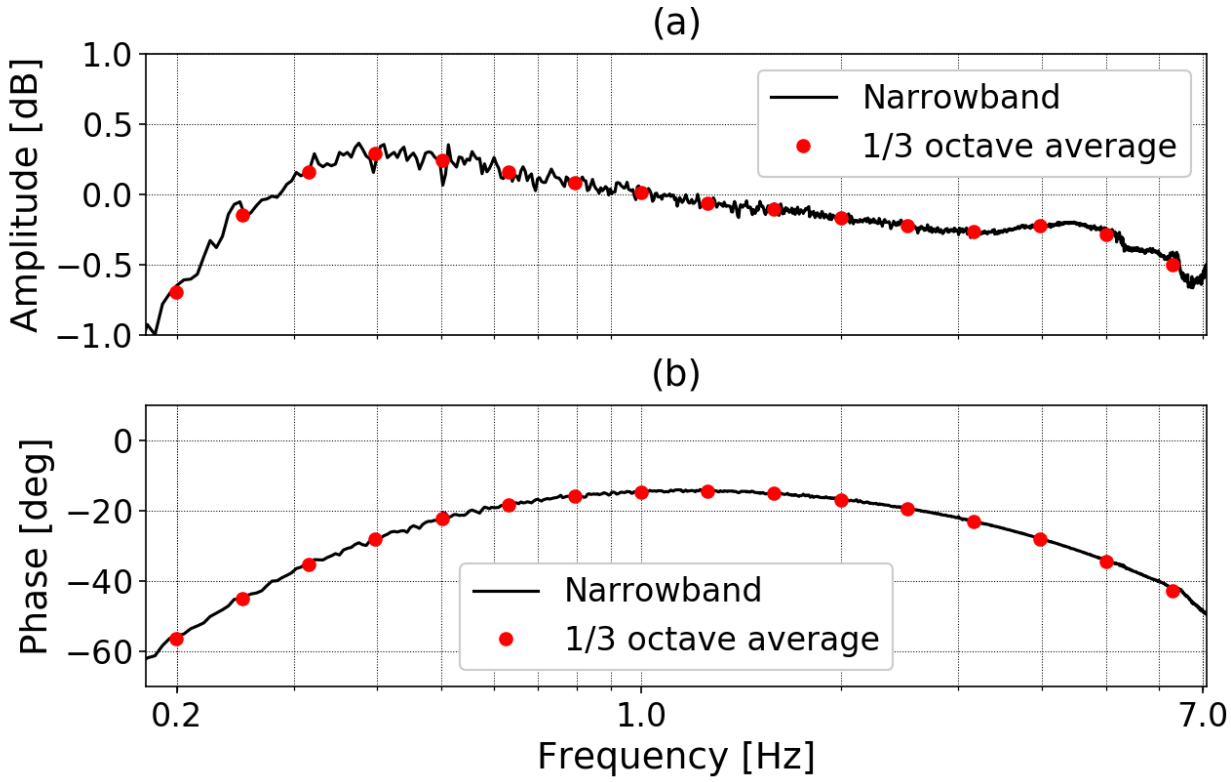

Figure 2.10. Noise response results for B&K relative to MB3d across 0.18 – 7.1 Hz. (a) Relative amplitude between the sensors, computed as the ratio of their response corrected spectra. (b) Relative phase, computed as the angle of the response corrected cross-spectrum. Raw computations are represented by a solid line, while 1/3-octave band averaging is represented by the filled circles.

The relative amplitude 1/3-octave average results between the B&K test sensor and the MB3d in Figure 2.10(a) are flat to within 0.40 dB (4.7%) across the 0.25 – 4.0 Hz 1/3-octave bands (upper limit of the MB3d evaluated passband). Relative phase results in Figure 2.10(b) are -14.6 degrees at 1 Hz. Across the 0.25 – 4.0 Hz passband, the relative phase has an average value of -22.8 $\pm$ 8.9 degrees.

Phase results are highly sensitive to time shifts and resampling. Given that the B&K is not a GPS synchronized system and that its lowest sample rate is 400 times greater than the sample rate of the MB3d, limitations arise in generating proper phase results between the B&K and MB3d. These results suggest that the amplitude response of the B&K sensor is flat above the 0.25 Hz 1/3-octave band, and can be used as a reference in digital calibrations.

2.5 Evaluation of the iPrecision smartphone microphone response across 1- 20 Hz

The test sensor consisted of iPrecision (iMic) smartphone microphone, which had been manufacturer-modified to decrease the lower frequency corner of the response. We obtained a digital sensitivity value in Pa/lsb for the test sensor and evaluated its response across the passband of interest (1 – 20 Hz 1/3-octave bands). The reference was the Brüel & Kjaer Microphone Type 4193 (B&K) sensor considered in Section 2.4. We disconnected both sensors from power and placed them inside a box with approximate dimensions 46 x 33 x 19 cm^3; the box was connected to a manifold, which had one port open. The iMic test sensor was connected to an iPhone 6s running the *RedVox Infrasound app* for iOS; the *app* was set to record at 80 Hz sample rate. The B&K reference sensor recorded at a sample rate of 8,000 Hz. In order to correct for the time between the test and reference sensors, we performed time correlation analysis on 30-second window containing the noise signal described in Section 2.5.2. The iMic data were upsampled to 8,000 Hz in this particular process to obtain better time alignment. We preprocessed B&K data in this section by shifting the waveform by the delay found in the time correction algorithm, then downsampling the record to 80 Hz (with a decimation factor of 100) to match the iMic sample rate, and reversing the polarity to match iMic sensor polarity.

2.5.1 Digital sensitivity measurement

We obtained digital sensitivities in Pa/lsb at 8 Hz and 16 Hz octave center frequencies for the iMic test sensor relative to the B&K reference sensor. The iMic is reported to have a low corner frequency below 3 Hz, which would make octave sinusoid signal measurements at 1, 2, and 4 Hz unreliable. A single digital sensitivity value at 16 Hz was chosen for the test sensor; this was the sinusoidal record with the highest signal-to-noise (i.e., 35 dB) and coherence results.

Table 2.5. Sine fit results with RMS error at 16 Hz for iMic digital sensitivity measurement. The algorithm's signal-to-noise value was 35 dB.

Frequency [Hz]	B&K pressure amplitude [Pa]	iMic digital amplitude [lsb]	iMic digital sensitivity [Pa/lsb]
16	(7.954 $\pm$ 0.100)e-01	(2.863 $\pm$ 0.030)e +06	(2.778 $\pm$ 0.050)e-07

2.5.2 Sensor frequency response

We developed a pole-zero response model for the iMic, described in Table 2.6, sensor and verified its response against the reference B&K sensor. The iMic test sensor is reported to have a flat amplitude response up to 20,000 Hz, with a 3 dB roll off below 3 Hz. We generated a response for the test sensor based on the observed 3 dB roll off frequencies and the measured digital sensitivity at 16 Hz. The iMic frequency response is shown in Figure 2.11. We placed poles at the observed low corner frequencies (each pole was paired to a zero at origin) and corrected the digital gain to obtain the measured digital sensitivity at 16 Hz presented in Table 2.5.

Table 2.6. iMic (SN CQ10003) pole-zero response model based on the digital sensitivity presented in Table 2.5 and the observed 3 dB roll off frequencies at 0.8 Hz, 1.5 Hz and 3.5 Hz.

Gain [lsb/Pa]	Zeros [rad]	Poles [rad]
3.710e+06	0 + 0j	$-2\pi(0.8 + 0j)$
	0 + 0j	$-2\pi(1.5 + 0j)$
	0 + 0j	$-2\pi(3.5 + 0j)$

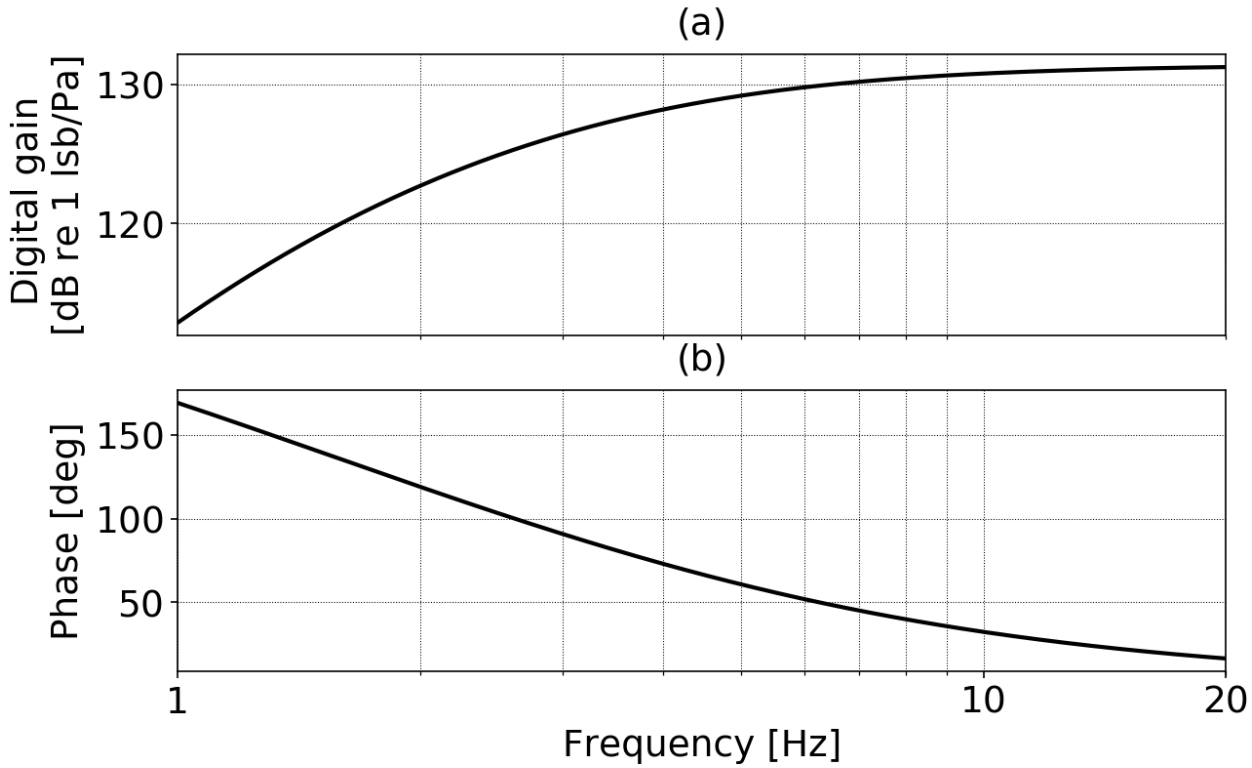

Figure 2.11. Frequency response of the iMic sensor based on pole-zero model presented in Table 2.6. (a) Amplitude response in dB re 1 lsb/Pa. (b) Phase response in degrees.

For this test we generated a 5-minute acoustic noise signal and computed resulting spectra with a Fast Fourier Transform window size of 4,096 samples (~51.2 seconds). Spectral resolution was kept at ~0.02 Hz while performing approximately 24 averages across the record. This allowed for sufficient smoothing of the random spectral variations while reducing errors in phase unwrapping at lower frequencies.

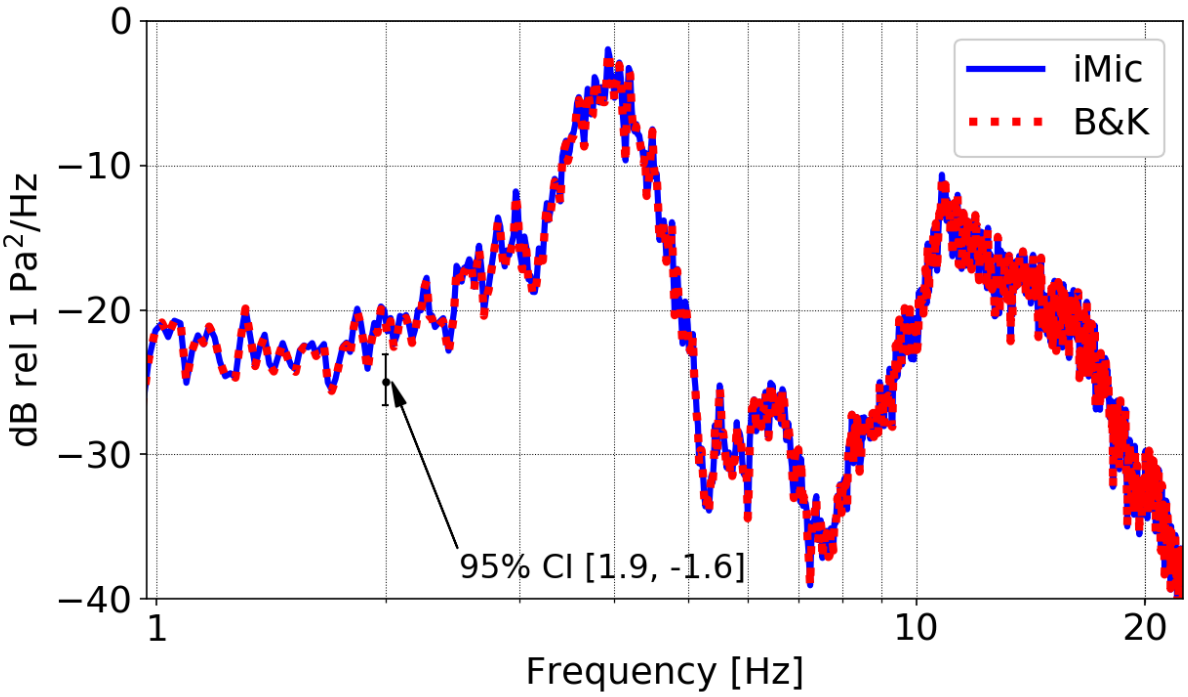

Figure 2.12. Noise power spectral density levels with 95% confidence interval (CI) [1.9, -1.6] dB re 1 Pa^2/Hz for iMic and B&K across 0.97 – 22.4 Hz.

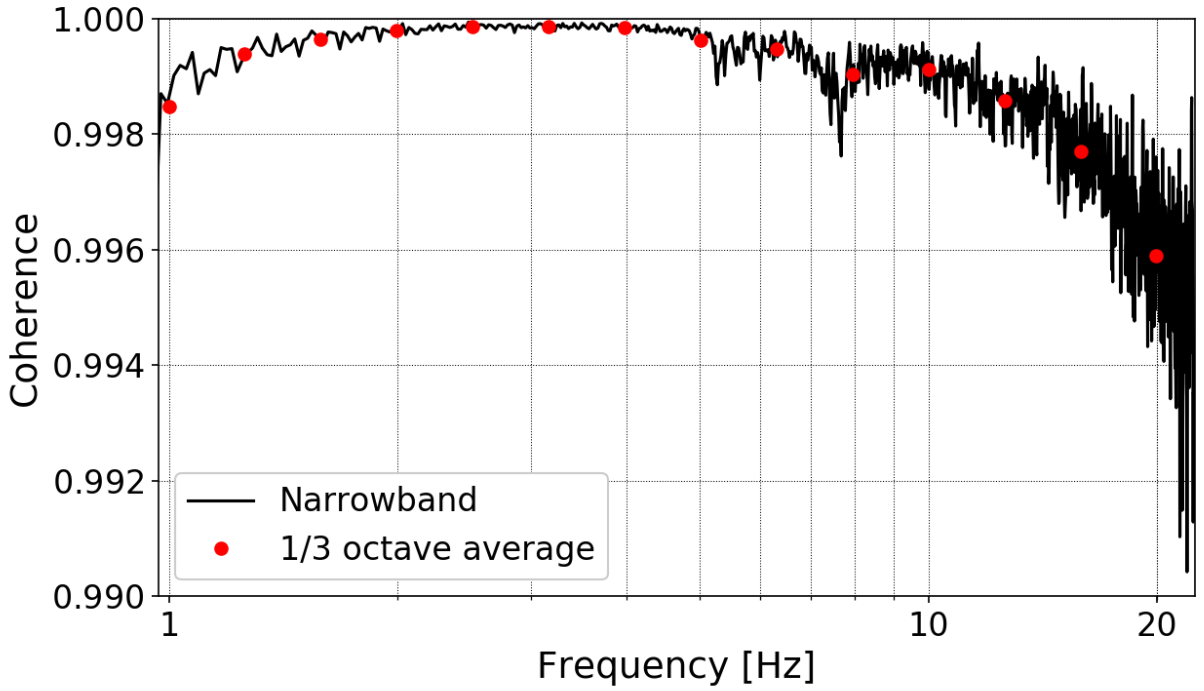

Figure 2.13. Noise coherence results for iMic and B&K across 0.97 – 22.4 Hz. The solid line represents the coherence between the sensors. The filled circles represent 1/3-octave band averaging.

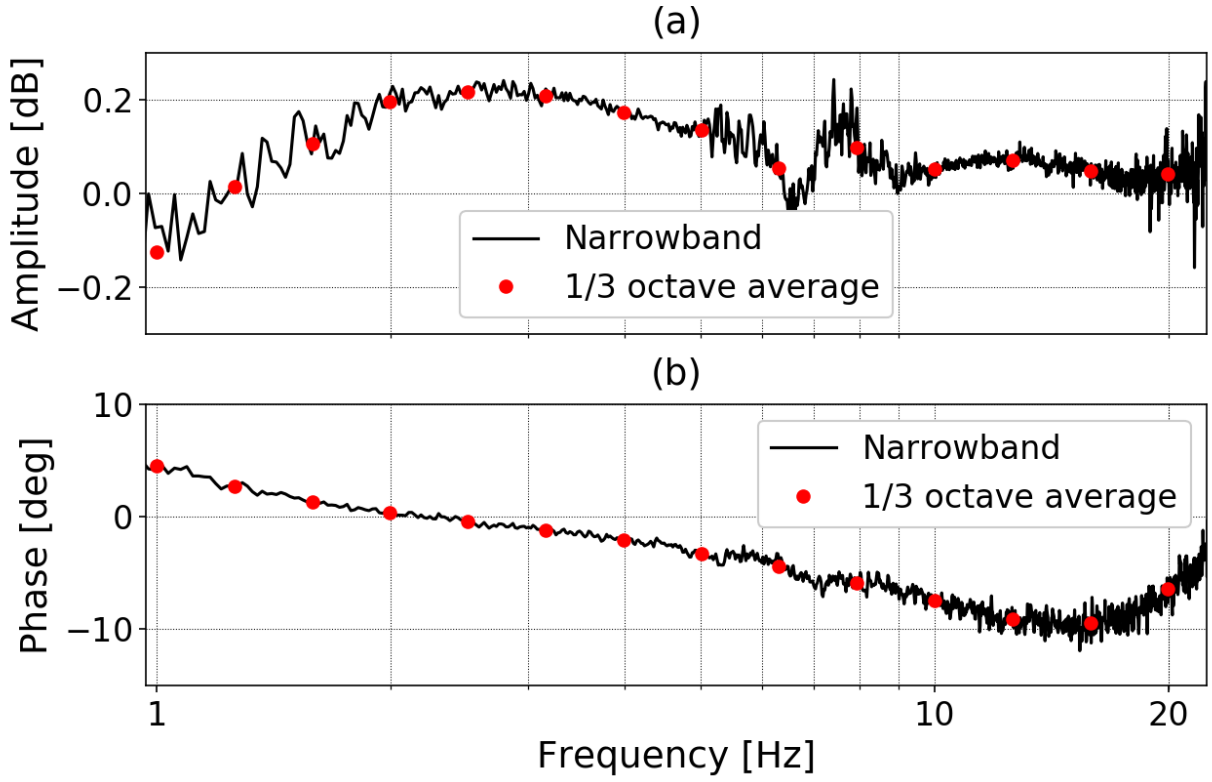

Figure 2.14. Noise response results for iMic relative to B&K across 0.97 – 22.4 Hz. (a) Relative amplitude between the sensors, computed as the ratio of their response corrected spectra. (b) Relative phase, computed as the angle of the response corrected cross-spectrum. Raw computations are represented by a solid line, while 1/3-octave band averaging is represented by the filled circles.

The noise power spectral density levels in Figure 2.12 and coherence results in Figure 2.13 indicate a coherence above 0.99 between the iMic test sensor and the B&K reference sensor across 0.97 – 22.4 Hz, with a normalized random error of (4.0 $\pm$ 3.4)e-04 across the passband. Relative amplitude 1/3-octave average results shown in Figure 2.14(a) are flat to within 0.22 dB (2.6 %) from the 1 Hz 1/3-octave pass band to beyond 20 Hz. Across the same passband, the relative phase of the sensors in Figure 2.14(b) has an average value of -2.9 $\pm$ 4.2 degrees. Though the relative phase is within 10 degrees across the passband, time shifts and downsampling factors are limitations in a proper phase fitting of the sensors. The iMic sensor's amplitude response is consistent with its parametric response model in a non-isolated environment across 1 – 20 Hz.

2.6 Conclusions

We have developed and characterized parametric response models for two next-generation digital acoustic sensors; we verified these responses against traceable, well-established analog sensors connected to external digitizers across the infrasound (i.e. 0.01 – 20 Hz) range in a non-isolated environment. We first evaluated the MB3 digital (MB3d) infrasound sensor against its MB2000 analog sensor predecessor, which was connected to a conventional external Reftek digitizer well known for its use in field experiments. We found the MB3d digital sensitivity at 1 Hz to be 5.6% from its nominal relative to the MB2000 nominal, and developed a pole-zero response model based on the measured digital sensitivity and the manufacturer-reported corner frequencies. Broadband measurements of a noise source indicated that the MB3d is consistent with its estimated response model across 0.01 - 4 Hz and meets the International Monitoring System requirements in a non-isolated environment. Self-noise measurements acquired over a three-hour period showed that the MB3d is consistent with its CEA self-noise model from 0.15 Hz to 4 Hz in a non-isolated environment. We postulate that increased self-noise levels below 0.15 Hz are due to atmospheric background noise feeding into the sensor in a non-isolated environment, while higher levels above 4 Hz are due to seismic vibrations. This suggests that the performance of the MB3d, as per its manufacturer specifications, could be affected by external factors at frequencies outside the 0.15 – 4 Hz pass band in non-isolated environments.

We proceeded to develop a response model for an analog Brüel & Kjaer (B&K) Microphone Type 4193 and evaluated it against the calibrated MB3d. We obtained the digital sensitivities at 1, 2, and 4 Hz for the B&K relative to the MB3d (shown in Table 2.3). The results showed that the B&K frequency response is coherent with the MB3d and flat down to 0.40 dB (4.7%) across the sensors' common passband (0.25 – 4 Hz). We subsequently calibrated an iPrecision (iMic) digital microphone sensor

connected to an iPhone 6s against the chosen B&K reference. Sinusoidal tone measurements provided a digital sensitivity value in Pa/lsb for the iMic sensor at 16 Hz, shown in Table 2.5. We developed a response model for the iMic sensor based on the measured digital sensitivity and corner frequencies. Measurements from a broadband noise source showed that the iMic amplitude response is coherent with the B&K reference and flat to within 0.22 dB (2.6 %) across 1 – 20 Hz.

Two factors limit our ability to perform a proper fit of the phase portion of the complex responses for the B&K and iMic sensors. First, the B&K and iMic sensors are not Global Positioning System (GPS) synced data acquisition systems, and thus have an inherent absolute timing error. Second, the process of decimation of the B&K data removed a significant amount of original samples. Phase responses are highly sensitive to time shifts and resampling, both which were present in the work described in this article.

Signal processing results (i.e., high coherence and signal-to-noise) demonstrate the application of a portable rotary subwoofer as a controllable infrasound source during calibration experiments. We showed that digital calibrations performed in a non-isolated calibration room can provide useful and reproducible results. By overlapping the responses of the MB3d microbarometer (i.e. 0.01 - 4 Hz) and the iPrecision microphone (i.e. 1 – 20 Hz) we can potentially benchmark next-generation digital sensor performance across the 0.01 – 20 Hz (i.e., infrasound) pass band. Upon further validation of stability and repeatability, these parametric responses could be used as references in future pressure measurements and digital acoustic sensor calibrations.

Acknowledgements

This work was supported by the Consortium for Verification Technology under Department of Energy National Nuclear Security Administration Award DE-NA0002534.

CHAPTER 3. A METHOD FOR ESTIMATING THE AMPLITUDE RESPONSE OF SMARTPHONE BUILT-IN MICROPHONE SENSORS BELOW 4 kHz

In review as: Asmar, K., Garces, M., and Williams, B. “A method for estimating the amplitude response of smartphone built-in microphone sensors below 4 kHz” *J. Acoust. Am.*

ABSTRACT

A method for estimating the amplitude response of built-in smartphone microphone sensors is presented. The method is intended to be accessible to the general public, and comparison calibration measurements are performed in a non-isolated environment using conventional consumer products. A double reference sensor scheme is set up, consisting of a MB3 digital microbarometer (reference over the 0.5 – 2 Hz octave bands) and the iPrecisionMic smartphone microphone (reference above the 2 Hz octave band). The amplitude response of the iPrecisionMic sensor is first evaluated over the 1 – 2000 Hz octave bands. The amplitude response of three Samsung Galaxy S8 built-in smartphone microphone sensors is then measured over the 0.5 – 2000 Hz octave bands. The *Redvox Infrasound Recorder* application (app) for Android is used to measure acoustic signals with the built-in smartphone microphone sensors. Amplitude response models in terms of digital gain are estimated for the test sensors based on the results. Last, self-noise levels for the iPrecisionMic and Samsung Galaxy S8 microphones are estimated and compared to Infrasound Station ambient noise models. Results show an experimental capability for estimating the amplitude response of built-in smartphone microphone sensors in a non-isolated environment with conventional consumer products.

3.1. Introduction

Smartphones currently constitute the fastest growing segment of the increasing commercial demand for personal mobile devices. Since the appearance of the iPhone in 2007, iOS and Android operated smartphones have evolved into high-performance multi-processor computers with built-in sensors such as microphones, barometers, accelerometers, magnetometers, gyroscopes, etc. Of the 1.46 billion devices shipped worldwide by smartphone companies in 2017, the majority run on Apple iOS and Google Android operating systems (IDC, 2018).

The growing prevalence of smartphones as consumer devices has fueled their integration into the scientific community as sensing systems, offering scientists the opportunity to acquire quality data expeditiously and at low cost. In the field of sound measurement, Kardous and Shaw (2014) examined several smartphone sound applications (apps) and found some of them accurate and reliable in occupational noise measurements. In a follow-up study (Kardous and Shaw, 2016), the accuracy of these apps when used with two different external calibrated microphones was examined. The authors showed that accuracy and precision of smartphone measurements is significantly enhanced with the use of external microphones. In seismology, the embedded accelerometers and GPS receivers of smartphones have been considered in earthquake monitoring studies. Minson *et al.* (2015) confirmed the capability of smartphones in detecting displacements from moderate and larger earthquakes, and proposed the use of crowdsourcing with smartphone data to achieve Earthquake Early Warning Systems. Kong *et al.* (2016) described a smartphone seismic system for the collection and analysis of earthquake data, as well as the development of an early warning algorithm.

Though the field of smartphone detection in acoustics is recent, numerous software applications, or apps, making use of their built-in microphones are already available. These microphones are designed for the recording and transmission of speech, which requires an enhanced response across the 350 – 4800 Hz passband (American National Standards Institute, Inc. 1997). The application of built-in smartphone microphones in infrasound recordings of rocket launches and high surf was presented in Asmar *et al.* (2016a) and Asmar *et al.* (2016b), respectively. Because of their growing presence in acoustic measurements, efficient and accurate calibration methods are necessary to benchmark the performance of these smartphone sensors. Wagner and Fick (2017) described the pressure reciprocity calibration of micro-electro-mechanical-systems (MEMS) microphones, commonly used in consumer devices such as smartphones (Ko, 2007), across 100 – 10,000 Hz. Their measurements showed the MEMS microphone responses to be within manufacturer specifications. Brown and Evans (2011) measured 1/3-octave sound pressure levels and reverberation time with iPhone apps and compared them to a Brüel & Kjaer (B&K) Hand Held Sound Level Meter Type 2250. Their study found that iPhone and B&K sound pressure levels were typically within 5 dB of each other, and that iPhone internal microphones had a limited dynamic and frequency range; namely, the iPhone internal microphone had a poor response below 200 Hz due to high noise floor. Further literature describing the frequency amplitude response of smartphone microphones is limited.

In this work, we develop a method for estimating the frequency amplitude response of built-in smartphone microphone sensors over the 0.5 - 2000 Hz octave bands. We use comparison calibration techniques to measure the response of the sensors across the passband of interest. A double reference sensor scheme (Marcillo *et al.,* 2012) is set up to measure frequency amplitude responses below 4 kHz. The reference sensor for measurements over the 0.5 – 2 Hz octave bands is the MB3 digital microbarometer (MB3d), an infrasound sensor developed by the Commissariat à l'Énergie Atomique (CEA) to meet the International Monitoring System (IMS) of the Comprehensive Test Ban Treaty Organization (CTBTO) requirements (Seismowave, 2015). Asmar *et al.* (2018) performed a digital calibration of this sensor; the study found the measured sensitivity of the MB3d to be within 5.6% of the nominal value and its frequency response to be flat (within 3 dB) across 0.01 – 4 Hz. For measurements above the 2 Hz octave band, the reference is the iPrecision smartphone microphone (iMic) (Audio Control, 2018), a factory calibrated iOS condenser microphone with an embedded preamplifier and 24-bit analog-to-digital converter (ADC). When connected to an iPhone or iPad, it is able to bypass the analog electronic stages with a digital audio link and override the internal microphone of the mobile device. Asmar *et al.* (2018) performed a digital calibration of this sensor and estimated a response model across 1 – 20 Hz to within 3% deviation. In this study, we expand the frequency amplitude response measurement of the iMic up to 2000 Hz, using a Brüel & Kjaer (B&K) Microphone Type 4193 as reference. B&K microphones and sound level meters are known for their long-established stability and are commonly used as references in calibration procedures by the acoustics community (Brown and Evans, 2011; Larsonner *et al.*, 2014; Ollivier *et al.*, 2014; Vanwynsberghe *et al.*, 2015).

The smartphone test sensors evaluated in this article consist of three Samsung Galaxy S8 (Model SM-G950U1) smartphones running the *RedVox Infrasound* app for Android (Redvox, 2018). The app displays the acoustic pressure recorded with the internal or external microphone of the smartphone as it streams the sound files anonymously to a cloud server for analysis. The app (version 2.3.15) contains options to sample acoustic data with the sensor microphone at 80, 800, and 8000 samples/sec. In this work, we evaluate the frequency amplitude response of the smartphone microphones at each sample rate for comparison.

In order for an acoustic signal to be measured by the app, the original pressure signal must first pass through the transducer (i.e., microphone), transforming physical pressure into an analog electrical signal measured in volts. The proportion of the original pressure units to the final electrical units is constrained by the transducer sensitivity, usually measured in V/Pa. The electrical signal then passes through the system's electronic interface, where the ADC digitizes the signal and converts the electrical units to digital units. The *least significant bit* (lsb) is defined as the smallest step that can be represented by the digital output word of the ADC. The proportionality of the electrical to digital units is constrained by the system's ADC resolution, and is measured in V/lsb. Once the signal is digitized, the operating system (OS) of the smartphone takes over, at times applying filters to the signal for sample rate conversion (Faber, 2017). The final signal output of the app is a digital binary signal proportional to the original

pressure signal. This proportionality is determined by the system's overall gain, referred to in this work as the *digital gain*, and is measured in lsb/Pa.

The *Redvox* app uses 24-bit audio, which allows for a number of discrete levels 256 times greater than 16-bit audio processors. This permits a higher precision of the system's quantization process (i.e., when the signal is mapped into discrete levels represented by a sequence of bits), a wider dynamic range, and a lower quantization error (Oppenheim and Schafer, 1989b). A 1-bit increase is equal to double the accuracy of a single measurement, or a dynamic range increase of the sensing system by approximately 6 dB (Sleeman *et al.,* 2006).

The main purpose of this article is to present an experimental method for estimating the responses of built-in smartphone acoustic sensors. Section II describes the experimental and processing methods applied during the digital calibration tests. Section III describes the evaluation of the iPrecision microphone (connected to an iPhone 6s (Model iPhone 8,1) and sampling at 8000 samples/sec) frequency amplitude response over the 1 – 2000 Hz octave bands. This sensor is then chosen as a reference above 2 Hz. In Section IV we estimate the frequency amplitude response of the Samsung Galaxy S8 smartphone microphones over the 0.5 – 2000 Hz octave bands. We measure the self-noise of the iPrecision microphone and the three Samsung Galaxy S8 smartphone microphones in Section V. We summarize our observations and comment on the implications of our results in Section VI.

3.2. Methods

Amplitude response measurements for the sensors described in this work were performed in a ~10.7 x 7.3x 3.0 m^3 non-isolated calibration room. Table 3.1 shows a summary of the sensor names and descriptions in relation to their respective octave band measurements. External noise factors such as wind, vibrations and anthropogenic noise were present in the measurements. A Tektronix RM 3100 signal generator was used to generate sinusoidal frequency tones. A Thigpen Rotary Woofer Model 17 (TRW-17) (Eminent Technologies, 2018; Park *et al.*, 2009a; Park and Robertson, 2009b) was used as the sound projector for tones lower than 20 Hz. The TRW-17 is a fan driven by an electric motor that rotates at steady revolutions-per-minute (RPM). The fan generates a sound pressure wave that propagates at a frequency determined by an electric input signal. The input signal is fed into the system's audio amplifier, which then drives an electromagnetic coil assembly into longitudinal motion. The motion of the coil is converted into rotational motion of the fan's blades, which pitch at a frequency equal to that of the input signal (Park *et al.,* 2009a). In this study, the TRW-17 was configured to radiate into the calibration room, while a room with approximate dimensions 8.8 x 6.6 x 3.0 m^3 served as the back volume. A Mackie Active Subwoofer (Model SWA1801z) was used as sound projector for tones from 20 Hz to 250 Hz. A Mackie Speaker (Model S215) was used as sound projector for tones higher than 250 Hz.

Digital gain levels for the smartphone test sensors at each frequency tone were computed with three-parameter sine-fit analysis (Merchant and Hart, 2011). Single or third octave center frequency tones were generated using the signal generator with input parameters 1 Vpp amplitude, 0 phase, and 0 offset.

For computational efficiency, we downsampled smartphone sensor data records to 20 samples/sec for 0.5 – 4 Hz tones. Similarly, data records for tones from 8 Hz to 20 Hz were downsampled to 80 samples/sec, unless the sample rate was originally 80 samples/sec. Data records for tones from 20 Hz to 300 Hz were downsampled to 800 Hz, unless the sample rate was originally 800 samples/sec. A band pass filter was applied to the tone data with corner frequencies at $G^{-1/2N}f_0$ and $G^{1/2N}f_0$, where $G = 10^{0.3}$, N is the octave order, and f_0 is the center frequency (i.e., tone) of the octave band (Garces, 2013). We use octave (N=1) and 1/3-octave (N=3) bands. The bandpassed digital data records were then sliced into consecutive segments of user-specified cycles. The sine-fit algorithm was performed on the segments, selecting results with the highest signal-to-noise values. In this paper, we refer to the Pa/lsb value as the *digital sensitivity*, and the lsb/Pa value for the pole-zero model as *digital gain.* The sine-fit amplitude results for the reference sensor were then multiplied by the sensor's digital sensitivity [Pa/lsb] in order to obtain pressure units. The digital gain [lsb/Pa] of the test sensor was computed as the ratio of the test sensor digital amplitude to pressure reference amplitude. Uncertainty levels for digital gain and sensitivity values were computed using error propagation techniques, where the uncertainty of the fit is computed as described in Merchant and Hart, 2011.

Table 3.1. Summary of sensor names and abbreviations in relation to the measurements over the octave band frequencies.

Sensor name	Sensor description	Measurement description
MB3d	MB3 digital microbarometer	Reference for S8 sensors over the 0.5 – 2 Hz octave bands
B&K	Brüel & Kjaer Microphone Type 4193 (B&K), attached to preamplifier ZC-0032 and Hand Held Analyzer Type 2250	Reference for iMic sensor over the 1 – 2000 Hz octave bands
iMic	the iPrecision microphone (iMic) connected to an iPhone 6s (Model iPhone 8,1)	Reference for S8 sensors over the 4 – 2000 Hz octave bands
S8	Samsung Galaxy S8 (Model SM-G950U1) smartphone built-in microphone	Response measured over the 0.5 – 2000 Hz octave bands

3.3 Amplitude response of the iMic

The response of the iMic was evaluated with the *RedVox* app for iOS (version 3.1.11), recording audio data at a sample rate of 8000 samples/sec. The reference sensor was the B&K, which recorded at

a sample rate of 8000 samples/sec. We first obtained the digital gain value for the iMic sensing system at 1 kHz using the Brüel & Kjaer Acoustic Calibrator Type 4231 (Brüel & Kjaer, 2014). The calibrator generates a 1 kHz tone with sound pressure level 94 dB ± 0.05 dB (0.58% error), which corresponds to a pressure value of one pascal. We recorded more than 100 cycles of each tone with the sensor, and performed sine fit analysis on the data to find the digital gain. The iMic pole-zero model proposed by Asmar *et al.* (2018) indicates a flat response above 20 Hz, with -3 dB roll offs at 0.8, 1.5, and 3.5 Hz, as shown in Table 3.2.

Table 3.2. Pole-zero model for the iMic. The digital gain was measured with Brüel & Kjaer Acoustic Calibrator Type 4231.

Digital gain [lsb/Pa]	Zeros [rad]	Poles [rad]
(1.013 ± 0.002)e+06	0 + 0j 0 + 0j 0 + 0j	-2π(3.5 + 0j) -2π(1.5 + 0j) -2π(0.8 + 0j)

The complex frequency response $H(e^{j\omega})$ of the iMic can be computed with Eq. (1),

$$H(e^{j\omega}) = k\frac{\prod_{i=1}^{i=N_{zeros}}(j\omega - z_i)}{\prod_{i=1}^{i=N_{poles}}(j\omega - p_i)}. \quad (3.1),$$

where ω is the angular frequency in radians, k is the gain factor in lsb/Pa, p_i represents the poles, z_i denotes the zeros (Merchant and Hart, 2011). The frequency *magnitude response* $\left|H(e^{j\omega})\right|$ in lsb/Pa can then be obtained as the modulus of Eq. (1), also known as the *gain* of the system (Oppenheim and Schafer, 1989a). The locations of the poles, when paired to a zero at origin, represent the corner frequencies with 3 dB decrease in spectral levels. The inverse of the discrete magnitude values correspond to the sensor's digital sensitivities in Pa/lsb at the angular frequency ω, or $2\pi f$, where f is the discrete frequency in Hz.

In order to verify the iMic response, we generated tones from 1 to 2,000 Hz in octave steps and measured the sensor's digital gain relative to the B&K. For optimization of signal-to-noise, we reconfigured the sensors according to the tone frequency. For 1 – 16 Hz tones and 125 – 500 Hz, the sensors were placed on a table approximately 5 meters from the rotary subwoofer and 1 inch (2.54 cm) apart from each other. For 32 Hz and 63 Hz tones, the sensors were placed inside a box with approximate dimensions 46 x 33 x 19 cm^3 on the same table. The box was closed and connected to a manifold, which had one port open. For 1 kHz and 2 kHz tones, the sensors were placed at precisely the same location (~10 inches or ~25 cm directly in front of the Mackie Speaker). Digital gain values for the iMic were obtained at each discrete frequency relative to the B&K by performing sine fit analysis on the data records.

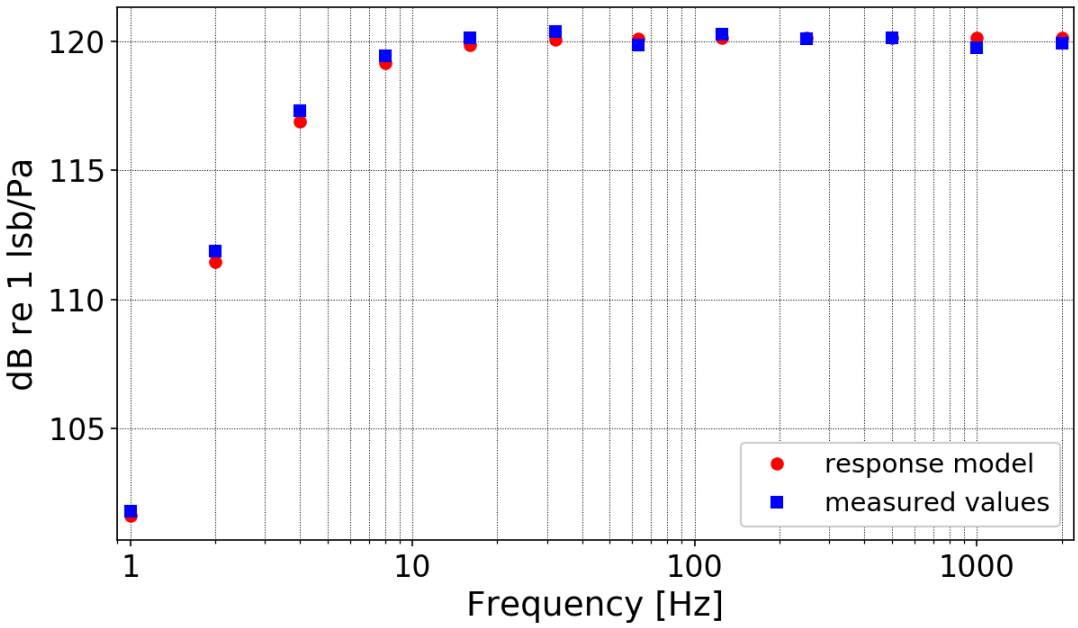

Figure 3.1. (Color online) Measured (filled squares) amplitude response for the iMic compared to the response model values (filled circles), which were computed with the pole-zero model shown in Table 3.2. The measured digital gain values were obtained by performing sine fit analysis on the sinusoidal tone data records, using the B&K as reference.

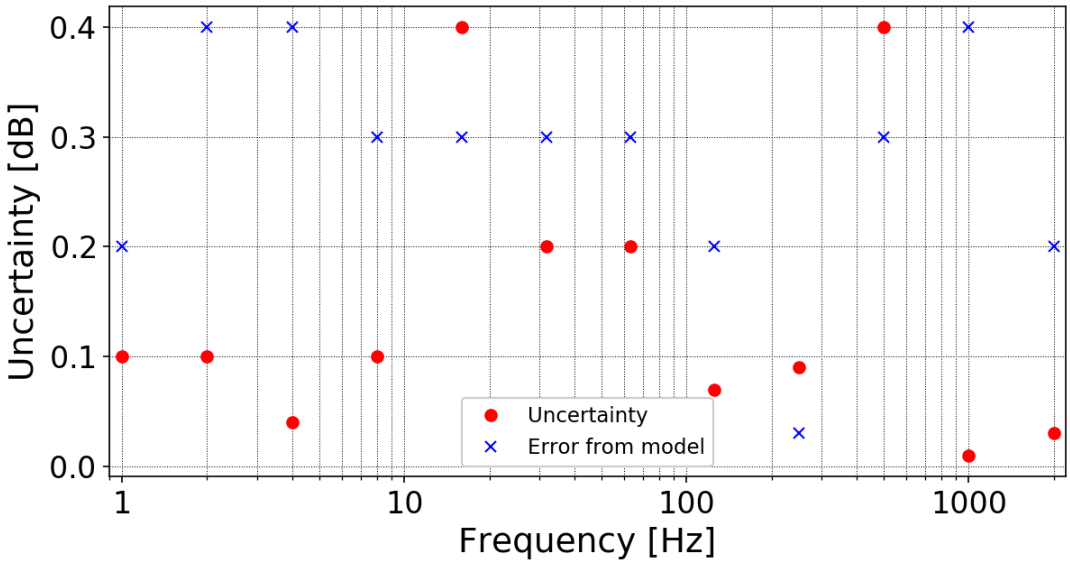

Figure 3.2. (Color online) Uncertainty of measured digital gain levels for the iMic. Uncertainty levels of the measurements are shown as filled circles, and errors of measured values from the response model in decibel units are shown as crosses.

Measured digital gain levels shown Figure 3.1 and their deviations from the model in Figure 3.2 show that the iMic is consistent with its parametric response model (presented in Table 3.2) down to 0.4 dB (4.7%). Similarly, uncertainty levels shown in Figure 3.2 indicate that the accuracy of the measurement procedure is within 0.4 dB (4.7%). The results show that by obtaining an accurate digital sensitivity level for the sensor at 1 kHz, the amplitude response can be computed within an error smaller than 5%.

3.4 Amplitude response of the S8

The amplitude response of three S8 microphones was estimated in a non-isolated calibration room. The smartphones were running the *RedVox* app (version 2.3.15) for Android, and the responses were evaluated with the app sampling at 80, 800, and 8000 samples/sec. We developed an amplitude response model for the smartphones based on the observed -3 dB low corner frequencies and digital gain levels.

For measurements with the MB3d, the smartphone test sensor was placed inside a box with approximate dimensions 46 x 33 x19 cm^3. The smartphone stood vertically on a conventional phone holder. The box was closed and connected to a manifold along with the MB3d, which sampled at 20 samples/sec. The unused ports of the manifold and MB3d were capped. The MB3d and manifold box were placed approximately 5 meters from the TRW-17 rotary subwoofer. For the rest of the measurements, the reference iMic was used. For 4 - 100 Hz measurements, the smartphone test sensor was placed on the phone holder next to the iMic inside the box. The box was then connected to the manifold, which had the rest of its ports capped (see Figure 3.3).

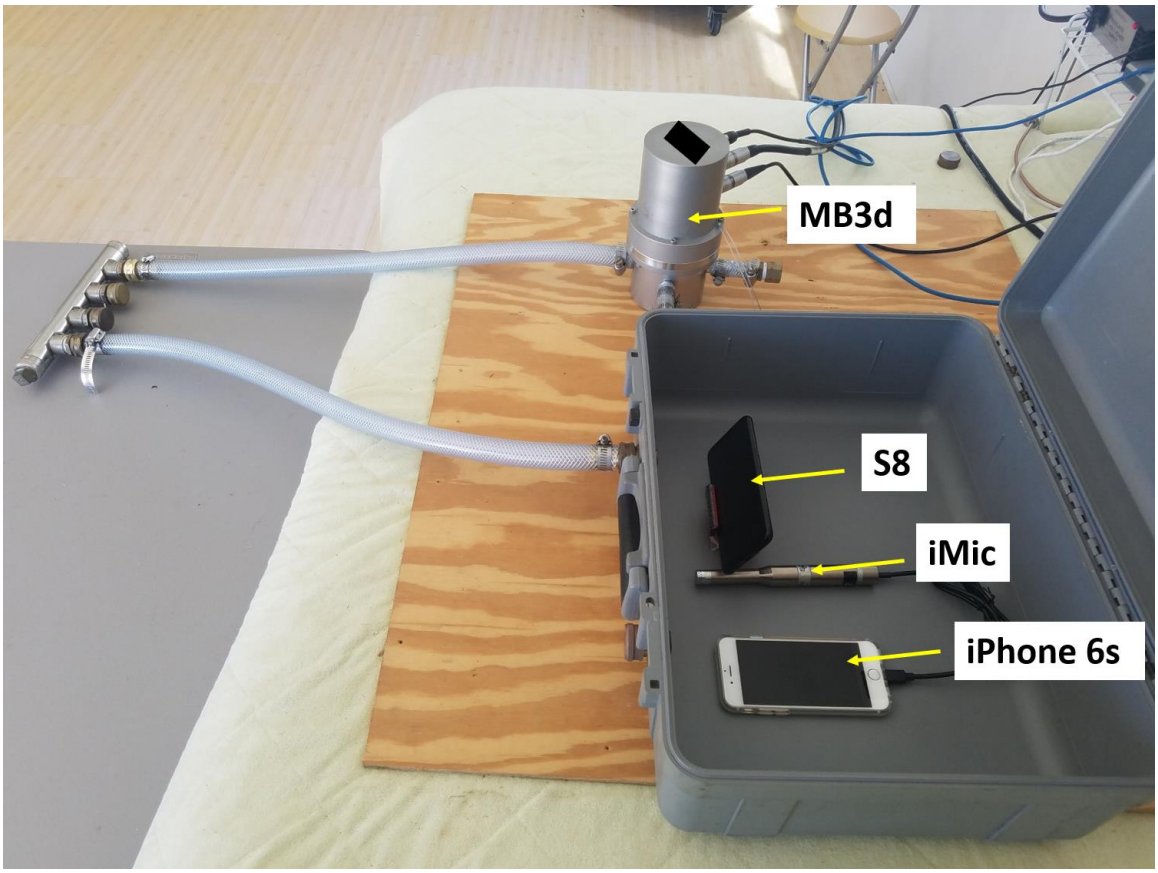

Figure 3.3. (Color online) Example of setup for measurements below 100 Hz. The iMic (connected to an iPhone 6s) is placed next to the S8, which is placed on a phone holder. Both sensors are placed inside a box with dimensions 46 x 33 x19 cm^3, which is connected to a manifold. The MB3d is connected to the same manifold, and both the box and the MB3d have their remaining ports capped. The box's lid was closed for all measurements.

Measurements above 100 Hz and below 300 Hz were performed with the smartphone test sensor on the phone holder next to the iMic, both placed on a table approximately 2 meters from the Mackie Subwoofer. Measurements above 300 Hz were performed with the smartphone test sensor on the phone holder next to the iMic, both placed directly in front of the Mackie Speaker. For tones from 300 Hz to 2 kHz, the distance between the sensors and projector was approximately 0.3 meters, and for tones above 2 kHz the distance was approximately 0.8 meters.

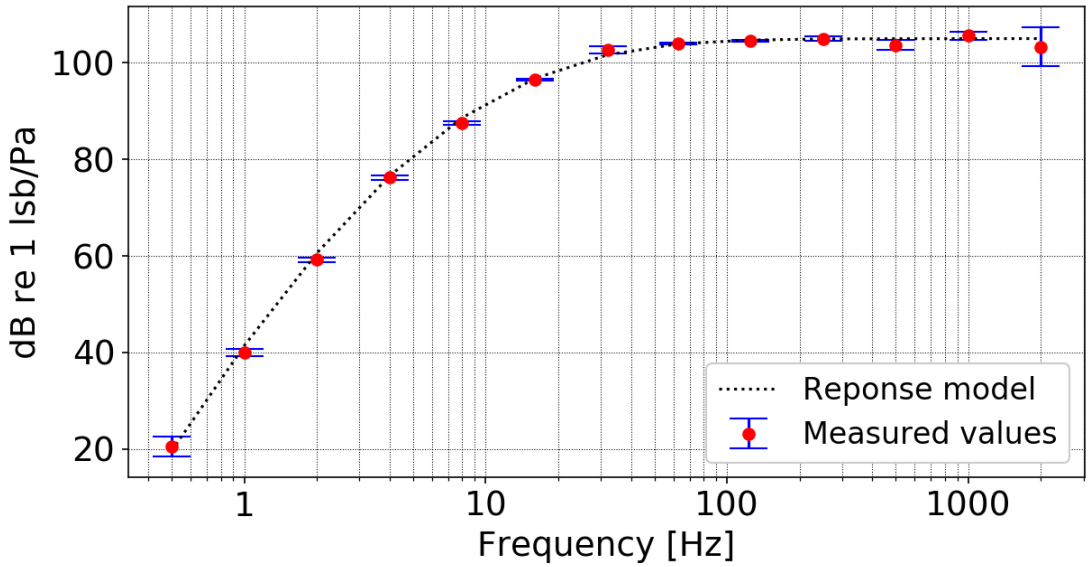

Figure 3.4. (Color online) Measured frequency amplitude response for three S8 sensors. Digital sensitivity values for each sensor were obtained with sample rates of 80, 800 and 8000 samples/sec. Measured values are shown as the mean and standard deviation of all nine measurements. An amplitude response model, shown as a dotted line, was developed based on the observed responses. The model indicates a 105 dB re 1 lsb/Pa digital gain with -3 dB low corner frequencies at 32, 8, 4, and 1 Hz.

Figure 3.4 shows digital gain mean values for three S8 sensors. Data were acquired for each sensor sampling at 80, 800, and 8000 samples/sec. The measured response of the first sensor varied with sample rate within $\pm$1.2 dB (14.8%), with a mean variation of -0.1 $\pm$ 0.3 dB (1.0 $\pm$ 4.0 %). The second sensor showed a response variation with sample rate within $\pm$1.1 dB (13.5%), with a mean variation of -0.1 $\pm$ 0.3 dB (1.0 $\pm$ 4.0 %). The response of the third sensor varied within $\pm$1.6 dB (20.2%) with changing sample rates, with a mean variation of -0.2 $\pm$ 0.5 dB (2 $\pm$ 6 %).

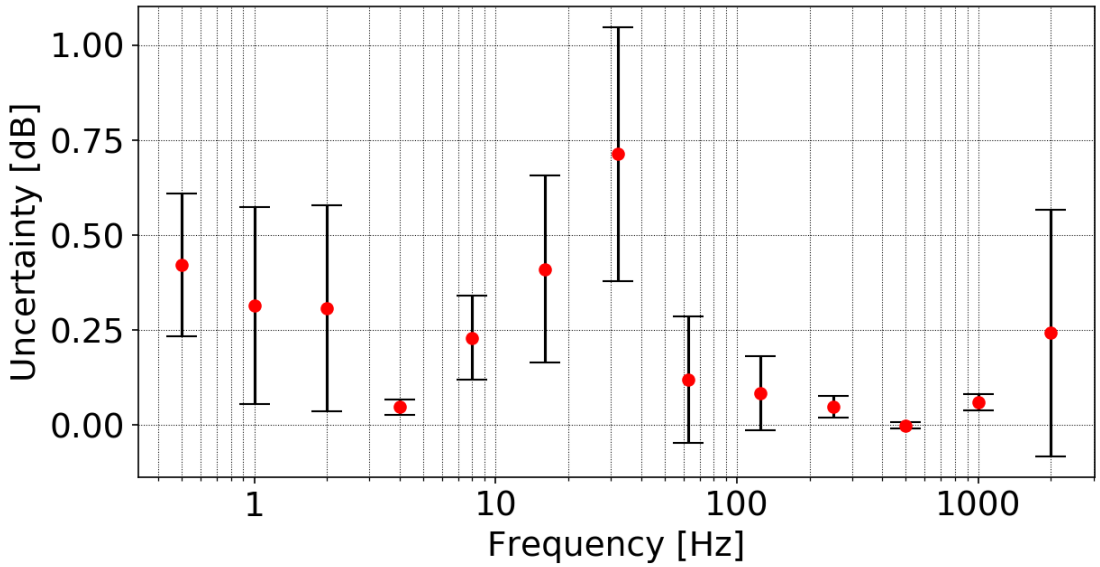

Figure 3.5. (Color online) Average and standard deviation of uncertainty levels for digital gain measurements for three S8 sensors. Measurements were obtained at sample rates of 80, 800, and 8000 samples/sec.

Table 3.3. Comparison of measured digital gain levels with the estimated response model of the S8 sensor. The digital gain levels were measured with three devices, each sampling at 80, 800, and 8000 samples/sec. The mean levels are compared to the estimated response model, which consists of a 105 dB re 1 lsb/Pa digital gain with -3 dB low corner frequencies at 32, 8, 4, and 1 Hz.

Frequency [Hz]	**Mean of digital gain [dB re 1 lsb/Pa]**	**Digital gain from response model [dB re 1 lsb/Pa]**	**Model estimate minus the mean [dB]**
0.5	20.57 ± 2.00	19.66	-0.91
1	40.02 ± 0.80	41.45	1.43
2	59.20 ± 0.40	60.64	1.44
4	76.20 ± 0.40	76.61	0.41
8	87.50 ± 0.40	88.65	1.15
16	96.44 ± 0.20	96.76	0.32
32	102.7 ± 0.7	101.7	-1.00
63	104.0 ± 0.2	103.9	-0.10
125	104.5 ± 0.2	104.7	0.20
250	105.0 ± 0.4	104.9	-0.10
500	103.7 ± 1.0	105.0	1.30
1000	105.6 ± 0.9	105.0	-0.60

2000	103.3 ± 4.0	105.0	1.70

Uncertainty levels in Figure 3.5 suggest that the measurement procedure is accurate within 1 dB (12%). Table 3.3 shows the mean of the measured gain levels of the three smartphones at the different app sample rates. The mean gain levels deviate from the proposed response model within an average of 0.7 ± 0.6 dB (8 ± 7 %).

In order to further verify the estimated amplitude response model for the S8 sensors, digital gain measurements were made at 1/3-octave center frequencies for the first sensor. The measured response compared to the response model is shown in Figure 3.6. Measured values at all 1/3-octave bands were within 2.7 dB (36%) of the estimated response model. The average deviation between 1/3-octave digital gain measurements and response model values was -0.8 ± 1.0 dB (9.6 ± 12.2 %).

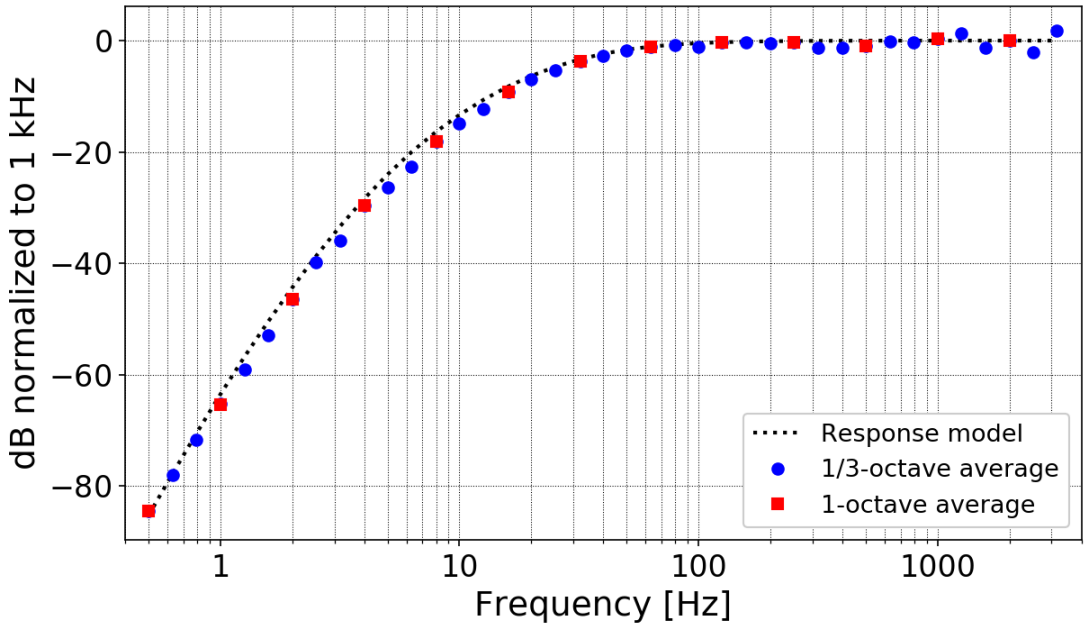

Figure 3.6. (Color online) Measured frequency amplitude response for one S8 sensor over the 0.5 – 3162 Hz 1/3-octave bands, normalized to 1 kHz. The estimated response model, shown as a dotted line, corresponds to a digital gain of 105 dB re 1 lsb/Pa and -3 dB low corner frequencies at 32, 8, 4, and 1 Hz. This corresponds to a digital sensitivity of 5.623e-06 Pa/lsb at 1 kHz. 1/3-octave measured digital gain levels are shown as filled circles, and octave averages are shown as filled squares.

3.5 Self-noise measurements

We measured the self-noise of the iMic and the three S8 sensors, considered in Sections III and IV, respectively. The smartphones were running the *RedVox* app with a sample rate of 8000 samples/sec. The sensors were placed simultaneously inside a portable sealed chamber and left recording for 10 minutes. This record length permits a total of 300 cycles at the lowest frequency of interest of 0.5 Hz. The portable sealed chamber is a cylinder ~26 cm long with a ~15 cm diameter with ~2.5 cm wide hatches on both ends providing a seal when closed. This chamber is commonly used for underwater sensor deployments.

Frequency analysis was performed using Welch's method (Welch, 1967). The digital time series were first divided into 75% overlapping segments of 32,768 samples (~4 second duration for a spectral resolution of ~0.2 Hz). After removing the mean for each segment and applying a *Hann* window of equal duration, the power (in Pa^2) or power density (in Pa^2/Hz) spectrum was computed by taking the square of the Fourier transform of the segments and removing the response of the sensor (Asmar *et al.*, 2018). The power and power density spectra were corrected for the windowing operation by multiplying the segments by a factor of $1/\sum_{i=1}^{M} w^2$ and $1/(fs \cdot \sum_{i=1}^{M} w^2)$, respectively, where is w is the windowing function of length M and fs is the sample rate. The power spectrum or power spectral density is then averaged over the number of segments. Sound pressure levels were computed as $10\log_{10}\left(\frac{p^2}{p_{ref}^2}\right)$, where p^2 is the power spectrum in units of Pa^2 and p_{ref} is the reference pressure equal to 20 μPa (threshold of human hearing).

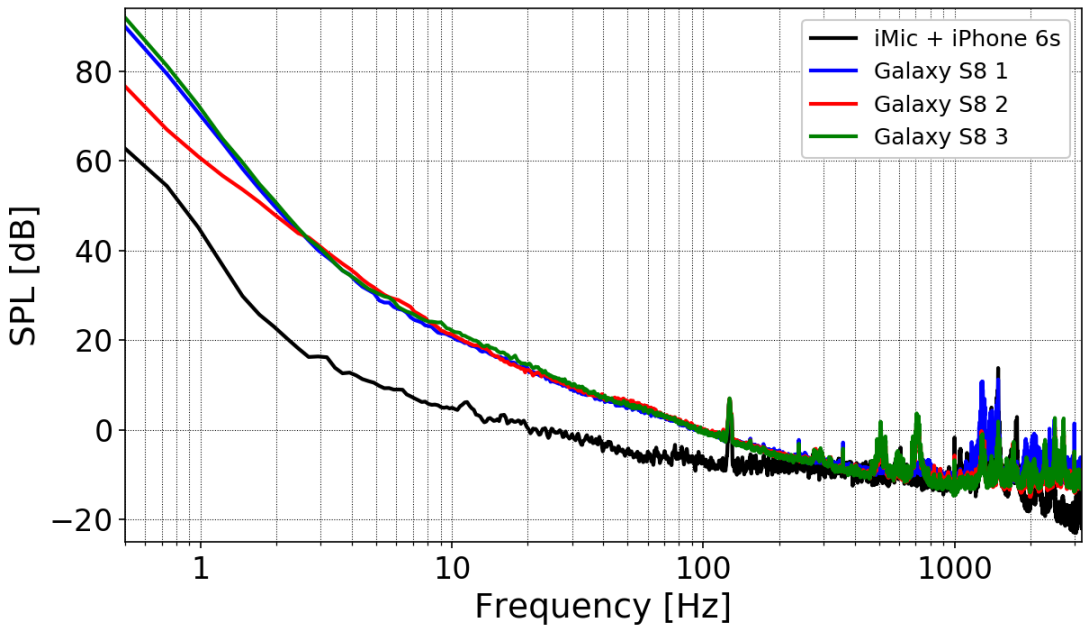

Figure 3.7. (Color online) Response corrected self-noise sound pressure levels of the iMic and three S8 sensors for a 10-minute record.

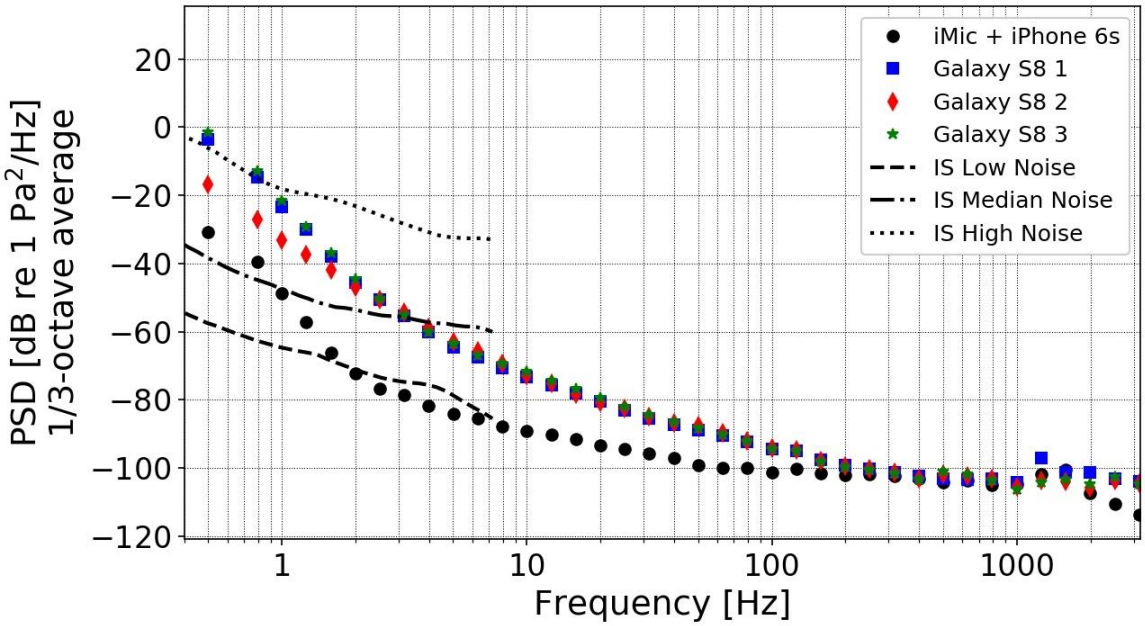

Figure 3.8. (Color online) Response corrected self-noise power spectral density levels averaged over 1/3-octave frequency bands. Ambient noise for infrasound stations that are part of the International Monitoring System (Bowmann *et al.,* 2007) are shown from 0.4 to 7 Hz. Sensor data corresponds to a 10-minute record for the iMic and three S8 sensors.

Self-noise power spectral density levels for the iMic and three S8 sensors are shown in Figure 3.7. Spectral peaks are visible for all sensors above 100 Hz, which likely correspond to external vibrations. In order to reduce randomness and external noise effects, spectral averaging over 1/3-octave bands was performed, and results are shown in Figure 3.8. Results show the iMic noise floor is below the reference sound level of 20 μPa (threshold of human hearing) above 20 Hz, and the S8 microphone is below the reference level above approximately 100 Hz. The iMic noise floor is more than 10 dB lower relative to the S8 noise floor up to the 63 Hz 1/3-octave band. The iMic sensor noise floor is within approximately 6 dB of the Low Noise Model for Infrasound Stations (Bowmann *et al.,* 2007) across 2 – 7 Hz. The S8 noise floors are lower than the High Noise Model above 1 Hz.

3.6 Summary

A method was developed for estimating the amplitude response of built-in smartphone microphone sensors in a non-isolated environment. A portable rotary subwoofer was used as a

controllable infrasound source to project pressure waves below 20 Hz. Mackie Subwoofer and Speakers served as sound projectors for tones above 20 Hz. A double reference sensor scheme was set up with the MB3 digital microbarometer (reference over the 0.5 - 2 Hz octave bands) and the iPrecisionMic smartphone microphone (reference above 2 Hz).

The response of the iPrecisionMic smartphone microphone (iMic) was first evaluated over the 1 – 2000 Hz octave bands, and results showed that by measuring the sensor's digital gain at 1 kHz, its amplitude response as a function of frequency can be estimated to within 5%. The iMic sensor was chosen as a reference in the evaluation of the response of three Samsung Galaxy S8 built-in smartphone microphones. The *Redvox Recorder* app for Android was used to measure pressure signals with the built-in microphones of the devices at the three available sample rates of the app: 80, 800, and 8000 samples/sec.

Microphone response measurements of each smartphone over the 0.5 – 2000 Hz octave bands showed an average variation with the app sample rate within 2%. Uncertainty levels and comparisons of the responses of the three test devices indicated the accuracy of the procedure to be within 1 dB (12%). An amplitude response model was estimated for the microphone of the Samsung Galaxy S8 (Model SM-G950U1) based on the measurement from the three smartphones; the model consisted of a 105 dB re 1 lsb/Pa digital gain with -3 dB low corner frequencies at 32, 8, 4, and 1 Hz. The mean measured levels deviated from the model within an average of 0.7 dB (8%). Further measurements over the 0.5 – 3162 Hz 1/3-octave bands of one of the smartphones showed an average deviation from the response model of less than 10%.

Self-noise measurements of the iMic sensor and the Samsung Galaxy S8 smartphone microphones showed that the noise floor of the iMic sensor was more than 8 dB lower than the Samsung Galaxy S8 microphones below 100 Hz. The iMic noise floor was observed to be below the reference sound level (20 μPa) above 20 Hz, and the Galaxy S8 microphone noise floor was below the reference above 100 Hz. Noise floors were compared to International Monitoring System infrasound ambient noise levels up to 7 Hz, and it was found that the iMic noise floor was within approximately 6 dB of the Low Noise Model across 2 – 7 Hz, and the Samsung Galaxy S8 smartphone noise floor were lower than the High Noise Model above 1 Hz. The results show an experimental capability for estimating the amplitude response of built-in smartphone microphone sensors from the infrasound range to the upper midrange in a non-isolated environment with conventional consumer products.

Acknowledgements

This work was supported by the Consortium for Verification Technology under Department of Energy National Nuclear Security Administration Award DE-NA0002534.

CHAPTER 4. REAL-TIME MONITORING AND DATA ANALYTICS IN MULTI-SENSING MOBILE SENSOR NETWORKS

In review as: Asmar, K., Christe, A., Williams, B., Watson, S., Chichester, D., and Garces, M. “Real-time monitoring and data analytics in multi-sensing mobile sensor networks”, *ACM Transactions on Data Science*

Abstract

The collection of acoustic data through crowdsourcing schemes with multi-sensing smartphones results in broadband mobile networks. This introduces a versatile global infrastructure that internally generates vast amounts of semi-structured and heterogeneous data streaming at high velocities. In order to extract meaningful knowledge and insights from the incoming data streams, protocols related to data management, processing, and analytics need to be readdressed. This work presents a data science approach for real-time sensor monitoring and acoustic data analysis in multi-sensing mobile networks. The ability to generate visual products (e.g., text, tables, graphs, images, maps) in real-time and through batch analysis is shown, and the potential use of these products for acoustic feature extraction, signal detection, and data-driven decision making is described.

4.1 Introduction

Smartphones are becoming increasingly prevalent as sensing systems within the scientific community. Since the appearance of the first iPhone in 2007, smartphones have evolved into multi-processor computers with built-in sensors such as microphones, barometers, accelerometers, magnetometers, and gyroscopes. The last decade has seen applications of smartphone sensors in seismic (Kong *et al.*, 2016; Minson *et al.*, 2015), sound and noise (Kardous and Shaw, 2014; Kardous and Shaw, 2016), and acoustic (Asmar *et al.*, 2016a; Asmar *et al.*, 2016b; Asmar *et al.,* 2018) measurements. The collection of acoustic data through crowdsourcing schemes with multi-sensing smartphones results in broadband mobile networks. This introduces a versatile global infrastructure that internally generates vast amounts of heterogeneous and semi-structured network-level (e.g., user id, location, device OS and type, etc.) and app-level (e.g., sensor payload, sampling rate, etc.) data streaming at high velocities (Yazti and Krishnaswamy*,* 2014; He *et al.,* 2016). The diverse embedded sensors and features of each smartphone in a network introduce veracity (e.g., timing, accuracy, quality processing, etc.) and variety (e.g., data from different sensors, changing sample rates, etc.) related issues into the mobile sensor data as well. In order to extract meaningful knowledge and insights from the incoming streams of data from mobile networks in real-time, data management and analytics protocols are readdressed.

This work presents a data science approach for sensor monitoring and knowledge extraction from acoustic data recorded with distributed smartphone sensor networks. The devices are running the *RedVox Recorder* app (RedVox, 2018), which accesses the embedded sensors and streams the data securely to a cloud server for analysis. By implementing the described approach in a big-data-capable cloud computing environment, we can dynamically scale computational resources to match real-time streaming needs and provide user-friendly visual products, which are generated with the potential for improving data-driven decision-making capabilities. In Section 4.2 we present a method for real-time monitoring of multi-sensing mobile devices in a distributed network. We use feature selection techniques to assess the physical, software, and streaming status of a device and ultimately present the information with visual products. In Section 4.3 we use feature extraction, dimensionality reduction, network time synchronization protocols, and traditional spectral analysis to produce real-time graph-based visual products. We proceed to perform batch analysis on the data parting from the real-time analytical results for the purposes of acoustic feature extraction. We describe in Section 4.4 a tonal signal detection algorithm that can be applied to real-time smartphone acoustic data. We apply the algorithm to a controlled data set to assess its detection performance of a high-signal-to-noise signal, and we describe how the implementation of the overall analysis/detection approach can contribute to industrial equipment monitoring capabilities. We summarize our observations and comment on the implications of our results in Section 4.5.

4.2 Real-time device monitoring

Real-time monitoring capabilities of mobile sensing devices are essential for field deployments. For packet-based data originating from multi-sensing mobile devices running the *RedVox app*, a feature selection approach can be used for remote device monitoring and data filtering. The app has options for private data streaming, meaning that only account users have access to the device data. Each packet that is sent to the cloud server by the app contains features such as user id, packet creation timestamp, device location, device temperature, device battery level, app version, device operating system (OS) and version, device make and model, acquisition and synchronization servers, privacy status, *RedVox* account login email, and payload for the enabled sensing channels. These data fields are used for real-time decision-making as well as stored and indexed in a database for batch and historical analysis. For remote monitoring, only the relevant features are kept. If the monitoring is to be done in real-time, the most recent packet is chosen. Batch analysis, however, can be performed to monitor any significant changes in the overall status of the device. For example, a device can be monitored remotely to check for continuous streaming (i.e., timestamp of latest packet), heating (i.e., temperature), power (i.e., battery level), automatic software updates (OS version), and acoustic data acquisition sample rate (i.e., microphone channel sample rate). Anomalies in any of these selected monitoring features can alert analysts and operators of possible issues with the sensing device that need to be physically assessed, and data-driven decisions regarding field troubleshooting can be made. Figure 4.1 shows visual products, accessible from an interactive web interface and generated with a cloud computing environment, that users can use to assess the physical and software status of mobile devices running the *RedVox* app.

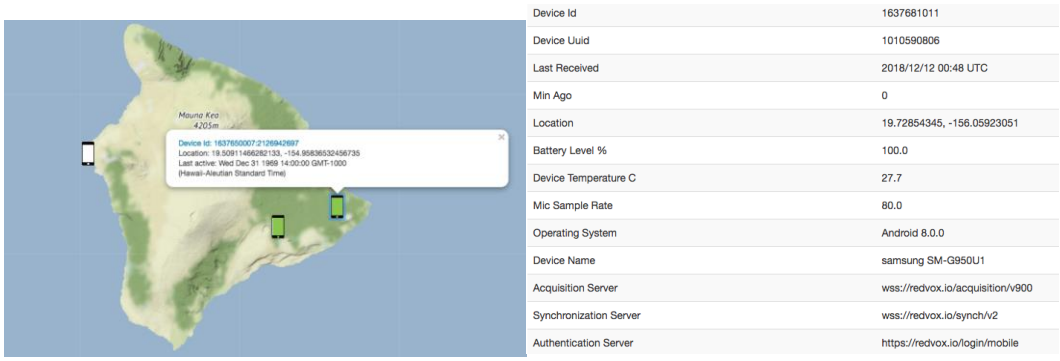

Figure 4.1. Example of visual products for real-time monitoring of smartphone devices deployed on the Big Island of Hawaii. On the left, icons in white show devices operating on iOS software, and icons in green show devices operating on Android software. By clicking on the icon the user can see the location coordinates of the device and the timestamp of the latest packet. On the right, the user can monitor the physical and software status of the device from the cloud environment. (redvox.io).

4.3 Real-time acoustic data analysis

4.3.1 Data cleaning, transformation, and processing

Data packets from multi-sensing devices running the *RedVox app* contain header information and payload values from several embedded sensors. For real-time data analysis and visual report generation, incoming data packets are first filtered and sorted by user id (i.e., device), packet creation timestamp (i.e., time window), and device location (i.e., distance from source). If the location of the event to be analyzed is known, the distance of each device from the event can be computed and used to assess the veracity and reliability of the acoustic data. For example, if the event is known to generate acoustic pressure waves within a limited range, the devices to be analyzed can be filtered to those deployed within that range.

Once the spatiotemporal filtered data packets for each device are obtained, acoustic analysis can be performed. The microphone channel payload of each packet is accessed, and dimensionality reduction techniques are used to obtain a single time series for the device within a given time period. Acoustic analysis is highly sensitive to sample rate, and therefore consecutive packets with the same sample rate need to be grouped for separate processing. For each packet within a common sample rate group, the time series payload (i.e., samples or counts), the timestamp of the first sample t_i, and the timestamp assigned by the device t_m to the start of the packet are extracted. Data packets for a same sample rate have the same duration and amount of microphone samples. The packet duration is equal to the difference between t_m of consecutive packets. If Δt_m is greater than this length plus a small error (due to the innate jitter of the device's autonomous clock), then one or more data packets are missing. The amount of missing data packets is equal to $\frac{\Delta t_m}{t_p}$, where t_p is the packet duration. For each missing packet, an array of zero-valued microphone payload values is created. A single waveform for the entire time period is obtained by concatenating all consecutive arrays of payload values.

The next step in the construction of a single time series is to build the time array by assigning the correct timestamp to each data sample. For this, the app version and time synchronization server are first assessed to determine whether the timing can be corrected. If the timing cannot be corrected, the time array is built by assigning the n^{th} sample in the time series the timestamp $t_{i0} + n/fs$, where fs is the sample rate and t_{i0} is t_i of the first sample in the waveform. If, however, the app is a later version and the device communicates with a reliable synchronization server, then time synchronization (described in Section 4.3.2) can be performed to improve the timing accuracy of the acoustic time series.

4.3.2 Time synchronization

In distributed signal processing systems such as a network of smartphone sensors, each node samples signals with its own analog-to-digital converter. As shown in Molnár *et al.,* (2003), the sampling of the analog data is controlled by autonomous clocks, which cannot generally be synchronized. This means that the timestamp associated with each sample has an offset and jitter with respect to the sampling frequency. In order to synchronize the discrete data sets from distributed systems in time, the offset of the clocks relative to a reference must be corrected. Messages must be exchanged between

node (i.e., smartphone) and reference (i.e., synchronization server) clock for determination of the relative offset, resulting in a *Tri-Message* time synchronization protocol (Tian *et al.,* 2009).

Figure 4.2 shows an example of four synchronizing nodes A, B, C, and D, consisting of smartphone devices running the *RedVox* app*.* The devices were placed on top of each other and sampled microphone data at 800 samples/sec. A pulse was generated at 23:12:45 UTC reference time. The recorded pulse times are shown in blue, and it can be seen that each node recorded the pulse at different times. By setting a common reference node, the records of A, B, C, and D can be synchronized with a common time base. The black lines in Figure 4.2 show the synchronized time series and Table 4.1 shows the offsets of the synchronizing nodes relative to the reference node. The offsets are based on the minimum achieved latency before synchronization. After synchronization, cross-correlation analysis indicates the relative delay between the records of nodes A, B, C, and D to be within less than 4 milliseconds (shown in Table 4.1). The final step before further analysis is to trim the time-series to start and end at the user-specified times.

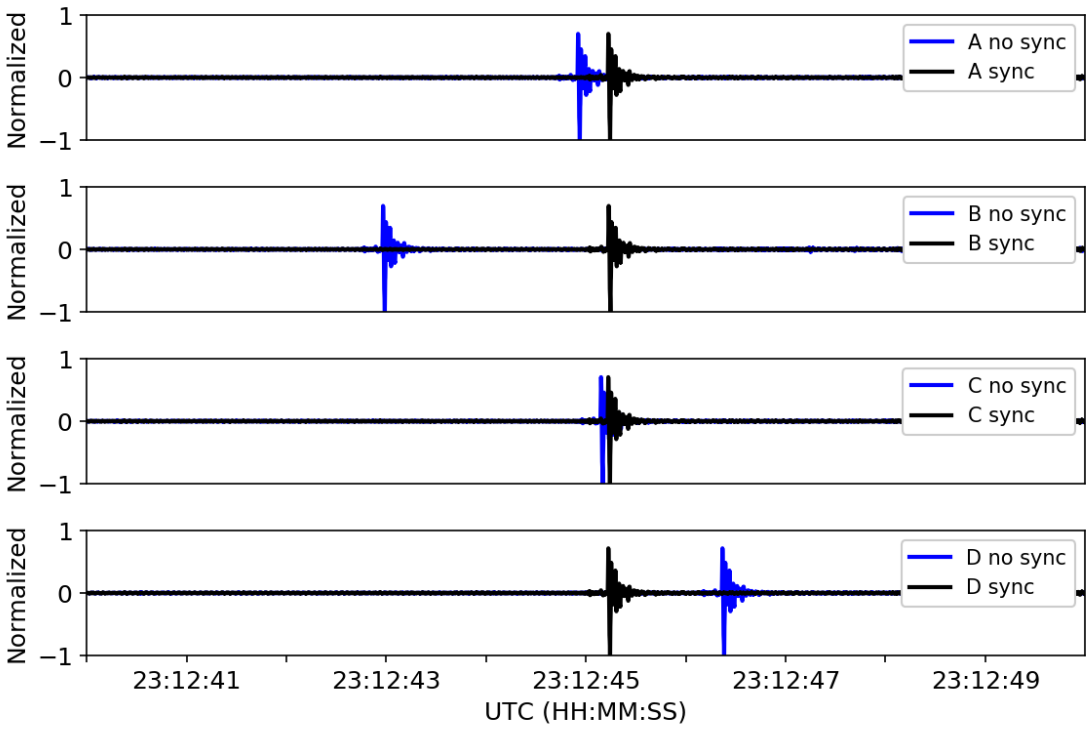

Figure 4.2. Waveforms for four co-located synchronizing nodes A, B, C, and D, before and after time synchronization. A pulse was generated at 23:12:45 UTC reference time. The blue lines represent the pulse recorded by the nodes before time synchronization. The black lines show the synchronized time series. The offsets (blue) before time synchronization were synchronized (black) to within less than 4 ms (see Table 4.1).

Table 4.1. Tri-message parameters for time synchronization of nodes A, B, C, and D, with common reference node. After time synchronization was performed, cross-correlation analysis yielded the relative delay between the waveforms of the synchronizing nodes, shown in the last column.

Synchronizing node	Minimum latency [ms]	Offset relative to reference node [ms]	Delay relative to node A after time synchronization [ms]
A	4.69	-1143	--
B	5.33	72.30	0
C	4.71	2259	3.75
D	6.86	305.2	3.75

4.3.3 Time-frequency analysis

Traditionally, acoustic records are first inspected in terms of quality and statistical properties in the time domain. The next step is to characterize the features of the signature, such as amplitude and phase, in the frequency domain. This process, often referred to as *spectral analysis*, computes a dynamic variable (such as power, energy, signal-to-noise ratio, etc.) as a function of frequency. The most common method used for spectral analysis of acoustic time series is the *Fourier* method, which is especially efficient when high spectral resolution is desired. By applying the *Discrete Fourier Transform* (DFT) to the digital time series, a frequency-domain representation composed of sinusoidal components is obtained for the record. The DFT is essentially a sequence of samples corresponding to the Fourier transform of the signal. When the frequency-domain properties of the signal vary with time, a *spectrogram* is computed. In this process, the *time-dependent Fourier* representation, the discrete time series is converted to a two-dimensional function of the time and frequency variables (Oppenheim, 1989). The resulting spectrogram is a representation of the magnitude of the dynamic spectral variable as a function of time-frequency windows.

In the *Fourier* method described in this article (Welch, 1967), the digital time series is first divided into 75% overlapping segments of equal size. The length of the segments is determined by the sample rate and desired spectral resolution. Each data segment is mean-subtracted and tapered with a *Hann* window of equal duration. The power spectrum is computed as the square of the Fourier transform of the tapered and mean-subtracted data segments. To correct the spectra for the windowing operation, each result is multiplied by a scaling factor $\frac{1}{\sum_{i=1}^{N} w^2}$, where w is the windowing function of length N. To compute the signal-to-noise spectrogram, the noise spectrum is first computed by taking the spectral average in time across the different frequency bands. The signal-to-noise ratio spectrogram is the ratio of the spectrum to the noise spectrum of the record per frequency band.

In cases where temporal resolution is desired over spectral resolution, a multiresolution approach (Garces, 2013) is used instead of the DFT. The multiresolution method allows for the spectral window size to be determined by the number of periods in each frequency band. This method is especially useful

for spectral analysis in the infrasound range, as it permits an adequate number of periods per band at lower frequencies. A bandpass filter is first applied to the data records at the corner frequencies of each fractional octave band, the order of which is chosen by the user. The data record is then divided into 75% overlapping segments of equal size. The size of the segments is chosen based on the center frequency of the band in order to allow for a minimum amount of periods for proper averaging. After removing the mean from each segment, the variance of the acoustic pressure over the time window is computed.

In order to accurately compute the time-varying spectral features of an acoustic record, any gaps in the data or consecutively repeated values surpassing a user-specified duration threshold must be removed from the spectral computation. These gaps are then replaced in the final visual product. The final step of the spectral analysis is to remove any previously known frequency responses from the data. For this, it is necessary to first assess whether the internal microphone of the device or an external microphone is being used for recording. This is specified by the sensor id feature in the microphone channel in a packet. If the internal microphone is being used, then the make and model of the device must be assessed in order to determine the corresponding response. The known responses can be stored in the production software and accessed when necessary. If the device has a known response, the response corrected power spectrum is computed as $P'_{xx}(f) = \frac{P_{xx}(f)}{H_x^*\left(e^{\frac{j\omega}{2\pi}}\right)H_x\left(e^{\frac{j\omega}{2\pi}}\right)}$, where H^* denotes the complex conjugate of the frequency response H, f is the frequency in Hz, $P_{xx}(f)$ is the raw power spectrum of time series x, and $P'_{xx}(f)$ is the response-corrected power spectrum. It is common in acoustics to represent the power spectrum in decibel units, as $10\log_{10}\left(\frac{P_{xx}}{p_{ref}}\right)$ dB relative to a reference p_{ref}. For response corrected power spectra, the units of P_{xx} are Pa^2. The sound pressure level can be obtained when the reference pressure is 20 μPa, and is equal to 0 dB at the threshold of human hearing.

4.3.4 Real-time visual products

Once a single time-series has been obtained for a device and spectral analysis has been performed, real-time visual products can be generated for further analysis and feature extraction to improve decision-making capabilities. For this it is first necessary to standardize plot production. This can be done using object-oriented programming techniques for the standardization of plot features such as figure size, data dimensions, font size, labels, axes limits, etc. The products can be accessed and modified by users via an interactive web interface.

Figure 4.3 shows an example of a visual product representing the raw time series and multiresolution spectral analysis results for a data record from a Samsung Galaxy S8 smartphone (Model SM-G950U1) running the *RedVox app*. The plots show seismo-acoustic signatures generated by a M6.9 earthquake occurring approximately 115 km away from the device. Figure 4.4 shows an acoustic record, analyzed in the time-frequency domain with the Fourier method, obtained with a Samsung Galaxy S8 smartphone (Model SM-G950U1) sensor running the *RedVox app*. The plots show acoustic signatures by a diesel generator (Asmar *et al.,* 2018).

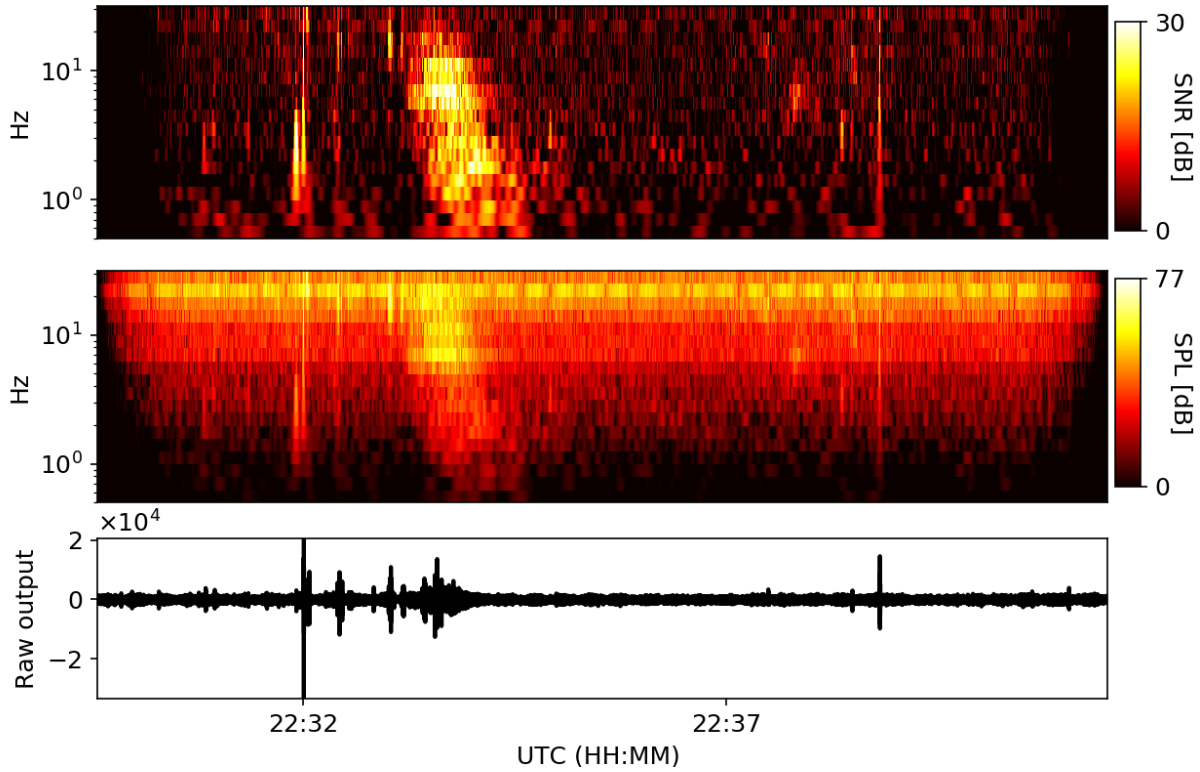

Figure 4.3. Example of a real-time visual product for acoustic data sampled at 80 samples/sec from a Samsung Galaxy S8 Model SM-G950U1 smartphone running the *RedVox* app version 2.2.6. The bottom window shows the raw time series. The middle panel shows the power scalogram computed with 3rd octave multiresolution analysis. The top panel shows the signal-to-noise scalogram. Both scalograms show broadband transient signals around 22:33 UTC across 0.5 – 20 Hz, corresponding to seismo-acoustic waves generated by a M6.9 earthquake occurring ~115 km from the device.

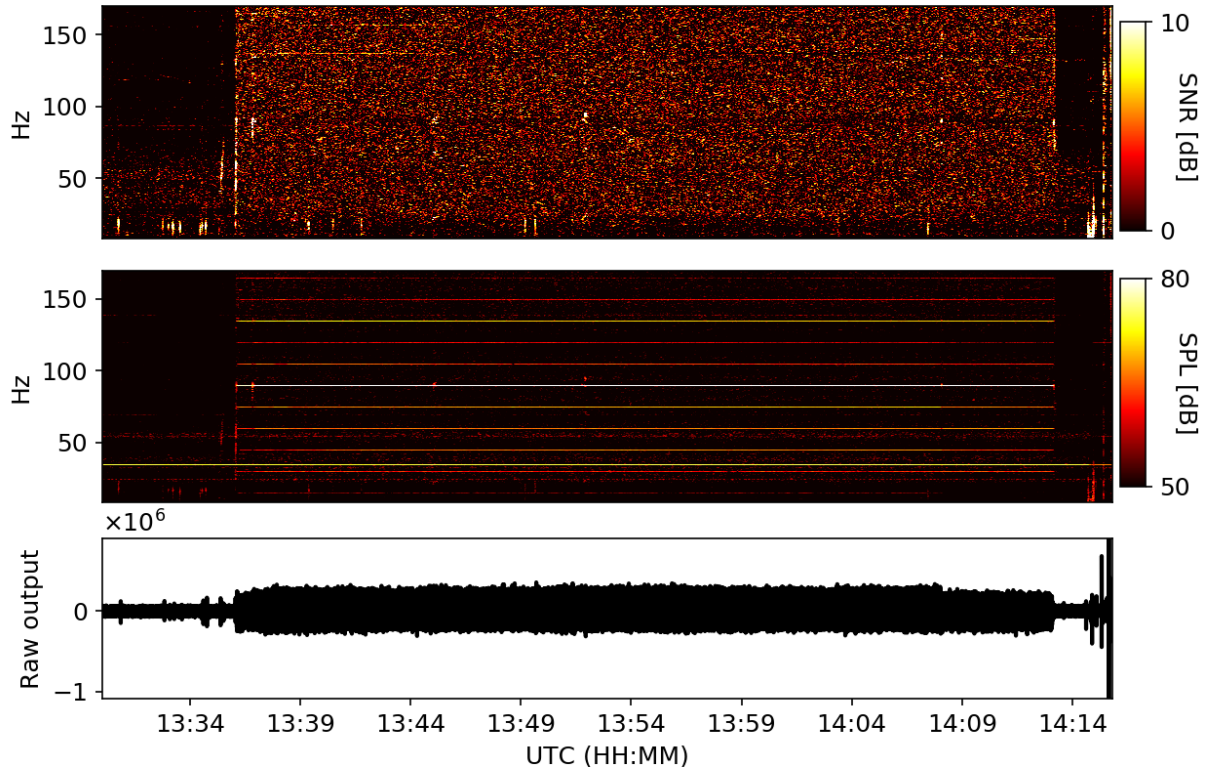

Figure 4.4. Example of a real-time visual product for a acoustic data sampled at 800 samples/sec from a Samsung Galaxy S8 (Model SM-G950U1) smartphone running the *RedVox* app version 2.3.15. The data correspond to a diesel generator startup/shutdown. Spectral analysis was performed with the Fourier method. The time window size was set to 8192 samples to obtain a spectral resolution of 0.1 Hz. The bottom window shows the raw digital output of the app in the time domain. The middle panel shows the sound pressure level (SPL) spectrogram in decibels after removing the sensor response from the spectral data. The top panel shows the signal-to-noise (SNR) spectrogram in decibels. An amplitude increase in the raw waveform is seen from the startup time (~13:36 UTC) to shutdown (~14:13 UTC). Similarly, increased ambient noise levels are seen across the same time window in the signal-to-noise spectrogram above 10 Hz. Distinct tonal signals at 15 Hz intervals are seen in the SPL spectrogram (middle panel) during the time the generator was on. A closer look at these tones is shown in Figure 4.6.

4.3.5 Batch analysis and feature extraction

Real-time visual products for the representation of acoustic data, such as those shown in Section 4.3.4, can enable analysts to perform further analysis in batch form to extract relevant acoustic features and make data-driven decisions. For example, after assessing Figure 4.4 in real-time, an analyst may proceed to perform array processing for an array of sensors close enough to the source for event localization. Similarly, the data record shown in Figure 4.4 can be further analyzed to assess the acoustic behavior of a diesel generator. Figure 4.5 shows sound pressure levels (SPL) at frequencies of interest corresponding to the time record shown in Figure 4.4. Average signal-to-noise ratio values are shown in

Table 4.2, with $\mathrm{SPL}_{\mathrm{noise}}$ considered as the mean SPL of a 30-minute window of the record when the generator was OFF, and $\mathrm{SPL}_{\mathrm{signal}}$ the mean power of a 30-minute window of the record when the generator was ON. These features could prove useful for monitoring industrial equipment with smartphone acoustic sensors, as described in Section 4.4.

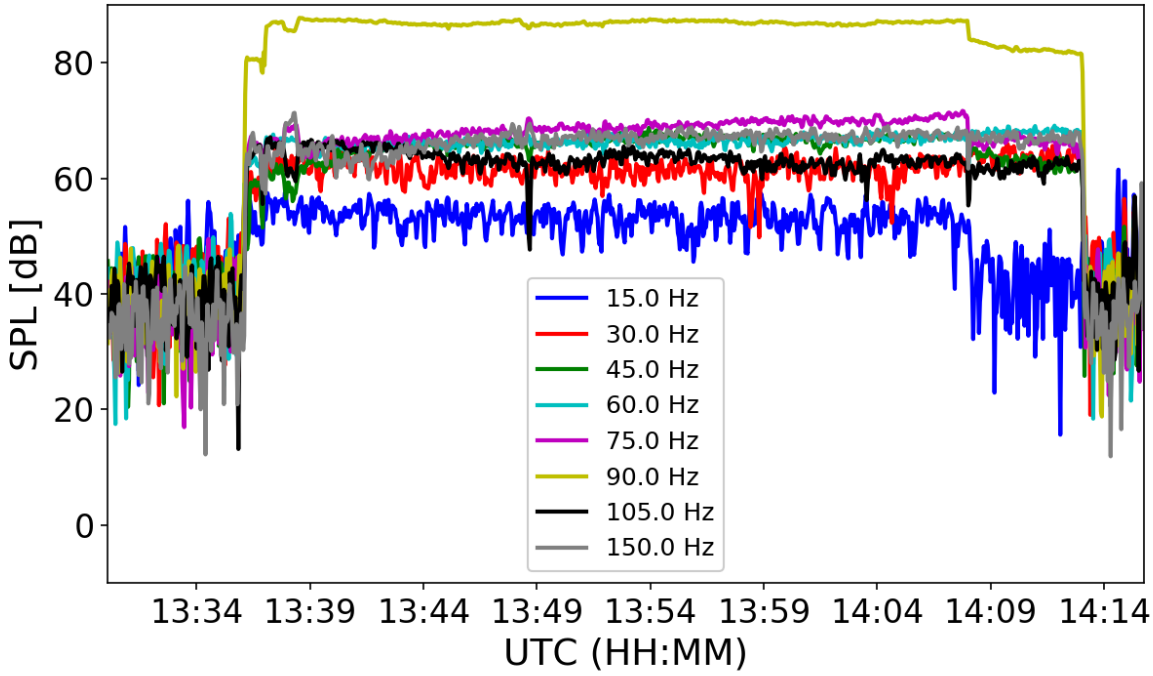

Figure 4.5. Sound pressure level (SPL) increase at frequencies of interest during diesel generator startup (~13:36 UTC) and shutdown (~14:13 UTC) described in Figure 4.5. All frequencies correspond to harmonics of fundamental 15 Hz. The highest SPL is seen at 90 Hz.

Table 4.2. Mean sound pressure levels (SPL) in decibels at frequencies of interest during 30-minute windows when the diesel generator was OFF ($\mathrm{SPL}_{\mathrm{noise}}$) and ON ($\mathrm{SPL}_{\mathrm{signal}}$). The levels and frequencies correspond to those shown in Figure 4.5, with spectral resolution 0.1 Hz. The increase in sound pressure level after startup, or $\mathrm{SPL}_{\mathrm{signal}} - \mathrm{SPL}_{\mathrm{noise}}$, is shown in the last column.

Frequency [Hz]	**Mean SPL noise (Generator OFF) [dB]**	**Mean SPL signal (Generator ON) [dB]**	**Mean SNR [dB]**
15.0	37.5 $\pm$ 5.6	52.3 $\pm$ 3.7	14.8
30.0	41.1 $\pm$ 5.8	61.6 $\pm$ 1.9	20.5
45.0	39.9 $\pm$ 6.4	66.2 $\pm$ 1.1	26.3

60.0	40.8 ± 5.6	66.4 ± 0.9	25.6
75.0	36.5 ± 5.6	68.7 ± 1.5	32.2
90.0	38.8 ± 5.7	86.7 ± 1.0	47.9
105.0	36.7 ± 5.2	63.1 ± 1.8	26.4
150.0	34.3 ± 5.7	66.7 ± 1.5	32.4

4.4 Acoustic tonal signal detection

4.4.1 Detection algorithm

Real-time monitoring and analytics of acoustic data from mobile devices can enable automated signal detection. Correlation analysis has previously been used in acoustics for the detection of broadband signals (Adrián-Martínez *et al.*, 2015) and array processing (Mialle *et al.*, 2019). For the detection of tonal signals, such as those shown in Figure 4.6, convolution analysis can be useful. Previous efforts for tonal signal detection are described in Chu *et al.* (2014) and Wang and Wan (2005). The algorithm for tonal detection described in this section is based on identifying slope changes in the convolution function between a particular data set and a synthetic step function. In order for the algorithm to identify the tonal signature, the frequency of the tone must be known. The user first specifies a desired frequency band with a certain spectral resolution. A Fourier power spectrogram is generated as described in Section 4.3.3. The spectral record at the chosen frequency band is mean-subtracted and fed into the detection algorithm.

The algorithm performs discrete linear convolution between the spectral record $f[k]$ of length *M* and a synthetic step function $g[k]$ of length *2M*, given by Eq. (4.1).

$$g[k] = \begin{cases} 1 \; if \; 0 \; \leq k < M \\ -1 \; if \; M \; \leq k < 2M \end{cases} \tag{4.1}$$

$$(f * g)[n] = \sum_{m=-\infty}^{\infty} f[m]g[n-m] = \sum_{m=-\infty}^{\infty} g[m]f[n-m] \tag{4.2}$$

The convolution product, calculated as shown in Eq. (4.4), is only kept for points where the signals overlap and has length *M + 1*. That is, only the values not requiring zero-padding are kept. This results in a convolution function with a negative slope whenever there is a step with sufficient signal-to-noise in the power record, as shown in Figure 4.6.

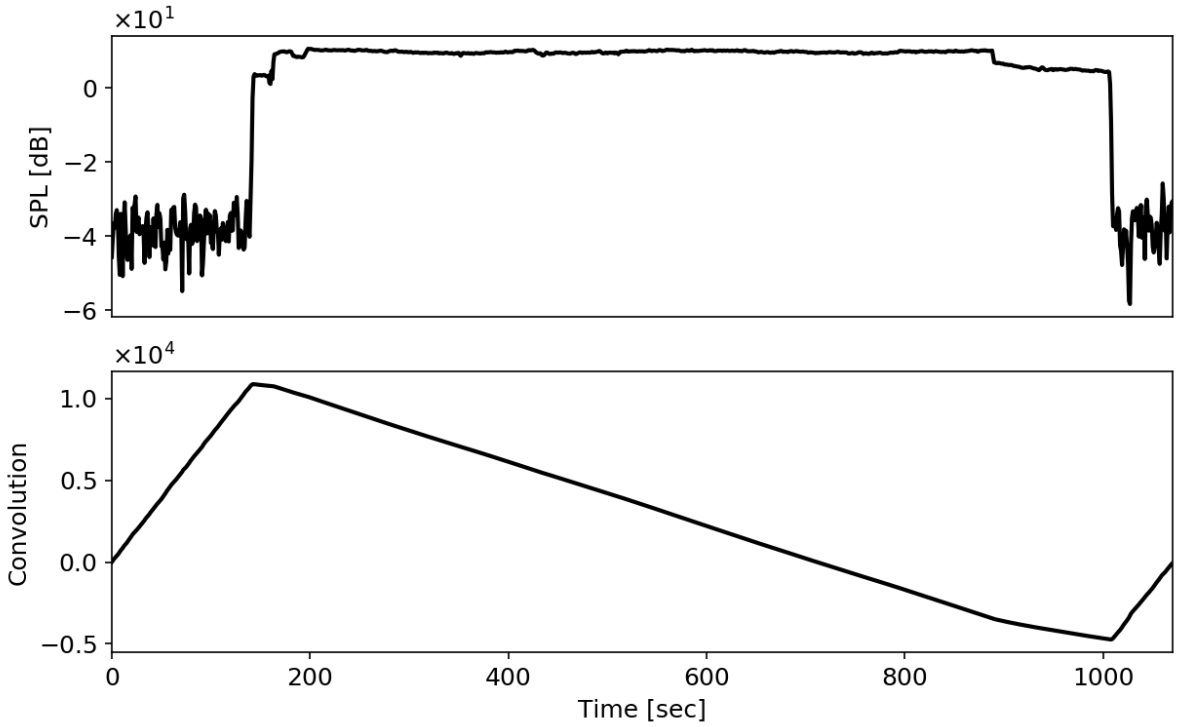

Figure 4.6. Example of convolution function related to the mean-subtracted spectral power function at 90 Hz (47.9 dB signal-to-noise shown in Table 4.2) of a diesel generator (see Figure 4.6) over time. The bottom window represents the convolution function between the power record (top window) and a synthetic step function (Eq. (4.1)). Negative slopes are visible in the convolution whenever there is a step increase in power levels.

The next step consists of detecting the negative slopes of the resulting convolution function. For this, it is necessary to have some idea of the duration of the signal to be detected. User-specified thresholds must be set for the signal and gap duration (SDT and GDT, respectively). From Figure 4.6, it can be seen that the overall trend of the convolution function is negative when there is a tonal signal that stands out from the ambient noise. However, due to randomness in the record, some negative trends may be present in the noise. In order to eliminate those random values and increase detection probability, it is necessary to specify the minimum duration of the signal for the negative trend to be considered. Similarly, random energy fluctuations during the signal may present themselves in intermittent positive trends in the overall negative trend of the convolution during the signal. A threshold for the maximum duration of these random gaps must be determined by the user for them to be discarded. The algorithm detects the beginning and end times of the negative slopes, which correspond to the approximate start and stop times of the rectangular energy pulse.

4.4.2 Performance statistics of the algorithm with a controlled data set

In order to evaluate the performance of the detection algorithm, a data set was generated from a controllable sound source. The data were captured by distributed smartphone sensors and streamed to Cloud Services, after which it was fed into the algorithm. Twenty Samsung Galaxy S8 (Model SM-G950U1) smartphones running the *RedVox* app and sampling acoustic data at 800 samples/sec were placed in groups of five at four different locations relative to a sound source inside a building. Two groups of smartphones were outside the building at approximately 56 and 22 meters from the source. The other two groups were inside the building at approximately 23 and 7 meters from the source (see Figure 4.7). A 125 Hz signal was generated with a Tektronix RM 3100 signal generator, using a Mackie Active Subwoofer Model SWA1801z as the sound projector. The sound projector was oriented facing the smartphones placed ~56 meters outside the building. The signal was generated five times with duration of 2 minutes, in approximately 2-3 minute intervals. Time synchronization analysis, described in section 4.3.2, was performed on the data to increase timing accuracy. With 20 devices recording 5 signals, the controlled data set corresponds to 100 possible correct detections. Sound pressure levels for a smartphone device from each group of distributed sensors are shown in Figure 4.8.

Figure 4.7. Map visualization of distributed smartphone sensors (yellow icons) and controllable sound source (red icon).

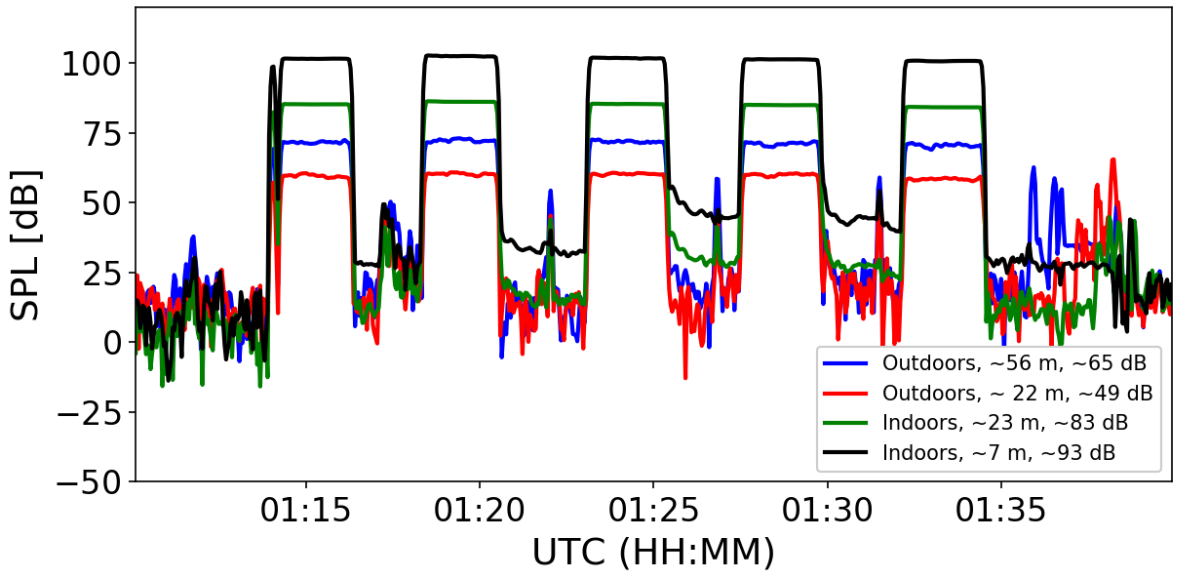

Figure 4.8. Sound pressure levels (SPL) in decibels at 125 Hz (computed with 0.1 Hz spectral resolution) for one device from each group of smartphone sensors. The 2-minute signal was generated five times, and can be seen as a rectangular pulse in the SPL record. Each group consisted of five sensors placed a certain distance from the sound source, which was indoors. Data are labeled with device location (outdoors or indoors), approximate distance from source in meters, and approximate signal-to-noise ratio in decibels recorded during the signal at 125 Hz. The sound projector was oriented facing the smartphones placed ~56 meters outside the building, and the result can be seen in a higher SPL (blue) measured than the smartphones placed ~22 meters outside the building (red), in opposite direction to the sound projection.

The performance evaluation of the algorithm with a controlled data set consists of evaluating the detection capability with different combinations of the user-specified parameters: spectral resolution (SR), signal duration threshold (SDT), and gap duration threshold (GDT). A true positive (TP) consists of a correct detection of a signal that is present (in the case we are presenting, if the signal start and stop times are detected to within 30-second precision). A true negative (TN) consists of a correct rejection of a signal that is not present. A false positive (FP) consists of an incorrect detection of a signal that is not present. A false negative (FN) consists of an incorrect rejection of a signal that is present. For each combination of parameters, the *sensitivity* (SEN) and *positive predictive value* (PPV) were evaluated as

$$SEN = \frac{TP}{TP+FN} \tag{4.5}$$

$$PPV = \frac{TP}{TP+FP}. \tag{4.6}$$

The sensitivity is essentially the ability of the algorithm to detect the presence of a signal when it exists. This is also known as the probability of detection or true positive rate. The positive predictive value is the proportion of positives that correspond to the presence of the signal. If the algorithm correctly detects all present signals and rejects all not present signals, then the sensitivity and positive predictive value are equal to 1 (Fawcett, 2005).

The algorithm was tested with spectral resolutions of 0.1, 0.2, 0.4, 0.8, 1.6, 3.1, and 6.3 Hz, which correspond to spectral window sizes (N_w) of 8192, 4096, 2048, 1024, 512, 256, and 128 samples, respectively. For each spectral resolution, the combinations of signal and gap duration thresholds shown in Table 4.3 were applied. This resulted in a total of 322 combinations of (N_w, SDT, GDT).

Table 4.3. Combinations of user-specified parameters: signal duration threshold (SDT) and gap duration threshold (GDT) used for testing signal detection algorithm.

SDT (seconds)	**GDT (seconds, in 5-second increments)**
15	5
30	5 to 10
60	5 to 30
75	5 to 40
90	5 to 40
105	5 to 50
120	5 to 55

Upon performance analysis, the SEN and PPV of the algorithm were found to be equal to 1 for 99.1% and 97.2% of the 322 combinations, respectively. The combinations that yielded SEN and PPV values lower than 1 are shown in Tables 4.4 and 4.5.

Table 4.4. Sensitivity (SEN) values not equal to 1 per combination of user-specified parameters: spectral resolution, signal and gap duration threshold (N_w, SDT, GDT).

(N_w, SDT [sec], GDT [sec])	**SEN**
(8192, 105, 50)	0.6
(8192, 120, 50)	0.6
(8192, 120, 55)	0.4

Table 4.5. Positive Predictive Values (PPV) not equal to 1 per combination of user-specified parameters: spectral resolution, signal and gap duration threshold (N_w, SDT, GDT).

(N_w, SDT [sec], GDT [sec])	PPV
(8192, 15, 5)	0.862
(8192, 30, 5)	0.971
(8192, 30, 10)	0.971
(4096, 15, 5)	0.943
(2048, 15, 5)	0.917
(1024, 15, 5)	0.971
(512, 15, 5)	0.971
(256, 15, 5)	0.962
(128, 15, 5)	0.990

For this test scenario, it can be seen that the algorithm performed optimally without false negatives 99.1% of the time and without false positives 97.2% of the time, out of a total of 322 combinations of user-specified parameters. The controlled case presented in this section corresponds to the detection of high signal-to-noise tonal signatures. Real-life acoustic signatures do not always present themselves with sufficiently high signal-to-noise, and thus can be missed without optimization of the detection algorithm. Further work needs to be done to determine the signal-to-noise threshold for detection of tonal signatures in various environments.

4.4.3 Approach for real-time monitoring of industrial equipment

Industrial equipment can be recognized from the sound emitted (i.e., acoustic signature) during operations. The implementation of the signal detection algorithm described in Section 4.4.1 could potentially contribute to the monitoring of industrial equipment for purposes such as faulty equipment detection and industrial facility monitoring (Uematsu *et al.,* 2017; Watson *et al.,* 2018). As an example, Figure 4.9 shows spectral analysis results from a Samsung Galaxy S8 (Model SM-G950U1) smartphone running the *RedVox app* deployed approximately 3 meters from a cooling tower in a nuclear facility. The figure shows the cooling tower in operation until around 19:56 UTC, when it was shut down. Clear signals are visible at 8.6 and 25.8 Hz during the time the cooling tower was in operation. A closer look at the different frequency bands, shown in Table 4.6, shows the frequency bands (overtones of 8.6 Hz) with the highest sound pressure levels during the time the cooling tower was on. The monitoring of cooling tower startups/shutdowns could therefore be achieved by implementing the detection algorithm (described in Section 4.4.1) to spectral records at the frequencies shown in Table 4.6 from smartphones deployed near the tower. Given that acoustic feature extraction can potentially be performed in real-time (see Sections 4.3.4 and 4.3.5, respectively), we propose that implementing the tonal signal detection algorithm in real-

time to acoustic datasets obtained with multi-sensing mobile devices could contribute to the monitoring of industrial equipment, once the frequencies of interest are known.

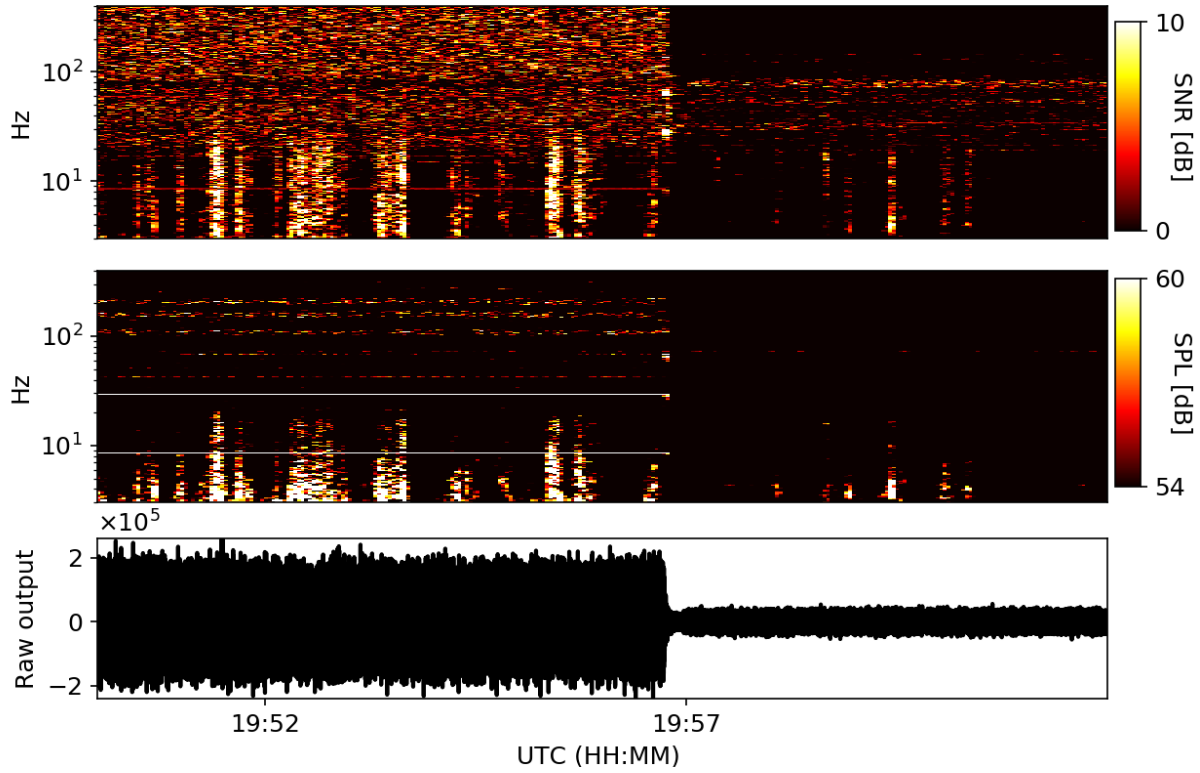

Figure 4.9. Spectral analysis results for an acoustic record corresponding to a cooling tower shutdown measured with a Samsung Galaxy S8 (Model SM-G950U1) smartphone running the *RedVox Infrasound* app at 800 samples/sec sample rate. The spectral window size was set to 8192 samples to obtain a spectral resolution of 0.1 Hz. The bottom window shows the raw digital output of the app in the time domain. The middle panel shows the sound pressure level (SPL) spectrogram in decibels. The top panel shows the signal-to-noise (SNR) spectrogram in decibels. An amplitude decrease in the raw waveform is seen at the time of shutdown (~19:56 UTC). Similarly, increased ambient noise levels are seen across the same time window in the signal-to-noise spectrogram above 20 Hz. Distinct signals are seen in the power spectrogram (middle panel) during the time the cooling tower was on around 8.6 and its 25.8 Hz overtone.

Table 4.6. Mean sound pressure levels (SPL) in decibels at frequencies of interest during 5-minute windows when the cooling tower was OFF (noise) and ON (signal). The levels and frequencies correspond to those shown in Figure 4.10, with spectral resolution 0.1 Hz. The decrease in sound pressure level after shutdown, corresponding to the signal-to-noise ratio (SNR) of the cooling tower operation, is shown in the last column.

Frequency [Hz]	**Mean SPL noise (Cooling tower OFF) [dB]**	**Mean SPL signal (Cooling tower ON) [dB]**	**Mean SNR [dB]**
8.6	38.1 $\pm$ 7.0	70.5 $\pm$ 0.5	32.4
68.8	37.2 $\pm$ 5.7	71.2 $\pm$ 1.1	34.0
137.6	35.3 $\pm$ 5.1	78.3 $\pm$ 1.0	43.0
163.4	33.0 $\pm$ 4.6	62.6 $\pm$ 2.6	29.6
172.0	32.2 $\pm$ 5.3	62.6 $\pm$ 1.9	30.4

4.5 Summary and future work

A data science approach for real-time sensor monitoring and acoustic data analysis in multi-sensing mobile networks was presented. Real-time visual products generated with the approach were shown, and examples of acoustic feature extraction and signal detection from further batch analysis were described. The implementation of such monitoring and analytics products in a big-data-capable Cloud Computing environment could significantly improve data-driven decision-making capabilities related to field deployments, geophysical hazard monitoring, and industrial equipment monitoring.

Acknowledgements

This work was funded by the Consortium for Verification Technology under Department of Energy National Nuclear Security Administration Award No. DE-NA0002534, Multi-informatics for Nuclear Operations Scenarios under Department of Energy National Nuclear Security Administration Award No. DE-AC07-05ID14517, Defense Nuclear Nonproliferation Research and Development, and Office of Proliferation Detection.

CHAPTER 5. CONCLUSIONS AND FUTURE WORK

5.1 Summary

This dissertation presented experimental and computational capabilities for the modernization of conventional infrasound technologies. The characterization and analytics methods described can enable the integration of next-generation sensors as supplements to current regional and global infrasound networks. These networks are currently in use for geophysical and nuclear monitoring, and their modernization could help reduce cost and increase deployment and data-driven decision-making efficiency.

Chapter 2 described the characterization of two next-generation digital acoustic sensors against their analog predecessors across the infrasound range in non-isolated conditions. Parametric responses in the digital domain were developed for the MB3 digital microbarometer (across 0.01 – 4 Hz) and the iPrecisionMic microphone (across 1 – 20 Hz). By overlapping both responses, next-generation digital sensor performance across the infrasound range can be benchmarked.

Chapter 3 presented a method for estimating the amplitude response of built-in smartphone microphone sensors in a non-isolated environment. A double reference sensor scheme was set up with the previously calibratred MB3 digital microbarometer (reference across 0.1 - 2 Hz) and the iPrecisionMic smartphone microphone (reference above 2 Hz). The response of the iPrecisionMic smartphone microphone (iMic) was first evaluated across 1 – 2000 Hz octave bands. The *Redvox Recorder* app for Android was used to measure pressure signals with the built-in microphones of three Samsung Galaxy S8 (Model SM-G950U1) smartphones, and an amplitude response model was estimated based on the measurements. The results showed an experimental capability for estimating the amplitude response of built-in smartphone microphone sensors from the infrasound range to the upper midrange in a non-isolated environment with conventional consumer products.

Chapter 4 presented a data science approach for real-time sensor monitoring and acoustic analysis in multi-sensing mobile networks. Real-time visual products generated with the approach were shown, and examples of acoustic feature extraction and signal detection from further batch analysis were described.

The results of this dissertation research aim to provide novel and accessible approaches that can efficiently contribute to the development of next-generation technologies and analytics for infrasound global networks.

5.2 Future work and recommendations

It is recommended that further tests be performed to validate the stability and repeatability of the parametric responses of the MB3 digital microbarometer and iPrecision microphone sensors under more diverse conditions. Upon response validation, these sensors can be established as references for future

digital calibrations and acoustic pressure measurements across 0.01 – 4000 Hz. Data science approaches, such as those described in Chapter 4, can be applied to the smartphone characterization methods described in Chapter 3 in order to standardize and increase the efficiency of on-site calibrations. The implementation of an interactive web interface that can allow users to analyze calibration datasets in real-time is currently in progress. By automating analysis algorithms, parametric responses can be estimated in real-time. These responses can then be stored in a cloud database accessible to cleared users. Further work also needs to be done to determine the signal-to-noise threshold for detection of tonal signatures (as described in Chapter 4) in various environments.

5.3 Contributions and implications

The integration of next-generation digital acoustic sensors in conventional technologies could help supplement regional and global networks. These networks currently monitor nuclear and geophysical hazards around the world. The use of mobile sensing devices could increase network deployment efficiency while decreasing geographical limitations and operational cost. The implementation of the experimental and computational capabilities presented in this dissertation can contribute to the modernization of conventional technologies as well as the improvement of data-driven decision-making protocols related to field deployments, geophysical hazard monitoring, and industrial equipment monitoring with infrasound systems.

APPENDIX A

Equipment	Serial No.
MB2000 microbarometer	1008
Reftek digitizer Model 130-01	9DDI
MB3d microbarometer	00009
iPrecision microphone	CQ10003
Brüel & Kjaer Microphone Type 4193	1886683
Brüel & Kjaer Preamplifier Type ZC-0032	16869
Brüel & Kjaer Hand Held Analyzer Type 2250	3001392
Brüel & Kjaer Acoustic Calibrator Type 4231	3020813
Tektronix RM 3100 signal generator	C010108
Thigpen Rotary Woofer Model 17	1708050115
Mackie Active Subwoofer SWA1801Z	(21)TK12575
Mackie Speaker S215	(21)PM12059

REFERENCES

Adrián-Martínez, S., Ardid, M., Bou-Cabo, M., Felis, I., Llorens, C., Martínez-Mora, J. A., and Saldaña, M. (2015) “Acoustic signal detection through the cross-correlation method in experiments with different signal to noise ratio and reverberation conditions” in *Ad-hoc Networks and Wireless: ADHOC-NOW 2014 International Workshops ETSD, MARSS, MWaoN, SecAN, SSPA, and WiARN, Benidorm, Spain, June 22-27, 2014, Revised Selected Papers*, edited by García Pineda, M., Lloret, J., Papavassiliou, S., Ruehrup, S., and Wesphall, C. B., Springer, Berlin, pp. 66-79

Amazon Web Services (2018) Available at https://aws.amazon.com/what-is-cloud-computing/?nc1=h_ls (Last viewed December 6, 2018)

American National Standards Institute, Inc. (1997) “Methods for calculation of the speech intelligibility index” ANSI S3.5 1997, American National Standards Institute, 1997

Asmar, K., Garces, M. Schnurr, J., and Christe, A. (2016a) “Rocket infrasound signatures recorded with smartphones” Consortium for Verification Technology Workshop, Ann Arbor, Michigan, 19-20 October

Asmar, K., Garces, M. Schnurr, J., and Christe, A. (2016b) “Surf infrasound recorded with smartphones during the 2016 Eddie Aikau” 5th Joint Meeting of the Acoustical Society of America and Acoustical Society of Japan, Honolulu, Hawaii, 28 November – 2 December

Asmar, K., Garces, M., Williams, B., Christe, A., Chichester, D., Watson, S., Holschuh, T., and Cardenas, E. (2018a) “Infrasound and low-frequency acoustic emissions from nuclear facilities recorded with smartphones” *Consortium for Verification Technology Workshop*, Ann Arbor, Michigan, USA 31st October – 1st November

Asmar, K., Garces, M., Hart, D., and Williams, B. (2018b) “Digital acoustic sensor performance across the infrasound range in non-isolated conditions” *J. Acoust. Soc. Am.* 144(5), 3036-3045

Assink, J. D., Evers, L. G., Holleman, I., and Paulssen, H. (2008) “Characterization of infrasound from lightning” *Geophysical Research Letters, 35*(15)

Audio Control (2018). Available at http://www.audiocontrol.com/pro-audio/mobile-solutions/iprecisionmic/, (Last viewed November 19, 2018)

Balachandran, N. K. and Donn, W. L. (1971) “Characteristics of Infrasonic Signals from Rockets” *Geophysical Journal of the Royal Astronomical Society, (26)*135-148

Bendat, J. S. and Piersol, A. G. (1986) *Random Data Analysis Measurement Procedures,* 2nd Ed. (Revised and Expanded), (John Wiley & Sons, Inc., New York)

Bowman J.R., Shields, G. and O’Brien, M.S. (2007) “Infrasound station ambient noise estimates and models”, Infrasound Technology Workshop, Tokyo, Japan, 13-16 November.

Brown, R. and Evans, L. (2011) “Acoustics and the smartphone” Proceedings of Acoustics, Gold Coast, Australia, 2-4 November

Brüel, D. and Kjaer, V. (1995) *Technical Documentation, Microphone Handbook* [Available at https://www.bksv.com/media/doc/be1373.pdf], 216 pp.

Brüel, D. and Kjaer, V. (1996) *Technical Documentation, Microphone Handbook: Volume 1, Theory* [Available at https://www.bksv.com/media/doc/be1447.pdf], 155 pp.

Brüel & Kjaer (2014) “Product Data: Sount Calibrator Type 4231”. Datasheet, 4pp. [Available online at https://www.bksv.com/media/doc/bp1311.pdf]

CEA/DAM (2009) “MB2000 and MB2005 microbarometers”. [Available online at http://www-dase.cea.fr/public/dossiers_thematiques/microbarometres/description_en.html] (Last viewed November 19, 2018)

Ceranna, L., Le Pichon, A., Green, D. N., and Mialle, P. (2009) “ The Buncefield explosion: a benchmark for infrasound analysis across Central Europe” *Geophysical Journal International, 177*(2), 491-508

Chaparral Physics (2011) *Operation manual for the Model 50A infrasound sensor*, Rev. May 2010, [Available online at http://www.gi.alaska.edu/files/Model%2050A%20Manual%20beta.pdf], 17 pp. (Last viewed on November 20, 2018)

Christe, A., Garces, M., Asmar, K., Magana-Zook, S., Gaylord, J., and Chichester, D. (2018) “Enabling Multi-Informatics for Nuclear Operations Scenario via a Scalable and Data Agnostic Framework” *Consortium for Verification Technology Workshop*, Ann Arbor, Michigan, USA 31st October – 1st November

Christie, D. R. and Campus, P. (2010) “The IMS Infrasound Network: Design and Establishment of Infrasound Stations”, in *Infrasound Monitoring for Atmospheric Studies*, edited by Le Pichon, A., Blanc, E., and Hauchecorne, A. (Springer, Dordrecht Heidelberg London New York) pp. 29 – 75

Chu, C., Shen, L., and Hwang, S. (2014) “A New Algorithm for Tone Detection” *AASRI Procedia 8*:118-122

CTBTO (2001) “The Global Verification Regime and the International Monitoring System”, CTBTO Preparatory Commission, Vienna International Centre, Vienna, Austria

Eminent Technologies (2018) available at http://www.eminent-tech.com/ (Last viewed November 19, 2018)

Evers, L. G. and Haak, H. W. (2010) “The Characteristics of Infrasound, its Propagation and Some Early History”, in *Infrasound Monitoring for Atmospheric Studies*, edited by Le Pichon, A., Blanc, E., and Hauchecorne, A. (Springer, Dordrecht Heidelberg London New York) pp. 3 – 27

Faber, B. M. (2017) “Acoustical Measurements with Smartphones: Possibilities and Limitations” *Acoustics Today*. 13(2): 10-17

Fawcett, T. (2005) “An Introduction to ROC Analysis” *Science Direct Pattern Recognition Letters*, 27(2006):861-874

Fee, D., Garcés, M. and Steffke, A. (2010) “Infrasound from Tungurahua Volcano 2006-2008: Strombolian to Plinian eruptive activity” *Journal of Volcanology and Geothermal Research, 193,* 67-81

Gabor, D. (1946) “Theory of Communications. Part 1: The Analysis of Information”, *Journal of the Institution of Electrical Engineers*, 93(26)*,* 429-457

Garcés, M. A., Aucan, J., Fee, D., Caron, P. Merrifield, M., Gibson, R., Bhattacharyya, J., and Shah, S. (2006) “Infrasound from Large Surf” *Geophysical Research Letters, 33*(L05611)

Garcés, M. A. and Le Pichon, A. (2009) “Infrasound from Earthquakes, Tsunamis and Volcanoes”, in *Encyclopedia of Complexity and Systems Science*, Springer, pp. 4839-4855

Garcés, M. A., Park, J., and Thigpen, B., (2009) “The rotary subwoofer: A controllable infrasound source”. J. Acoust. Soc. Am. *125*(4):2006-2012

Garcés, M. A. (2013) “On infrasound standards, Part 1: Time, frequency and energy scaling”. InfraMatics 2(2): 13-35

Grus, J. (2015) *Data Science from Scratch: First principles with Pyhton,* 1st Ed., O'Reilly Media, Inc., Sebastopol, California

He, Y., Yu, F. R., Zhao, N., Yin, H., Yao, H., and Qiu, R. C. (2016) "Big Data Analytics in Mobile Cellular Networks", *IEEE Access*, Volume 4, 1985-1996

Hupe, P., Ceranna, L., and Pilger, C. (2018) "Using barometric time series of the IMS infrasound network for a global analysis of thermally induced atmospheric tides", *Atmos. Meas. Tech.*, 11, 2027-2040

IDC (2018) "Smartphone Vendor" (International Data Corporation) https://www.idc.com/promo/smartphone-market-share/vendor

Kardous, C. A. and Shaw, P. B. (2014) "Evaluation of smartphone sound measurement applications" J. Acoust. Soc. Am. 135(4):EL186-EL192

Kardous, C. A. and Shaw, P. B. (2016) "Evaluation of smartphone sound measurement application (*apps*) using external microphones – A follow-up study" J. Acoust. Soc. Am. 140(4):EL327-EL333

Kinsler, L. E., Frey, A. R., Coppens, A. B., and Sanders, J. V. (1982) *Fundamentals of Acoustics*, Third Edition ed., John Wiley & Sons, Inc., 480 pp.

Ko, W. H. (2007) "Trends and frontiers of MEMS" *Sens. Actuators A*, 136, 62-67

Kong, Q., Allen, R. M., Schreier, L., and Kwon, Y. W. **(2016)** "MyShake: A smartphone seismic network for earthquake early warning and beyond" Sci. Adv. **2**(2):e1501055 8pp.

Kromer, R. P., Hart, D. M. and Harris, J. M. (2007) "Test definitions for the evaluation of infrasound sensors". Sandia National Laboratories Technical Report SAND2007-5038

Larsonner, F., Uszakiewicz, H-G. and Mende, M. (2014) "Infrasound sensors and their calibration at low frequency". *INTERNOISE 2014 - 43rd International Congress on Noise Control Engineering: Improving the World Through Noise Control*, Melbourne, Australia 16 – 19 November

Liszka, L. and Waldemark, K. (1995) " High resolution observations of infrasound generated by the supersonic flights of Concorde" *Journal of Low Frequency Noise & Vibration, 14*(4), 181-192

Lo, F. (2018) *What is Data Science?* Retrieved from https://datajobs.com/what-is-data-science

Marcillo O., Johnson, J. B. and Hart, D. (2012) "Implementation, characterization, and evaluation of an inexpensive low-power low-noise infrasound sensor based on a micromachined differential pressure transducer and mechanical filter" *J. Atmos. Oceanic Technol.,* 29, 1275-1284

Marty, J. (2019) “The IMS Infrasound Network: Current Status and Technological Developments” in *Infrasound Monitoring for Atmospheric Studies: Challenges in Middle Atmosphere Dynamics and Societal Benefits, Second Edition*, edited by Le Pichon, A., Blanc, E., and Hauchecorne, A. (Springer, Switzerland) pp. 3 – 62

Merchant J. and Hart, D. (2011) “Component evaluation testing and analysis algorithms”, Sandia National Laboratories Technical Report SAND2011-8265.

Merchant J. and McDowell, K. (2014) “MB3a Infrasound sensor evaluation”, Sandia National Laboratories Technical Report SAND2014-20108

Mialle, P., Brown, D., Arora, N., and colleagues from IDC (2019) “Advances in Operational Processing at the International Data Centre” in *Infrasound Monitoring for Atmospheric Studies: Challenges in Middle Atmosphere Dynamics and Societal Benefits, Second Edition*, edited by Le Pichon, A., Blanc, E., and Hauchecorne, A. (Springer, Switzerland) pp. 209-248

Microsoft Azure (2018) Available at https://azure.microsoft.com/en-us/overview/what-is-cloud-computing/ (Last viewed December 6, 2018)

Mikumo, T. (1968) “Atmospheric pressure waves and tectonic deformation associated with the Alaskan earthquake of March 28, 1964” *Journal of Geophysical Research, 73,* 2009-2025

Minson, S. E., Brooks, B. A., Glennie, C. L., Murray, J. R., Langbein, J. O., Owen, S. E., Heaton, T. H., Iannucci, R. A., and Hauser, D. L. (2015) “Crowdsourced earthquake early warning” Sci. Adv. 1(3):e1500036 7pp.

Molnár, K., Sujbert, L., and Péceli, G. (2003) “Synchronization of sampling in distributed signal processing systems” in *2003 IEEE International Symposium on Intelligent Signal Processing*, Budapest, Hungary, 6 September

Nief, G., Talmadge, C., Rothman, J., and Gabrielson, T. (2019) “New Generations of Infrasound Sensors: Technological Developments and Calibration” in *Infrasound Monitoring for Atmospheric Studies: Challenges in Middle Atmosphere Dynamics and Societal Benefits, Second Edition*, edited by Le Pichon, A., Blanc, E., and Hauchecorne, A. (Springer, Switzerland) pp. 63-89

Nyquist, H. (1928) “Certain Topics in Telegraph Transmission Theory” *Transactions of the American Institute of Electrical Engineers, 47*(2) pp. 617-644

Ollivier S., Salze, E., Averiyanov, M., Yuldashev, P., Khokhlova, V., and Blanc-Benon, P. (2012) "Calibration method for high frequency microphones" in *Proceedings of the Acoustics Nantes Conference*, Nantes, France, April 2012.

Oppenheim, A. V. and Schafer, R. W. (1989) *Discrete-time Signal Processing*, Prentice Hall, Englewood Cliffs, New Jersey 07632, 879 pp.

Park, J., Garces, M. A. and Thigpen, B. (2009a) "The rotary subwoofer: A controllable infrasound source", *J. Acoust. Soc. Am.* 125(4), 2006-2012

Park J. and Robertson, J. (2009b) "A portable infrasound generator" J. Acoust. Soc. Am. *125*(4):EL148-EL151

Percival, D. B. and Walden, A. T. (1993) *Spectral Analysis for Physical Applications: Multitaper and Conventional Univariate Techniques*, Cambridge University Press, Cambridge, 583 pp.

Pierce, A. D. (1981) *Acoustics – An Introduction to its Physical Properties and Applications*, McGraw-Hill, New York, 678 pp.

Ponceau, D. and Bosca, L. (2010) "Low-Noise Broadband Microbarometers", in *Infrasound Monitoring for Atmospheric Studies*, edited by Le Pichon, A., Blanc, E., and Hauchecorne, A. (Springer, Dordrecht Heidelberg London New York) pp. 119-140

Randall, R. B. (2008) "Spectral Analysis and Correlation" in *Handbook of Signal Processing in Acoustics, Volume 1,* edited by Havelock, D., Kuwano, S., and Vorländer, (Springer, New York) pp. 33-52

Redvox (2018) Infrasound Recorder for Android and Apple iOS [Mobile application software]. Retrieved from Play Store and Apple Store

Refraction Technology Inc. (2011) "130-01 Operations: Startup", [Available online at http://nappe.wustl.edu/SPREE/instrument-other-documentation/from-RefTek/130_startup_01.pdf], 121 pp. (Last viewed November 19, 2018)

ReVelle, D. O. (1975) " Studies of sounds from meteors" *Sky and Telescope, 49,* 87-91

Scott, E. D., Hayward, C., Kubichek, R. F., Hamann, J. C., Pierre, J. W., Comey, B., and Mendenhall, T. (2007) "Single and Multiple Sensor Identification of Avalanche-generated Infrasound" *Cold Regions Science and Technology*, *47*(1)

Seismowave (2015) “MB3d Infrasound Sensor”, available online at http://seismowave.com/medias/documents/MB3d2.pdf (Last viewed November 19, 2018)

Shannon, C. E. (1949) “Communication in the Presence of Noise” *Proceedings of the IRE, 37*(1) pp. 10-21

Sleeman, R., van Wettum, A., and Trampert, J. (2006) “Three-channel Correlation Analysis: A New Technique to Measure Instrumental Noise of Digitizers and Seismic Sensors” *Bulletin of the Seismological Society of America*, **96**(1), 258-271

Smith, S. W. (1999) *The Scientist and Engineer’s Guide to Digital Signal Processing, Second Edition,* California Technical Publishing, San Diego, California, 650 pp.

Swanson, D. C. (2008) “Acoustic Data Acquisition”, in *Handbook of Signal Processing in Acoustics, Volume 1*, edited by Havelock, D., Kuwano, S. and Vorländer, M. (Springer, New York) pp. 17 – 32

Tian, C., Jiang, H., Liu, X., Wang, X., Liu, W., and Wang, Y. (2009) “Tri-Message: A Lightweight Time Synchronization Protocol for High Latency and Resource-Constrained Networks” in *2009 IEEE International Conference on Communications*, Dresden, Germany, 14-18 June

Uematsu, H., Koizumi, Y., Saito, S., Nakagawa, A., and Harada, N. (2017) “Anomaly detection technique in sound to detect faulty equipment” *NTT Technical Review: NTT Group’s Artificial Intelligence Technology*, 15(8), 7 pp.

Vanwynsberghe, C., Marchiano, R., Ollivier, F., Challande, P., Moingeon, H., and Marchal, J. (2015) “Design and implementation of a multi-octave-band audio camera for realtime diagnosis” Applied Acoustics 89, 281-287

Wang, Q. and Wan, C. R. (2005) “A Novel CFAR Tonal Detector Using Phase Compensation” *IEEE J. Ocean. Eng.* 30(4):900-911

Wagner, R. P. and Fick, S. E. (2017) “Pressure reciprocity calibration of a MEMS microphone” J. Acoust. Soc. Am. 142(3):EL251-EL257

Watson, S. M., Chichester, D. L., Garces, M. A., Maceira, M., Johnson, J. T., Christe, A. J., Cardenas, E. S., Holschuh, T. V., and Asmar, K. A. (2018) “Use of infrasound to monitor nuclear facilities” in *Institute of Nuclear Materials Management 59th Annual Meeting,* Baltimore, Maryland, USA 22-26 July

Waxler, R. and Gilbert, K. E. (2006) “ The radiation of atmospheric microbaroms by ocean waves” *Journal of the Acoustical Society of America, 119*(5), 2651-2664

Welch, P. D. (1967) “The use of the Fast Fourier Transform for the estimation of power spectra” IEEE Trans.Audio Electroacoust., AU-15(2), 70-73

Wilson, C. R. (1967) “Infrasonic pressure waves from the aurora: a shock wave model”, *Nature* 216(131-133)

Yazti, D. Z and Krishnaswamy, S. (2014) “Mobile Big Data Analytics: Research, Practice, and Opportunities” in *2014 IEEE 15th International Conference on Mobile Data Management*, Brisbane, QLD, Australia, 14-18 July